# Theoretical investigation of Resonant inelastic X-ray spectroscopy of low dimensional spin systems

By

***Subhajyoti Pal***

**Enrolment No: PHYS11201705006**

**National Institute of Science Education and Research, Bhubaneswar**

***A thesis submitted to the***

***Board of Studies in Physical Sciences***

***In partial fulfillment of requirements***

***for the Degree of***

**DOCTOR OF PHILOSOPHY**

***of***

**HOMI BHABHA NATIONAL INSTITUTE**

March, 2026

# Homi Bhaba National Institute

## Recommendations of the Viva Voce Committee

As members of the Viva Voce Committee, we certify that we have read the dissertation prepared by **Subhajyoti Pal** entitled " **Theoretical investigation of Resonant inelastic X-ray spectroscopy of low dimensional spin systems** " and recommend that it may be accepted as fulfilling the thesis requirement for the award of Degree of Doctor of Philosophy.

| | |
|---|---|
| Chairman - Prof. Dr. Ashok Mohapatra<br>SPS-NISER | 13/03/2026 |
| Guide / Convener - Prof. Dr. Anamitra Mukherjee<br>SPS-NISER | 13/03/26 |
| Member 1 - Prof. Dr. V Ravi Chandra<br>SPS-NISER | Vullmiri . R. Chandra<br>13-03-2026 |
| Member 2 - Prof. Dr. Kush Saha<br>SPS-NISER | K Saha<br>13/03/26 |
| Member 3 (External) - Prof. Dr. Arijit Saha<br>Institute of Physics, Bhubaneswar | Arijit Saha<br>13/03/2026 |
| Examiner (External) - Prof. Dr. Tanmoy Das<br>Indian Institute of Science, Bangalore | 13/03/26 |

Final approval and acceptance of this thesis is contingent upon the candidate's submission of the final copies of the thesis to HBNI.
I/We hereby certify that I/we have read this thesis prepared under my/our direction and recommend that it may be accepted as fulfilling the thesis requirement.

**Date :** 13/03/2026

**Place :** NISER, Bhubaneswar

13/03/26

**Signature**

**Guide**

# STATEMENT BY AUTHOR

This dissertation has been submitted in partial fulfillment of requirements for an advanced degree at Homi Bhabha National Institute (HBNI) and is deposited in the Library to be made available to borrowers under rules of the HBNI.

Brief quotations from this dissertation are allowable without special permission, provided that accurate acknowledgement of source is made. Requests for permission for extended quotation from or reproduction of this manuscript in whole or in part may be granted by the Competent Authority of HBNI when in his or her judgment the proposed use of the material is in the interests of scholarship. In all other instances, however, permission must be obtained from the author.

Name: Subhajyoti Pal
Subhajyoti Pal
Signature of the Student

# DECLARATION

I, hereby declare that the investigation presented in the thesis has been carried out by me. The work is original and has not been submitted earlier as a whole or in part for a degree / diploma at this or any other Institution/ University.

Name: Subhajyoti Pal
Subhajyoti Pal
Signature of the Student

## CERTIFICATION ON ACADEMIC INTEGRITY

### Undertaking by the Student

1. I **Subhajyoti Pal**, HBNI Enrolment No. **PHYS11201705006** hereby undertake that the Thesis, titled **"Theoretical investigation of Resonant inelastic X-ray spectroscopy of low dimensional spin systems"** is prepared by me and is the original work undertaken by me.
2. I also hereby undertake that this document has been duly checked through a plagiarism detection tool and the document is found to be plagiarism free as per the guidelines of the Institute/ UGC.
3. I am aware and undertake that if plagiarism is detected in my thesis at any stage in the future, suitable penalty will be imposed as per the guidelines of the Institute/ UGC.

Subhajyoti Pal 16/03/2026

Signature of the Student with date

**Endorsed by the Thesis Supervisor:**

I certify that the thesis written by the researcher is plagiarism free as mentioned above by the student

16/3/26

Signature of the Thesis Supervisor with Date

**Name:** Anamitra Mukherjee

**Designation:** Associate Professor

**Department/ Centre:** School of Physical Sciences

**Name of the CI/ OCC:** National Institute of Science Education and Research

## List of Publications arising from the thesis

### Journal

1. "Theoretical analysis of multimagnon excitations in resonant inelastic x-ray scattering spectra of two-dimensional antiferromagnets", Subhajyoti Pal, Umesh Kumar, Prabhakar, and Anamitra Mukherjee, Phys. Rev. B **108**, 214405 (2023)

2. "Emergent quasiparticles & field-tuned rixs spectra in a trimerized spin-1/2 chain", Subhajyoti Pal, Pradeep Thakur, Ashis Kumar Nandy, and Anamitra Mukherjee, **arXiv**:2505.23208 [cond-mat.str-el], **(2025)**

### Conferences

1. (2024) Presented Poster at **ICBEC**-2024 at S. N. Bose National Centre for Basic Sciences, Kolkata.

2. (2024) Oral presentation at **APS March meeting** in Minneapolis, Minnesota,USA.

3. (2024) Oral presentation at **EQCMP**-2024 in Institute of Physics (IOP) Bhubaneswar, India.

4. (2023) Presented Poster at Annual Conference on Quantum condensed Matter(**QMAT**-2023) at NISER,Bhubaneswar.

5. (2023) Presented Poster at 4th PRL CONFERENCE ON CONDENSED MATTER PHYSICS (**PRL CCMP** 2023) at PRL, Ahmedabad from.

6. (2022) Presented Poster at Young Investigators Meet on Quantum Condensed Matter Theory-2022(**YIMQCMT**-2022) at NISER, Bhubaneswar.

7. (2021) Presented Poster at Young Investigators Meet on Quantum Condensed Matter Theory-2021(**YIMQCMT**-2021) at NISER, Bhubaneswar.

### Others

1. Prabhakar, **Subhajyoti Pal**, Umesh Kumar, Manoranjan Kumar, and Anamitra Mukherjee, "Fractionalized excitations and resonant inelastic x-ray spectra in frustrated spin-1/2 trimer chains," Phys. Rev. B **111**, 205106 (2025)

2. Gour Jana, Abhishek Joshi, **Subhajyoti Pal**, and Anamitra Mukherjee, “Emergent half-metal at finite temperatures in a mott insulator,” *Communications Physics* **5**, 66 (2022).

Name: Subhajyoti Pal
Subhajyoti Pal
Signature of the Student

# DEDICATION

*To my family, whose unconditional love, sacrifice, and unwavering support made this journey not only possible, but meaningful.*

# ACKNOWLEDGEMENTS

This thesis is the end of one long journey, but I could not have walked it alone. There are so many people who stood beside me, in ways big and small, and I want to thank them from the bottom of my heart.

First, to my parents — thank you for your endless patience and for supporting me financially when things were hard. You have sacrificed so much for me, and whatever I achieve in life will always be because of you. To my supervisor, Prof. Anamitra Mukherjee — thank you for believing in me, even when I doubted myself. You gave me the freedom to chase my own ideas, and at the same time, you were there with guidance whenever I was stuck. Your trust has shaped me as a researcher and as a person. To Dr. Pradeep Thakur — your tough questions, sharp comments, and deep discussions have always pushed me to think differently and more deeply. You have a way of pushing boundaries and making people think nontrivially, and I am grateful for that. I also want to thank Aritra Mukhopadhyay for always helping me with GitHub (sometimes more times than I would like to admit!) and for his patience. My friend Rahul Ghosh — thank you for valuing my suggestions and respecting my ideas, that really gave me confidence. A very special mention goes to my friends from medical backgrounds — Dr.Payel Ghosh, Spandita Kundu, and Dr.Manikarnika. You not only helped me financially when times were rough, but you also had faith in me when I was losing mine. Payel, especially — thank you for being there during a medical emergency in my family. I will never forget that. I want to thank Dr. Biyas Koley for standing by me during my period of depression. Without your support and guidance, those days would have been much darker. I am also grateful to Adv. Ananya Bhattacharya from Kolkata High Court for her timely legal advice and support during a stressful period. To my gym buddies, Dinesh Kumar Panda and Sakti Ranjan Rout — thank you for the fitness suggestions, for dragging me to the gym, and for keeping my health in check when I wanted to ignore it. To Pappu Vaiya — thank you for helping me with paperwork, leave forms, and signatures. You took care of so many small things that made my life so much easier.

Now, I must take a moment to go back to my graduation days — the time when my journey in physics truly started. Dr. Monorama Chatterjee, Head of the Physics Department at Asutosh College — I still remember those weekend classes you took just for me when I was struggling to catch up. Even when my results were embarrassingly bad, you stood by me and kept encouraging me. Without your kindness and constant support, I would have probably given up right there.

Dr. Mainak Gupta — you were the teacher who made me fall in love with physics properly. The way you explained the basics, patiently and with so much clarity, built the foundation on which everything I do today rests. Whenever I solve a problem or understand a tough concept, I know it goes back to those days in your classroom. Dr. Bedanga Das Mohanti — I can never forget that you allowed me to attend the NISER viva even though I was a day late. That one act of kindness changed my life completely, because without it, I would not even be here writing this thesis. I owe you a debt of gratitude that words can't fully capture.

And finally, I'll be honest — I also want to acknowledge Copilot for helping me write codes and GitHub for helping me manage them. These tools saved me countless hours and made my research smoother.

To everyone I've mentioned, and even to those I may have forgotten, thank you. This thesis carries my name, but it belongs just as much to all of you.

# ABSTRACT

Strongly correlated electron systems, particularly low-dimensional quantum magnets, host a rich landscape of emergent phenomena driven by intense electron-electron interactions and reduced dimensionality. This thesis presents a unified theoretical investigation of multi-spin dynamics in spin-$1/2$ systems, leveraging Resonant Inelastic X-ray Scattering (RIXS) as a momentum-resolved probe of spin, charge, and orbital excitations. Employing the ultrashort core-hole lifetime (UCL) expansion of the Kramers-Heisenberg formalism, the work systematically decomposes RIXS cross-sections into spin-conserving and non-conserving channels, enabling the identification of both conventional and unconventional quasiparticles.

In two-dimensional cuprates, such as $\mathrm{La_2CuO_4}$, experimental RIXS spectra reveal broad, weakly dispersive high-energy features that elude explanation within standard one- and two-magnon frameworks. Through linear spin wave theory (LSWT) and exact diagonalization, this thesis demonstrates that three-magnon excitations—arising from higher-order spin-flip processes in the non-conserving channel—account for these features, highlighting the essential role of multi-spin dynamics in 2D antiferromagnets.

Turning to one-dimensional systems, the thesis investigates trimerized spin-$1/2$ chains realized in $\mathrm{Na_2Cu_3Ge_4O_{12}}$ ($J_1 > J_2$) and $\mathrm{Cu_3(P_2O_6OH)_2}$ ($J_1 < J_2$). Using density matrix renormalization group (DMRG), exact diagonalization, and real-space renormalization group techniques, the study uncovers a hierarchy of excitations: gapless spinons, composite doublons and quartons, and multi-trimer modes, all directly observable via RIXS. The application of a magnetic field reveals a robust one-third magnetization plateau and a field-driven evolution of the excitation spectrum, culminating in the emergence of gapless spin-1 bosonic modes indicative of a field-tuned Bose-Einstein condensate.

Collectively, these results establish RIXS as a powerful tool for probing fractionalization and composite quasiparticles in strongly correlated quantum materials. The thesis bridges experimental observations and theoretical modeling, deepening our understanding of quantum magnetism and superconductivity in cuprates, and laying the groundwork for future studies of emergent phenomena in low-dimensional systems.

# Contents

# Summary

The study of strongly correlated electron systems stands at the forefront of condensed matter physics, offering a window into the collective quantum phenomena that emerge when electrons interact intensely within solids. Materials such as cuprates, which host high-temperature superconductivity, magnetism, and Mott insulating states, exemplify the richness and complexity of these systems [40]. Despite decades of research, many fundamental questions remain unresolved—most notably, the microscopic mechanisms underlying unconventional superconductivity and the nature of exotic excitations in low-dimensional quantum magnets.

A central challenge in this field is to unravel the dynamics of quasiparticles—elementary collective excitations such as magnons, spinons, and composite modes—that govern the low-energy physics of correlated materials. Traditional experimental probes, including angle-resolved photoemission spectroscopy (ARPES) [42] and inelastic neutron scattering (INS) [1], have provided invaluable insights into charge and spin dynamics. However, these techniques face limitations in energy resolution, sample requirements, and sensitivity to multi-particle processes. In recent years, resonant inelastic X-ray scattering (RIXS) has emerged as a uniquely powerful tool, capable of accessing a broad spectrum of spin, charge, orbital, and lattice excitations with element and orbital specificity [9, 43]. RIXS enables momentum-resolved studies of both single- and multi-spin excitations, opening new avenues for exploring quantum magnetism and superconductivity.

This thesis is motivated by the need to advance our understanding of magnetic excitations in low-dimensional quantum systems, leveraging the capabilities of RIXS to probe phenomena inaccessible to conventional techniques. The work is situated at the intersection of experimental progress and theoretical innovation, addressing key questions: What are the origins of unconventional high-energy features observed in RIXS spectra of two-dimensional cuprates? How do composite and fractionalized quasiparticles emerge in one-dimensional trimerized spin chains, and how are their dynamics modulated by external fields?

To tackle these questions, the thesis develops and applies a suite of analytical and numerical methods—including linear spin wave theory (LSWT), exact diagonalization (ED), density matrix renormalization group (DMRG), and real-space renormalization group (RG)—within the framework of the ultra-short core-hole lifetime (UCL) expansion of the Kramers-Heisenberg formalism [82, 95]. This approach enables a systematic decomposition of RIXS cross-sections into spin-

conserving and non-conserving channels, revealing the hierarchy of multi-spin processes that shape the excitation spectrum.

Key findings of the thesis include the identification of three-magnon excitations as the origin of the broad, weakly dispersive high-energy feature observed in Cu $L$-edge RIXS measurements on $La_2CuO_4$ [139, 125]. By extending the Heisenberg model to include next-nearest-neighbor interactions and calculating higher-order UCL corrections, the work demonstrates that conventional one- and two-magnon frameworks are insufficient, and that three-spin processes play a crucial role in the magnetic dynamics of 2D cuprates.

In the realm of one-dimensional systems, the thesis explores trimerized spin-$1/2$ chains, such as $Cu_3(P_2O_6OH)_2$ [126], uncovering a rich spectrum of fractionalized spinons and composite quasiparticles — doublons, quartons, and multi-trimer modes—directly observable via RIXS. The application of a magnetic field reveals a robust one-third magnetization plateau and a field-driven evolution of the excitation spectrum, culminating in the emergence of gapless spin-1 bosonic modes suggestive of a stabilize Bose-Einstein condensate in Temperature-dependent dimensional crossove state of $Cu_3(P_2O_6OH)_2$.

By synthesizing experimental observations and theoretical modeling, this thesis establishes RIXS as a central probe for unraveling the complex hierarchy of excitations in strongly correlated materials. The results not only deepen our understanding of quantum magnetism and superconductivity in cuprates but also lay the groundwork for future studies of fractionalization, composite modes, and field-tuned quantum phase transitions in low-dimensional systems. In doing so, the thesis contributes to the broader scientific quest to decode the emergent phenomena that arise from strong electron correlations, bridging the gap between theory and experiment in the exploration of quantum materials.

# List of Figures

# List of Tables

# Chapter 1

# Introduction

When a large number of electrons and ions—on the order of $10^{23}$—assemble to form a solid, their individual identities are largely lost, and the system begins exhibiting complex collective behavior. In certain materials, this complex collective behavior is governed by strong interactions between electrons. Such materials, referred to as ***strongly correlated systems***, give rise to a wide range of emergent quantum phenomena, including magnetism, high-temperature superconductivity, and Mott insulating states [40].

Since the discovery of high-temperature superconductivity in two-dimensional cuprates [17], identification of fractionalized excitations in one-dimensional spin chains [20], and the observation of the two-dimensional Quantum Hall effect [91], low-dimensional spin systems have become a central area of interest in condensed matter physics. These systems, with their reduced dimensionality, exhibit rich and often unexpected quantum behavior that is rarely observed in three-dimensional materials [81, 5]. They provide an excellent platform to study fundamental questions related to magnetism, quantum fluctuations, and strong electron correlations.

A particularly active area of research is the search for quantum spin liquids—a novel state of matter characterized by power-law quantum correlations but the absence of long-range magnetic order even at zero temperature. Since Anderson's proposal of the *resonating valencebond* (RVB) state as a potential ground state of the antiferromagnetic insulating phase in high-$T_c$ cuprates [34], this concept has motivated intense theoretical and experimental investigation aimed at identifying real materials that exhibit such exotic ground states.

These motivations provide the foundation for the studies presented in this thesis. The focus of this work is to investigate the properties and dynamics of low-dimensional quantum spin systems, particularly one- and two-dimensional magnetic materials, through the lens of advanced spectroscopic techniques.

In the chapter that follows, we provide a detailed overview of one- and two-dimensional spin systems, review recent theoretical and experimental progress, and introduce the key material platforms explored in this work.

## 1.1 High $T_c$ superconductors:

High-$T_c$ cuprate superconductors are among the most extensively studied materials in condensed matter physics. In their undoped state, these transition metal oxides exhibit antiferromagnetic (AFM) order at low temperatures [40, 143, 82]. Beyond their superconducting behavior, two-dimensional cuprates also exhibit a variety of remarkable phenomena, such as charge and spin stripe order [160], pseudogap behavior [158], and antiferromagnetic Mott insulating phases [162]. These complex properties arise from strong electron-electron correlations, which dominate the physics of these systems and give rise to a rich array of emergent phenomena, including Mott insulating behavior, symmetry-breaking orders, high-temperature superconductivity, strange metals, and metal-insulator transitions [101, 40, 82, 86].

The first high-$T_c$ superconductivity was discovered in a cuprate compound, $\mathrm{Ba_xLa_{5-x}Cu_5O_{5(3-y)}}$, with a transition temperature of 30 K [17], significantly higher than what was predicted by BCS theory or observed in conventional superconductors. Since then, numerous high-$T_c$ compounds have been discovered. Notably, mercury-based cuprates have achieved superconducting transition temperatures up to 133 K [144]. Under high-pressure conditions, even higher values of $T_c$, reaching 165 K, have been reported in mercury-based copper oxides [182].

Since liquid nitrogen boils at 77 K, high-$T_c$ materials have raised the possibility of practical applications such as superconducting quantum interference devices (SQUIDs) and Josephson junction-based integrated circuits [116, 40]. Despite these advances, widespread technological implementation remains limited due to various material and engineering challenges.

In figure 1.1 we summarizes the major discoveries of high-$T_c$ superconductors over the past

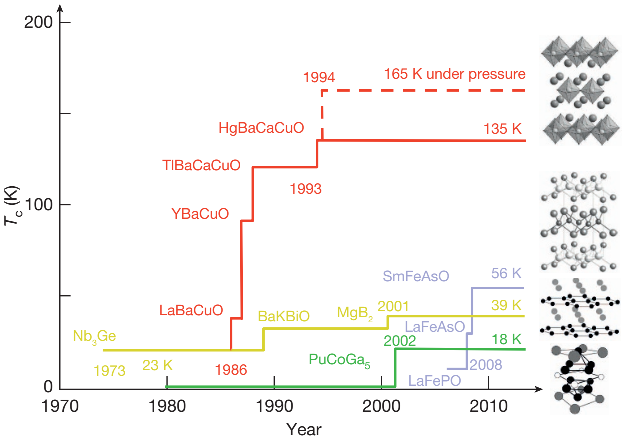

Figure 1.1: Superconducting transition temperatures ($T_c$) plotted against the year of discovery for various classes of superconducting materials [87]. Representative crystal structures for selected compounds are shown on the right. Conventional electron-phonon superconductors (yellow) exhibit a maximum $T_c$ of 39 K in $MgB_2$. Despite low Fermi energies, heavy-fermion superconductors (green) display notably high $T_c$ values due to strong electronic correlations. Iron-based superconductors (purple), discovered more recently, achieve $T_c$ values approaching 60 K. The highest known $T_c$ is found in the copper oxide (cuprate) family (red), reaching 165 K under pressure in a mercury-based cuprate compound (dashed red line).

four decades, including their critical temperatures and representative crystal structures.

Yet, even after more than thirty years, a definitive understanding of the complete framework of mechanism behind high-$T_c$ superconductivity, strange metal, violation of Luttinger's theorem remain elusive. One of the most fundamental open questions in the field is the nature of the superconducting pairing glue.

### 1.1.1 Crystal structure of 2D cuprates

Copper-based superconductors, commonly referred to as cuprates, are part of the 3d transition metal oxide family. These materials are distinguished by their layered perovskite-like structures, which consist of alternating copper-oxygen ($CuO_2$) planes separated by layers containing elements such as lanthanum (La), yttrium (Y), or bismuth (Bi). The $CuO_2$ planes are central to the superconducting properties of these compounds, as they host the conduction electrons responsible for superconductivity. It is widely believed that the superconducting mechanism is closely tied to processes occurring within the $CuO_2$ planes, while the intermediate layers primarily act as charge reservoirs, supplying carriers to the $CuO_2$ planes.

Superconductivity in these materials is typically achieved through doping, which is accomplished via chemical substitution or adjustments in oxygen stoichiometry within the spacing layers. This doping process introduces charge carriers into the $CuO_2$ planes, enabling superconductivity. Over the decades, a wide range of compounds featuring $CuO_2$ planes have been synthesized. This diversity arises from the ability to modify several structural parameters, including the number of $CuO_2$ planes per unit cell, the atoms separating adjacent planes, and the composition and structure of the charge reservoir layers. These modifications have led to the discovery of numerous cuprate superconductors with varying properties.

In the following sections, we delve deeper into the lattice structure and phase diagrams of specific high-$T_c$ cuprate compounds, exploring their unique characteristics and the mechanisms underlying their superconducting behavior.

Figure 1.2 illustrates representative crystal structures of several cuprate families. Among them, $La_{2-x}Sr_xCuO_4$ (LSCO) is the prototypical hole-doped cuprate with a single $CuO_2$ layer per unit cell and a perovskite structure similar to $K_2NiF_4$. Superconductivity in LSCO arises when Sr doping suppresses the antiferromagnetic order of the parent insulating phase [138, 12]. $YBa_2Cu_3O_{6+x}$ (YBCO) has a more complex structure containing double $CuO_2$ planes separated by yttrium (Y) layers and additional Cu-O chains that act as charge reservoirs and contribute to its anisotropic properties [156]. Doping through oxygen content variation tunes its carrier concentration and enables superconductivity up to $T_c \approx 93$ K [178]. In contrast, $Nd_{2-x}Ce_xCuO_4$ (NCCO) represents the electron-doped side of the cuprate phase diagram. The **T'** structure in $Nd_{2-x}Ce_xCuO_4$ (NCCO) is a body-centered tetragonal phase similar to the **T** structure of LSCO, but crucially lacks apical oxygens in the charge-reservoir layers [40, 13]. This structural distinction favors electron doping and enables superconductivity around 20–25 K upon Ce substitution for Nd [13, 40].

We illustrate in Fig. 1.2(d) the single-layer structure of $Bi_2Sr_2Cu_2O_{6+x}$ (Bi2201), in Fig. 1.2(e)

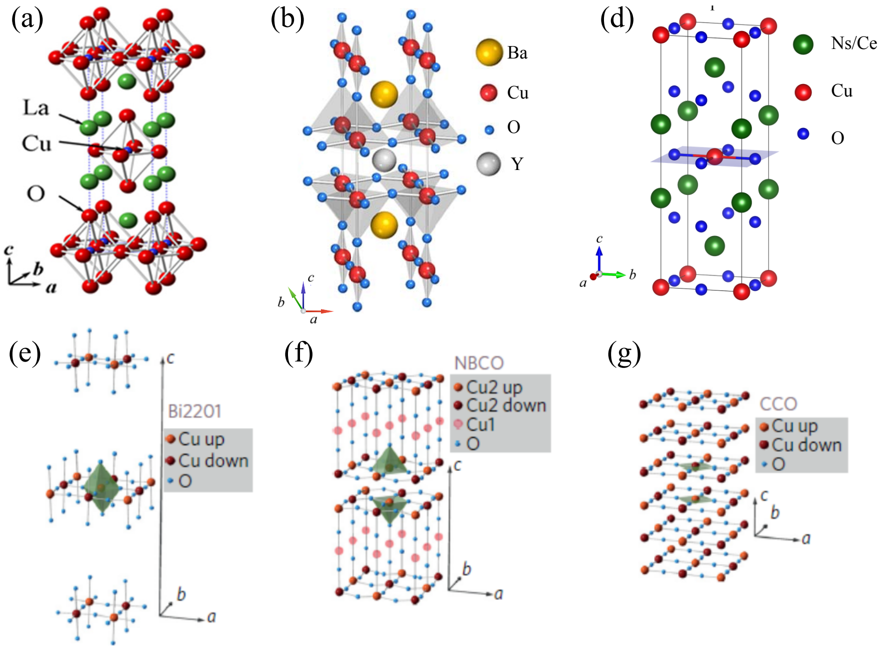

Figure 1.2: Representation of crystal structures for selected 2D cuprate families. Panel (a) shows $La_{2-x}Sr_xCuO_4$ (LSCO) [74], panel (b) illustrates $YBa_2Cu_3O_{6+x}$ (YBCO) [156], and panel (c) depicts $Nd_{2-x}Ce_xCuO_4$ (NCCO) [63]. Panels (d-f) present partial crystal structures of $Bi_2Sr_{2-x}La_xCuO_6$ (Bi2201), $NdBa_2Cu_3O_{6+x}$ (NBCO), and $CaCuO_2$ (CCO) respectively[128]

.

the bi-layer structure of $NdBa_2Cu_3O_{7-x}$ (NBCO), and in Fig. 1.2(f) the infinite-layer structure of $CaCu_2O_2$ (CCO). Despite their structural diversity, all cuprates share a common building block: the $CuO_2$ plane composed of corner-sharing $CuO_4$ plaquettes, where $Cu^{2+}$ ions in a square-planar coordination form the essential electronic states for superconductivity. Variations in the coordination environment—such as the presence or absence of apical oxygens—strongly influence the hybridization between Cu $3d$ and O $2p$ orbitals, and thus the superconducting and magnetic properties of these materials.

### 1.1.2 Phase diagram

The complexity of the physics of cuprates is encapsulated in the phase diagram shown in Figure 1.3. This diagram, distinguished by its unique features, illustrates the temperature dependence as a function of hole concentration in copper oxides. Notably, the superconducting phase is just one

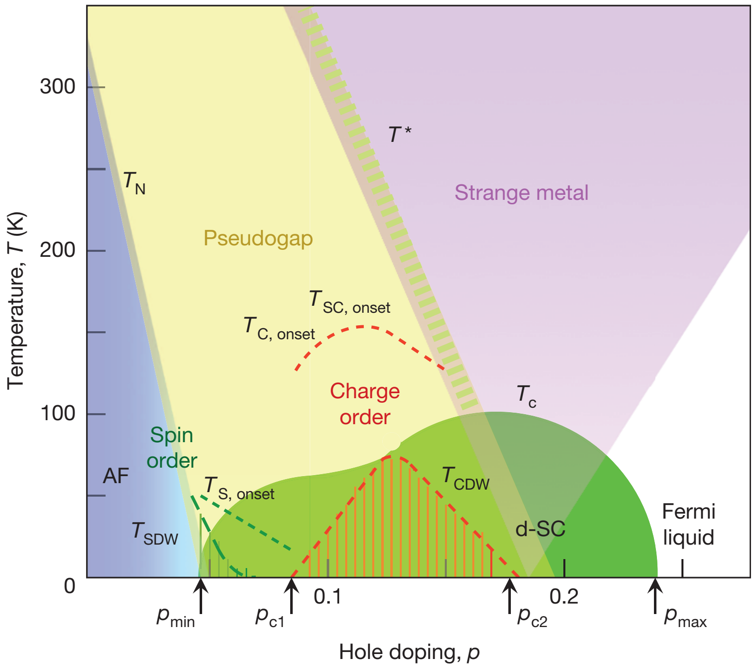

Figure 1.3: Schematic phase diagram [87] of high-$T_c$ cuprate superconductors as a function of hole doping ($p$) and temperature ($T$). The diagram highlights the antiferromagnetic (AFM) insulating phase at low doping, the superconducting (SC) dome, and the pseudogap (PG) region, along with other competing orders.

among several emergent phenomena present in these materials. Despite decades of research, a comprehensive explanation for this remarkably rich phase diagram remains elusive [40, 143, 101]. It should be emphasized that the phase diagram as a function of electron doping is qualitatively similar to that shown in Figure 1.3, with some notable exceptions—for instance, the absence of a pseudogap phase in electron-doped cuprates. As discussed above, the level of hole or electron doping can be tuned either by chemical substitution or by introducing additional oxygen atoms into the $CuO_2$ planes. This allows for the synthesis of compounds with varying doping levels and corresponding superconducting transition temperatures ($T_c$).

Specifically, hole-doped (electron-doped) cuprates are obtained when electrons are removed from (added to) the $CuO_2$ layers. At zero or extremely low doping, these materials are classified as insulators stabilized by interaction and charge-transfer energy scales, exhibiting long-range antiferromagnetic (AFM) order and an optical gap of approximately 2 eV. As the hole concentration increases, the AFM order is rapidly suppressed, and superconductivity emerges. The superconducting critical temperature $T_c$ rises with increasing doping, reaching a maximum at a doping level known as optimal doping (OP).

Between the antiferromagnetic (AFM) and optimally doped (OP) regions of the cuprate phase diagram lies the underdoped (UD) regime, which has garnered significant attention due to its unconventional properties. In this region, above the superconducting dome—where the density of state shows a minima at the Fermi energy—a distinct phase known as the pseudogap emerges and persists to temperatures well above $T_c$. Experimentally, the pseudogap manifests as a partial suppression of the electronic density of states near the Fermi level, often observed in spectroscopic measurements. One of its hallmarks is the appearance of so-called Fermi arcs along the nodal directions in the Brillouin zone [121].

Despite extensive experimental and theoretical efforts, the relationship between the pseudogap phase and superconductivity remains unresolved [159]. The microscopic origin of the pseudogap is still debated, but recent studies suggest that the underdoped regime hosts a variety of competing or intertwined orders on intermediate length scales. These include charge order or charge density waves (CDW), spin density waves (SDW), electronic nematicity, and possibly pair density waves (PDW). The interplay among these incipient orders and their connection to the pseudogap and superconductivity continues to be a central topic in the field of high-$T_c$ superconductivity.

Charge order is a ubiquitous feature of high-temperature superconducting (HTS) cuprates. Its first clear manifestation was observed as stripe order in the so-called “214” cuprate families (e.g., $\mathrm{La_{2-x-y}(Sr, Ba)_x(Nd, Eu)_yCuO_4}$) [160, 181, 3], where it is intimately linked to the uniaxially modulated antiferromagnetic (AFM) order of the $\mathrm{CuO_2}$ planes. In these materials, the charge order exhibits a commensurate modulation with a period of $4a$ (where $a$ is the Cu-Cu lattice spacing), while the associated spin modulation has twice this period. The interplay between these orders leads to a pronounced suppression of the superconducting transition temperature $T_c$ at a hole concentration near $p \approx 1/8$, providing compelling evidence for competition between stripe order and superconductivity.

In other cuprate families, such as the “123” compounds, signatures of charge density order in the underdoped regime were initially detected only under applied magnetic fields [179, 180]. More recently, long-range incommensurate charge density waves (CDWs) were discovered in (Y,Nd)$\mathrm{Ba_2Cu_3O_{6+\delta}}$ [58], with the incommensurate nature of the CDW wave vector revealed by X-ray scattering experiments. This breakthrough established X-ray techniques, particularly resonant X-ray scattering (RXS), as powerful tools for probing charge order in cuprates. Subsequent RXS studies have demonstrated that CDW order is a generic property of both hole[130, 36]- and electron-doped [38] cuprates. As with stripe order, the presence of CDW correlations further supports the notion of competition between charge ordering and superconductivity. Notably, the CDW signal typically reaches its maximum intensity near $T_c$ and diminishes sharply below the superconducting transition.

The phase diagram in Figure 1.3 encapsulates these phenomena. Competing orders, such as stripes and CDWs, are most prominent in the underdoped regime, with their onset temperatures lying within the pseudogap phase. Their evolution appears to influence the extent and shape of the superconducting dome. At higher doping levels and elevated temperatures, cuprates in the optimally doped (OP) and overdoped (OD) regions exhibit “strange metal” behavior—a non-Fermi liquid state with anomalous transport properties. In this regime, the electrical conductivity above $T_c$ is much lower than that of conventional metals, and its temperature and frequency dependence defy standard metallic theory.

Despite decades of intensive experimental and theoretical research, a comprehensive and universally accepted explanation for the mechanism of superconductivity in cuprates remains elusive. The unresolved nature of this problem continues to represent one of the most significant challenges in condensed matter physics.

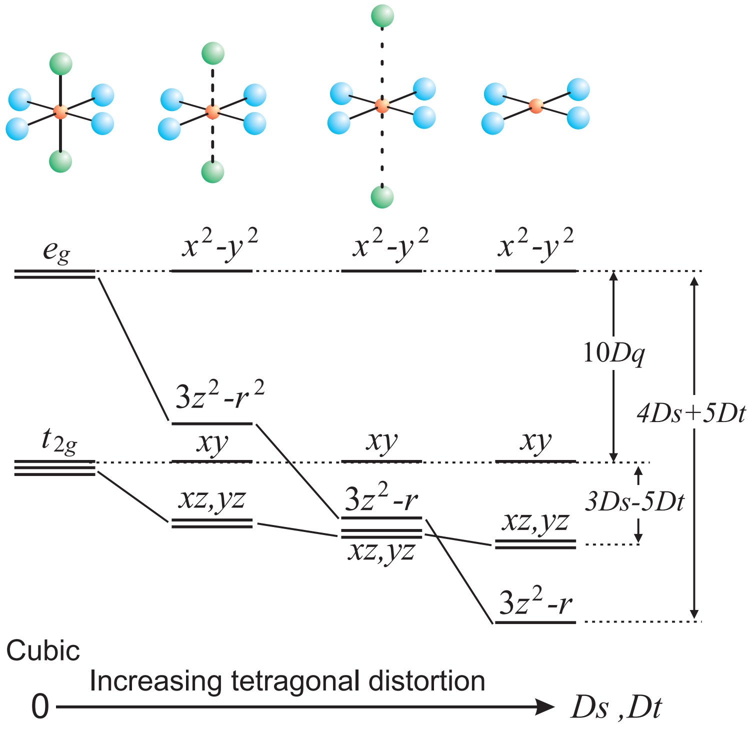

Figure 1.4: Local crystal field and energy level diagram for $d$ orbitals under spherical symmetry, cubic symmetry ($O_h$), and tetragonal symmetry ($D_{4h}$). Adapted from Ref. [117].

### 1.1.3 Electronic and magnetic properties of 2D cuprates

The electronic structure of high-$T_c$ cuprates can be understood within a simplified ionic framework. In this picture, copper ions ($Cu^{2+}$) in the $CuO_2$ planes adopt a $3d^9$ electronic configuration, with one unpaired electron occupying the $d_{x^2-y^2}$ orbital. Oxygen ions ($O^{2-}$), on the other hand, are in a $2p^6$ configuration, completing their $p$-shell. The interaction between the copper $d$ orbitals and oxygen $p$ orbitals results in the formation of bonding and antibonding states, which play a key role in determining the electronic properties of these materials. Consequently, the electronic behavior of high-$T_c$ cuprates is often described using a single-hole model with $d_{x^2-y^2}$ symmetry [143, 40, 117].

The energy levels of the copper $3d$ orbitals are influenced by the surrounding crystal environment, which is typically either tetragonal or orthorhombic. The coordination of oxygen ligands breaks the spherical symmetry of the copper ion's potential, leading to a splitting of the $3d$ orbitals as shown in the Fig: 1.4. This phenomenon is explained by the crystal field model, where the energy difference between the doubly degenerate $e_g$ orbitals ($d_{x^2-y^2}$ and $d_{3z^2-r^2}$) and the triply degenerate $t_{2g}$ orbitals ($d_{xy}$, $d_{xz}$, and $d_{yz}$) is quantified by the crystal field splitting parameter, $10Dq$. Additional terms, $4D_s + 5D_t$ and $3D_s - 5D_t$, further describe the energy separation between these states.

As the symmetry transitions from cubic ($O_h$) to tetragonal ($D_{4h}$) as a function of the distortion of the $CuO_6$ octahedra around the Cu ion, the degeneracy of the $e_g$ and $t_{2g}$ orbitals is lifted, resulting in a more complex energy level structure. This splitting is strongly influenced by the distance between the apical oxygen atoms and the copper ion. The relative positioning of these apical oxygens plays a critical role [127] in shaping the electronic properties of the $CuO_2$ planes, which are central to the superconducting behavior of high-$T_c$ cuprates.

***Three-band model:*** Building on the preceding discussion of crystal structure and crystal field (CF) splitting of orbitals, we now turn to the theoretical modeling of the electronic structure in high-$T_c$ cuprates. The complexity of these materials, with their layered architectures and multiple atomic species, necessitates certain simplifications to capture the essential physics. A natural starting point is to focus on the $CuO_2$ planes, as these are widely recognized as the primary stage for the unconventional superconductivity and magnetism observed in these compounds.

Within the $CuO_2$ planes, copper ions ($Cu^{2+}$) possess a $3d^9$ configuration, leaving a single hole predominantly in the $d_{x^2-y^2}$ orbital. The surrounding oxygen ions ($O^{2-}$) are fully occupied in their $2p$ orbitals. The strong hybridization between the copper $3d_{x^2-y^2}$ and oxygen $2p$ orbitals leads to the formation of bonding and antibonding bands, with the low-energy physics dominated by the antibonding states. This scenario justifies the use of an effective three-band model, where the relevant degrees of freedom are holes with $d_{x^2-y^2}$ symmetry [40, 143] moving on a two-dimensional lattice.

The local environment of the copper ions further refines this picture. The crystal field created by the surrounding oxygens lifts the degeneracy of the $3d$ orbitals, as illustrated in Fig. 1.4. In the typical tetragonal or orthorhombic symmetry of the cuprates, the $d_{x^2-y^2}$ orbital is pushed to the highest energy among the $3d$ states, making it the primary host for the unpaired electron (or hole). The magnitude of this splitting, and thus the detailed electronic structure, is sensitive to the geometry of the $\mathrm{CuO_6}$ octahedra, particularly the distance to the apical oxygens [127].

Given these considerations, the essential low-energy physics of undoped cuprates can be described by a lattice of localized spin-$1/2$ moments on the copper sites, interacting via superexchange mediated by the oxygen atoms. Upon doping, additional holes are introduced into the $\mathrm{CuO_2}$ planes, leading to a rich interplay between magnetism, charge dynamics, and superconductivity. While interlayer couplings and further orbital complexities can play important roles in specific phenomena, the three-band model on the $\mathrm{CuO_2}$ planes provides a robust foundation for understanding the emergent properties of high-$T_c$ superconductors. When a cuprate such as $\mathrm{La_{2-x}Sr_xCuO_4}$ is doped, for example by substituting a La atom with a Sr atom, an extra hole is introduced into the $\mathrm{CuO_2}$ plane. At first glance, one might expect that this simply removes another electron from the copper $d_{x^2-y^2}$ orbital. However, this picture does not account for the strong Coulomb repulsion that makes double occupancy of the same orbital energetically unfavorable. In reality, if interactions were neglected, $\mathrm{La_2CuO_4}$ would be metallic due to a half-filled conduction band. Instead, it is an antiferromagnetic insulator, highlighting the importance of electron correlations.

To capture the essential physics of these materials, it is useful to construct a model Hamiltonian that includes both the copper $3d_{x^2-y^2}$ and oxygen $2p$ orbitals, as well as the relevant hopping and interaction terms [49, 51, 165, 50, 40]. In the so-called “hole picture,” where the vacuum corresponds to all orbitals being filled, the Hamiltonian can be written as [40, 16]:

$$\begin{aligned} H = & -t_{pd}\sum_{\langle ij\rangle}\left(p_j^\dagger d_i + \text{h.c.}\right) - t_{pp}\sum_{\langle jj'\rangle}\left(p_j^\dagger p_{j'} + \text{h.c.}\right) + \epsilon_d\sum_i n_i^d + \epsilon_p\sum_j n_j^p \\ & + U_d\sum_i n_{i\uparrow}^d n_{i\downarrow}^d + U_p\sum_j n_{j\uparrow}^p n_{j\downarrow}^p + U_{dp}\sum_{\langle ij\rangle} n_i^d n_j^p \end{aligned} \tag{1.1}$$

Here, $d_i$ and $p_j$ are fermionic operators that annihilate holes at copper and oxygen sites, respectively. The sums $\langle ij\rangle$ and $\langle jj'\rangle$ run over nearest-neighbor Cu-O and O-O pairs. The hopping parameters $t_{pd}$ and $t_{pp}$ describe the hybridization between copper and oxygen, and between neighboring oxygen sites. The on-site energies $\epsilon_d$ and $\epsilon_p$ set the relative energy levels of the copper and oxygen orbitals. The terms $U_d$, $U_p$, and $U_{dp}$ represent the Coulomb repulsion for double occupancy on copper, on oxygen, and between adjacent copper and oxygen sites, respectively.

This model, often referred to as the three-band Hubbard model or Emery model, captures the essential interplay between kinetic energy and strong correlations in the $CuO_2$ planes. In the strong coupling limit and at half-filling, it reduces to an effective spin-$1/2$ Heisenberg model with antiferromagnetic superexchange interactions [188]. Upon doping, the motion of holes in this correlated background leads to a rich variety of phenomena, including high-temperature superconductivity.

***One-band model:*** While the three-band model provides a detailed description of the electronic structure in cuprates, it is still quite complex and involves many parameters. To make theoretical studies more tractable, researchers have sought to simplify the model further. A key step in this direction was proposed by Zhang and Rice, who showed that the essential low-energy physics can be captured by focusing on a single effective band [187].

Their argument is based on the observation that a hole introduced into the $CuO_2$ plane tends to form a *spin singlet state between the doped hole residing primarily on the oxygen* $2p$ *orbitals and the localized spin on the copper* $3d_{x^2-y^2}$ *orbital*, known as a Zhang–Rice singlet. In the case of cuprates, which are negative charge-transfer insulators, the doped holes predominantly occupy the oxygen sites rather than the copper sites, and their hybridization with the $Cu^{2+}$ $(3d^9)$ spin results in the formation of this bound singlet state. By projecting onto this singlet subspace, the problem can be mapped onto a model where the relevant degrees of freedom are spins and holes on a two-dimensional square lattice [50] of copper sites, with the oxygen degrees of freedom integrated out.

The resulting effective Hamiltonian is the so-called $t$-$J$ model [11]:

$$H = J \sum_{\langle ij \rangle} \left( \mathbf{S}_i \cdot \mathbf{S}_j - \frac{1}{4} n_i n_j \right) - t \sum_{\langle ij \rangle, \sigma} \left[ c^\dagger_{i\sigma} (1 - n_{i,-\sigma})(1 - n_{j,-\sigma}) c_{j\sigma} + \text{h.c.} \right] , \tag{1.2}$$

where $\mathbf{S}_i$ is the spin-$1/2$ operator at site $i$, $n_i$ is the number operator, $t$ is the hopping amplitude, and $J$ is the antiferromagnetic exchange interaction between nearest neighbors. The projection operators $(1 - n_{i,-\sigma})$ ensure that double occupancy is forbidden, reflecting the strong on-site Coulomb repulsion.

In this model, each site can be either empty (a hole) or occupied by a single electron with spin up or down. The $t$-$J$ model thus captures the interplay between electron motion and magnetic interactions in a strongly correlated system.

It is important to note that the reduction from the three-band model to the $t$-$J$ model is an approximation, and there is ongoing debate about its validity for all regimes [188]. Some studies suggest that certain aspects of the original three-band physics may be lost in this mapping, especially regarding the nature of the quasiparticles and the role of oxygen orbitals. Nevertheless, the $t$-$J$ model has become a standard tool for exploring the low-energy properties of cuprates.

Alongside the $t$-$J$ model, another widely studied simplification is the one-band Hubbard model [77]:

$$H = -t \sum_{\langle ij \rangle, \sigma} \left( c_{i\sigma}^{\dagger} c_{j\sigma} + \text{h.c.} \right) + U \sum_{i} \left( n_{i\uparrow} - \frac{1}{2} \right) \left( n_{i\downarrow} - \frac{1}{2} \right), \tag{1.3}$$

where $U$ is the on-site Coulomb repulsion. In the strong coupling limit ($U \gg t$), the Hubbard model reduces to the $t$-$J$ model, with $J = 4t^2/U$ [185].

Although the one-band Hubbard model is a further simplification and does not explicitly include the oxygen orbitals, it has been shown to reproduce many of the qualitative features of the cuprates, especially at low energies. Numerical studies indicate that, with appropriate parameters, the Hubbard and $t$-$J$ models can capture the essential magnetic and electronic properties observed in experiments.

Despite their simplicity, these models remain central to our theoretical understanding of high-$T_c$ superconductors. They provide a framework for exploring how strong correlations, magnetism, and doping interplay to give rise to the rich phase diagrams and exotic phenomena seen in cuprate materials.

## 1.2 Crystal structure of 1D cuprates

One-dimensional (1D) cuprates are a distinctive class of transition metal oxides where copper and oxygen atoms form chain-like arrangements, resulting in strongly anisotropic physical properties. In contrast to the more commonly studied two-dimensional (2D) cuprates—where $CuO_2$ planes dominate the electronic behavior—the copper-oxygen units in 1D cuprates are arranged into linear or quasi-one-dimensional chains. This reduced dimensionality enhances quantum fluctuations and suppresses long-range magnetic order, making these systems ideal platforms for exploring fundamental aspects of strongly correlated electron physics in low dimensions.

Structurally, the essential building blocks of 1D cuprates are square-planar $CuO_4$ plaquettes, which are corner-shared or edge-shared to form extended chains along specific crystallographic directions. Notable examples include $Sr_2CuO_3$ and $Ba_{2-x}Sr_xCuO_{3+\delta}$, as well as the so-called infinite-chain compounds $ACuO_2$, where $A$ represents an alkali or alkaline earth metal (e.g., Li, Na, K, Rb, Cs). For instance, in $Sr_2CuO_3$, the copper ions are arranged in nearly perfect linear chains along the $b$-axis, connected through corner-sharing $CuO_4$ units, as shown in Figure 1.5. This highly anisotropic structure results in electronic transport and magnetic properties that are predominantly one-dimensional [141].

The physical properties of these materials are profoundly influenced by their dimensionality. In 1D, quantum fluctuations are significantly enhanced, and conventional long-range magnetic order is suppressed at finite temperatures, in accordance with the Mermin-Wagner theorem [113]. As a consequence, 1D spin systems often exhibit exotic phenomena absent in higher dimensions. A key example is the fractionalization of elementary excitations: in the spin-1/2 antiferromagnetic Heisenberg chain, a single spin-flip excitation can decay into a pair of spinons—quasiparticles carrying fractional spin-1/2 quantum numbers [53]. This phenomenon of fractionalization is a hallmark of 1D quantum magnetism.

These systems also serve as important testbeds for theoretical techniques uniquely suited to one dimension. Models such as the spin-1/2 Heisenberg chain are exactly solvable via the Bethe ansatz [20], offering precise insights into their ground state and excitation spectra. Furthermore, field-theoretical approaches like bosonization and conformal field theory provide powerful tools for analyzing the low-energy behavior of 1D correlated systems [60]. These approaches reveal how reduced dimensionality facilitates the emergence of collective excitations, strong entanglement, and unconventional quantum phases such as spin liquids.

Hole doping introduces additional complexity and richness to the physics of 1D cuprates. By substituting elements or tuning oxygen content, one can introduce mobile carriers into the chains. This doping can drive the system through a series of quantum phase transitions, giving rise to competing ground states such as antiferromagnetic, spin-Peierls, or even superconducting phases under specific conditions. The interplay between strong correlations, dimensional confinement, and doping leads to a highly nontrivial phase diagram that is still under active investigation.

On the experimental front, several advanced spectroscopic techniques have been pivotal in probing the unique properties of 1D cuprates. Among them, resonant inelastic X-ray scattering (RIXS) [9, 43] has proven particularly powerful in detecting spin and orbital excitations with momentum and energy resolution. In addition, neutron scattering [171, 71, 35, 9, 43] and angle-resolved photoemission spectroscopy (ARPES) [36, 2, 37] have provided valuable information on magnetic dynamics and electronic structure. These methods have revealed not only the presence of fractionalized excitations but also their evolution under external perturbations such as doping, temperature, and applied fields.

Altogether, one-dimensional cuprates offer a fertile ground for investigating the fundamental physics of quantum magnetism, electron fractionalization, and strongly correlated electrons in low dimensions. By combining theoretical techniques suited to 1D systems with state-of-the-art experimental probes, these materials continue to deepen our understanding of the rich and often counterintuitive phenomena that emerge when interactions, topology, and quantum mechanics intertwine in reduced dimensions.

### 1.2.1 Electronic and magnetic properties of 1D cuprates

To study 1D cuprates it is essential to understand there lattice configuration and electronic configuration. *The three materials discussed in this section are relevant to the materials studied in this thesis.*

We start with the Goodenough-Kanamori-Anderson (GKA) theory that provides a microscopic understanding of magnetic superexchange interactions between transition metal ions mediated by nonmagnetic anions, such as oxygen. This framework is essential for explaining the magnetic properties of strongly correlated materials, particularly transition metal oxides like cuprates, manganites, and nickelates.

In insulating materials where direct overlap between magnetic ions is negligible, the dominant magnetic interaction arises from *superexchange*—a virtual hopping process through the ligand anion. This mechanism was first introduced by Anderson [10], and later refined through semi-empirical rules by Goodenough [61] and Kanamori [85]. The GKA theory systematically explains the sign and strength of exchange interactions based on orbital occupancy, bond angles, and symmetry considerations.

Consider two magnetic cations (e.g., $\mathrm{Cu}^{2+}$) connected via a nonmagnetic anion (e.g., $\mathrm{O}^{2-}$). The superexchange interaction arises from a second-order virtual hopping process, where an electron from one metal site virtually hops to the ligand and then to the neighboring metal site. The effective exchange Hamiltonian can be expressed as:

$$H_{\text{ex}} = J_{\text{eff}}\, \boldsymbol{S}_i \cdot \boldsymbol{S}_j, \tag{1.4}$$

where $J_{\text{eff}}$ is the exchange coupling constant, and $\boldsymbol{S}_i$, $\boldsymbol{S}_j$ are the spin operators on neighboring sites. The sign of $J_{\text{eff}}$ determines whether the interaction is ferromagnetic ($J < 0$) or antiferromagnetic ($J > 0$).

The GKA rules predict the sign of $J_{\text{eff}}$ based on the following factors:

**Bond Angle:**

- For **180**° metal-oxygen-metal bonds:
  - When the bond angle is close to 180° (linear arrangement), the overlap between the metal d-orbitals and oxygen p-orbitals is typically maximized. If the d-orbitals involved are half-filled, the interaction is usually strongly antiferromagnetic due to the Pauli exclusion principle, which favors opposite spins on the metal for kinetic energy lowering through virtual electron transfer.
  - If one orbital is *half-filled* and the other is *empty*, the interaction may become **ferromagnetic**.
- For **90**° bonds:
  - When the bond angle is around 90° (perpendicular arrangement), direct overlap between certain cation d-orbitals might be minimal, but indirect overlap through different anion p-orbitals can occur. This geometry often favors ferromagnetic coupling, especially if one of the cation orbitals is half-filled and the other is empty or fully occupied, allowing for spin-parallel virtual electron transfer consistent with Hund's rule. When the bond angle is around 90° (perpendicular arrangement), direct overlap between certain cation d-orbitals might be minimal, but indirect overlap through different anion p-orbitals can occur. This geometry often favors ferromagnetic coupling, especially if one of the cation orbitals is half-filled and the other is empty or fully occupied, allowing for spin-parallel virtual electron transfer consistent with Hund's rule

**Orbital Occupancy:**

- *Half-filled-half-filled:* Strong antiferromagnetic exchange.
- *Half-filled-empty or full-half-filled:* May result in ferromagnetic exchange.

**Orbital Symmetry and Overlap:**

- Stronger overlap between metal $d$ orbitals and oxygen $p$ orbitals leads to stronger exchange interactions.
- Directionality of orbitals (e.g., $d_{x^2-y^2}$ vs. $d_{3z^2-r^2}$) plays a crucial role.

So understanding the lattice configuration, orbital occupation and the bond angle is essential to understand the magnetic properties of 1D cuprates.

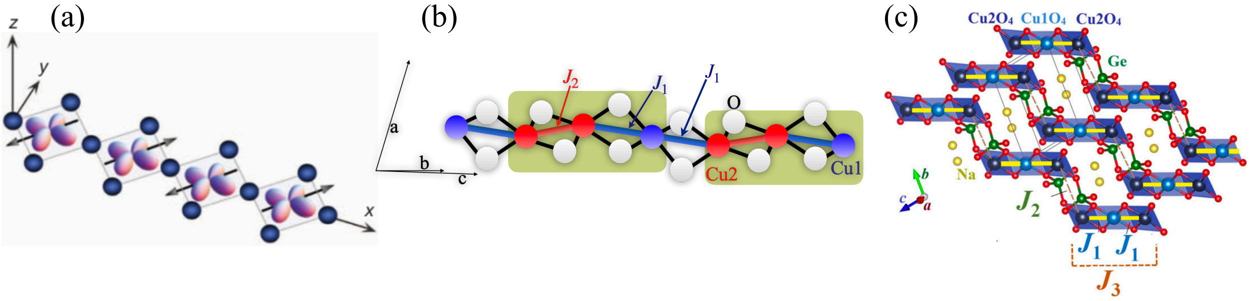

Figure 1.5: Schematic illustrations of the crystal structures of various one-dimensional (1D) cuprates. Panel (a) shows the crystal structure of $Sr_2CuO_3$ [147], where linear chains of corner-sharing $CuO_4$ plaquettes extend along the $x$-axis. Panel (b) presents a schematic representation of the positions of Cu and O atoms in $Cu_3(P_2O_6OH)_2$ [126]. Blue, red, and white circles represent Cu1 sites, Cu2 sites, and oxygen atoms connected to copper, respectively. Black bars indicate Cu-O bonds, while red and blue bars denote the shortest and second-shortest Cu-Cu distances, corresponding to exchange interactions $J_1$ and $J_2$. Panel (c) shows the schematic spin-trimer structure of $Na_2Cu_3Ge_4O_{12}$ [18]. Spins $S_1$, $S_2$, and $S_3$ denote the three $Cu^{2+}$ spins within a trimer unit. The exchange couplings $J_1$, $J_2$, and $J_3$ represent intratrimer, intertrimer, and next-nearest-neighbor intratrimer interactions, respectively. A schematic of a 1D spin chain with $J_1$, $J_2 = \alpha J_1$, and $J_3 = \beta J_1$ is also included for comparison.

**$Sr_2CuO_3$:** This compound is one of the most studied 1D cuparte. $Sr_2CuO_3$ is composed of chains of $CuO_4$ plaquettes, where each pair of adjacent plaquettes shares a corner oxygen atom (see Fig. S1). At the center of each plaquette sits a copper ion in a $3d^9$ electronic configuration, corresponding to a single hole in the $3d$ shell that carries spin $S = 1/2$. The strong on-site Coulomb repulsion $U$ among the copper $3d$ electrons drives the system into a Mott-insulating state. The optical gap, approximately $1.5\,\mathrm{eV}$[147], is of charge-transfer character, arising from the transfer of electrons from oxygen $2p$ orbitals to copper $3d$ orbitals. The pronounced crystal-field anisotropy inherent to the quasi-one-dimensional structure stabilizes a ferro-orbital ground state, with the holes occupying the $3d_{x^2-y^2}$ orbitals on each copper site. Magnetic interactions between neighboring spins are governed by a strong antiferromagnetic super-exchange coupling, with $J \approx 250\,\mathrm{meV}$—one of the largest values observed in cuprate systems. As a result, $Sr_2CuO_3$ closely realizes the physics of an ideal one-dimensional spin-$1/2$ antiferromagnetic Heisenberg chain, making it a model system for exploring quantum magnetism and fractionalized excitations in low dimensions.

**$Cu_3(P_2O_6OH)_2$:** Another notable example of a one-dimensional cuprate is $Cu_3(P_2O_6OH)_2$, which exhibits a distinctive chain structure where copper ions are linked via oxygen and phosphorus atoms. In this material, the copper ions are arranged in a zigzag configuration, resulting in a complex network of magnetic interactions. The magnetic behavior of $Cu_3(P_2O_6OH)_2$ has been the subject of extensive investigation, revealing a rich phase diagram that includes antiferromagnetic order and a characteristic 1/3 magnetization plateau [68]. The essential physics of this compound can be captured by an effective spin-$1/2$ model, which provides a framework for exploring quantum phase transitions and the emergence of unconventional magnetic states.

Structurally, $Cu_3(P_2O_6OH)_2$ crystallizes in the triclinic space group P1 (No. 2), with lattice parameters $a = 4.7819(16)$ Å, $b = 7.0370(8)$ Å, $c = 8.3574(8)$ Å, and angles $\alpha = 66.6790(6)°$, $\beta = 76.9930(7)°$, $\gamma = 72.0642(6)°$ [68]. The unit cell contains a single formula unit ($Z = 1$), and each $Cu^{2+}$ ion carries a spin-$1/2$. As illustrated in Supplemental Material Fig. 1.5, there are two inequivalent copper sites (Cu1 and Cu2) and two principal Cu–Cu exchange pathways. The shortest Cu–Cu separation is 3.06 Å, mediated by two equivalent Cu–O–Cu super-exchange paths with bond angles of $100.8°$. The next shortest Cu–Cu distance is 3.28 Å, with corresponding Cu–O–Cu angles of $98.0°$ and $98.5°$ [68]. According to the GKA rules, superexchange through Cu–O–Cu angles near $90°$ typically favors *ferromagnetic* coupling due to the orthogonality of the participating $d_{x^2-y^2}$ orbitals, whereas angles approaching $180°$ promote *antiferromagnetic* exchange via stronger overlap between the O $p$ and Cu $d$ orbitals. The observed Cu–O–Cu angles between $98°$ and $101°$ thus place the exchange interactions $J_1$ (shortest bond) and $J_2$ (second-shortest bond) in the regime of competing, moderately antiferromagnetic superexchange, consistent with the GKA framework.

All other Cu–Cu separations exceed 4.27 Å and contribute negligibly to the magnetic network.

Consequently, $Cu_3(P_2O_6OH)_2$ can be effectively described as a spin-$1/2$ trimer chain system with alternating $J_1$–$J_2$–$J_1$ exchange couplings. Quantum Monte Carlo analysis of magnetization data yields $J_1 = 30$ K and $J_2 = 111$ K, corresponding to a ratio $J_1/J_2 = 0.27$ [68]. The microscopic Hamiltonian governing this system is

$$H = \sum_i \left( J_1 \, \mathbf{S}_i^a \cdot \mathbf{S}_i^b + J_2 \, \mathbf{S}_i^b \cdot \mathbf{S}_i^c + J_1 \, \mathbf{S}_i^c \cdot \mathbf{S}_{i+1}^a \right) , \tag{1.5}$$

where $i$ indexes unit cells, and $\{a, b, c\}$ label trimer spins.

**$Na_2Cu_3Ge_4O_{12}$:** $Na_2Cu_3Ge_4O_{12}$ is an excellent realization of a spin-1/2 Heisenberg antiferromagnetic chain (HAC) composed of coupled spin-trimersand hosts a reverse hierarchy of exchanges ($J_1 < J_2$) as opposed to $Cu_3(P_2O_6OH)_2$ [137, 126]. Its crystal structure consists of linear chains of $Cu_3O_8$ trimers, where each trimer is formed by three edge-sharing $CuO_4$ square planes [18]. The magnetic $Cu^{2+}$ ions within these planes each carry spin-$1/2$, and the dominant magnetic interactions are antiferromagnetic super-exchange couplings. Within a trimer, the nearest-neighbor (NN) super-exchange interaction $J_1$ connects adjacent copper ions via oxygen bridges. The trimers are coupled to each other through a next-nearest-neighbor (NNN) super-exchange interaction $J_2 = \alpha J_1$, mediated by oxygen, germanium, and oxygen ions. Additionally, there is an intra-trimer NNN interaction $J_3 = \beta J_1$ between the two edge spins of a trimer, which introduces frustration into the system. For $\alpha = 0$, the trimers are isolated; for $\alpha = 1$ and $J_3 = 0$, the model reduces to the uniform HAC. In $Na_2Cu_3Ge_4O_{12}$, the experimentally determined parameters are $J_1 = 235$ K, $\alpha = 0.18$, and $\beta = 0.18$, indicating that the strongest interaction is within the trimer ($J_1 > J_2$)[18, 137].

In contrast, $Cu_3(P_2O_6OH)_2$ exhibits the same basic trimer configuration, but with the opposite hierarchy of exchange interactions: the inter-trimer coupling $J_2$ is stronger than the intra-trimer coupling $J_1$ ($J_1 < J_2$)[126, 68]. Thus, in $Cu_3(P_2O_6OH)_2$, the magnetic chains are composed of weakly bound trimers that are more strongly coupled to each other via $J_2$, whereas in $Na_2Cu_3Ge_4O_{12}$, the intra-trimer interaction $J_1$ dominates and the coupling between trimers is weaker. This difference in the relative strengths of $J_1$ and $J_2$ leads to distinct magnetic properties and excitation spectra in the two materials. Both systems, however, serve as model platforms for studying quantum magnetism in trimerized spin chains, with $Na_2Cu_3Ge_4O_{12}$ representing the case of strong intra-trimer coupling and $Cu_3(P_2O_6OH)_2$ the case of strong inter-trimer coupling.

### 1.2.2 Phase diagram:

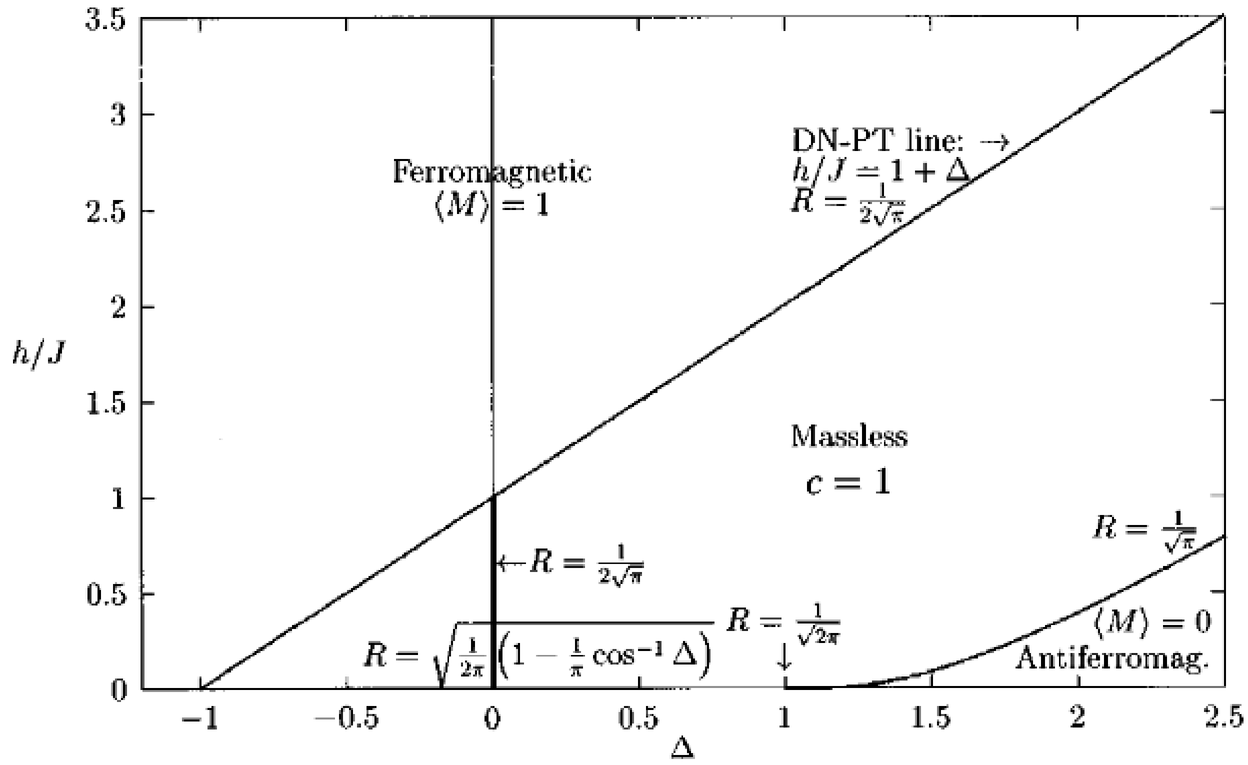

Figure 1.6: Magnetic phase diagram of the spin-$\frac{1}{2}$ XXZ chain in the presence of a longitudinal magnetic field [27]. The horizontal axis represents the anisotropy $\Delta$, while the vertical axis corresponds to the applied field $h$. For $|\Delta| < 1$, the ground state is a critical Luttinger liquid; for $\Delta > 1$, a gapped antiferromagnetic phase appears at low field; and for $\Delta < -1$, the ground state becomes ferromagnetic. At sufficiently large $h$, the system crosses into a fully polarized phase. The boundaries between these regimes are obtained exactly from Bethe ansatz solutions, highlighting the model's integrability and its role as a prototype for describing quantum criticality in 1D magnets.

The XXZ model serves as a generic Hamiltonian for one-dimensional spin-$\frac{1}{2}$ systems, encompassing a broad range of low-energy magnetic behaviors depending on the anisotropic exchange interactions and an external magnetic field. The cuprate compounds discussed above are all effectively described as spin-$1/2$ chains with dominant nearest-neighbor exchange, making them special realizations (nearly isotropic Heisenberg-like) of the XXZ model. It is a minimal yet powerful framework to explore the physics of quantum phase transitions and low-dimensional magnetism. Thus, the phase diagram of the XXZ chain offers a unified theoretical framework that captures the quantum phases and critical behavior observed in these materials.

For a one-dimensional chain in an external magnetic field, the Hamiltonian takes the form

$$H_{\mathrm{XXZ}} = J \sum_i \left( S_i^x S_{i+1}^x + S_i^y S_{i+1}^y + \Delta S_i^z S_{i+1}^z \right) - h \sum_i S_i^z, \tag{1.6}$$

where $J$ is the nearest-neighbor exchange coupling, $\Delta$ characterizes the anisotropy of the interaction, $S_i^\alpha$ $(\alpha = x, y, z)$ are spin-$\frac{1}{2}$ operators, and $h$ denotes the strength of the applied field along the $z$-axis.

An important feature of Eq. (1.6) is that the magnetic field couples to the conserved total magnetization of the system, given by

$$\langle M \rangle = \frac{2}{L} \sum_{i=1}^{L} S_i^z,$$

with $L$ the number of lattice sites. Because magnetization is conserved, the role of the magnetic field is analogous to that of a chemical potential: it shifts the energy landscape without altering the underlying integrability of the model. Thus, the Hamiltonian remains exactly solvable via the Bethe ansatz [27] even in the presence of a finite field $h \neq 0$. In the thermodynamic limit, its low-energy sector is described by a conformal field theory with central charge $c = 1$, equivalent to a free compactified boson whose compactification radius depends on both $\Delta$ and the magnetization $\langle M \rangle$ [27].

The richness of this model is most clearly expressed in its phase diagram, which reveals how different ground states emerge depending on the interplay between anisotropy $\Delta$ and the applied field $h$. A schematic representation of the phase diagram is shown in Fig. 1.6.

- **XY regime ($|\Delta| < 1$):** The system realizes a gapless Luttinger liquid, a critical quantum state with power-law correlations.

- **Ising-like regime ($\Delta > 1$):** At low field, the chain stabilizes a gapped antiferromagnetic phase with long-range order along the $z$-direction.
- **Ferromagnetic regime ($\Delta < -1$):** The ground state becomes fully ferromagnetic, with all spins aligned.
- **High-field regime:** Regardless of $\Delta$, increasing $h$ eventually drives the system into a fully polarized (saturated) state, where all spins align with the external field.

This versatility makes the XXZ model not only a cornerstone of quantum integrable systems but also a realistic description of many quasi-one-dimensional materials, including cuprate spin-chain compounds, where experimental observations of magnetization plateaus and critical phenomena can be directly interpreted through this framework.

In summary, the XXZ chain provides a clean theoretical playground where one can trace, in an exact manner, how anisotropy and magnetic field drive transitions between distinct magnetic phases. This phase diagram will serve as a guiding reference for the subsequent discussion of low-dimensional quantum magnetism throughout this thesis.

## 1.3 Scope and Organization

This chapter has provided an overview of the crystal structures, electronic configurations, and phase diagrams of one- and two-dimensional cuprates, highlighting their rich quantum phenomena and the role of strong correlations. While the fundamental models and magnetic properties have been discussed, the mechanisms for probing spin and charge excitations—such as inelastic neutron scattering (INS) and resonant inelastic X-ray scattering (RIXS)—and the detailed excitation spectra remain to be addressed. The central aim of this thesis is to investigate spin dynamics in low-dimensional strongly correlated materials using advanced numerical methods, with a particular focus on interpreting and predicting RIXS experiments that probe these excitations. The thesis is organized as follows:

In chapter 2 we provide a comprehensive overview of experimental techniques and review the current state of research on spin and charge excitations in low-dimensional quantum system, summarizing key experimental findings and theoretical insights with emphasis on insights from Resonant Inelastic X-ray Scattering (RIXS).We highlight how RIXS reveals single- and multi-spin processes, fractionalized quasiparticles, and collective spin dynamics, establishing it as a key probe of quantum magnetism. In chapter 3 we provide theoretical frameworks of RIXS cross section to understand elementary excitations in low-dimensional quantum materials and introduce the numerical methods employed in this thesis, including exact diagonalization (ED) and density matrix renormalization group (DMRG) techniques. In chapter 4 we demonstrates, using linear spin-wave theory and exact diagonalization, that three-magnon excitations in the non-spin-conserving channel are essential for explaining high-energy features in RIXS spectra of two-dimensional antiferromagnets, providing new insight into multi-magnon processes beyond conventional magnon frameworks. In chapter 5 we demonstrate how RIXS reveals emergent fractionalized quasiparticles and field-tuned composite excitations in a trimerized spin-1/2 chain, providing direct predictions for experiments on $Cu_3(P_2O_6OH)_2$.

# Chapter 2

# Probing Elementary Excitations in Quantum Materials: RIXS

In the previous chapter, we introduced low-dimensional quantum systems, focusing on one- and two-dimensional cuprates. These materials exhibit a variety of quantum phases driven by strong electron-electron interactions, such as Fermi-liquid metals, magnetism, superconductivity (SC), Mott insulators (MI), and charge density waves (CDW). Despite the complexity of these systems, their low-energy behavior can often be described in terms of weakly interacting quasiparticles—collective excitations that carry well-defined quantum numbers. Examples include magnons (associated with spin fluctuations), phonons (related to lattice vibrations), and orbitons (linked to orbital degrees of freedom). While this quasiparticle approach simplifies the theoretical description, accurately determining their microscopic properties and dynamical behavior remains a major challenge.

From an experimental perspective, a central objective is to map the dispersion relations of these excitations, revealing how they propagate through the crystal. This objective has led to the development of various spectroscopic techniques capable of probing elementary excitations and the correlation functions that govern material properties. For instance, angle-resolved photoemission spectroscopy (ARPES) is widely used to study charge excitations [42], while inelastic neutron scattering (INS) is a key method for investigating spin excitations [1]. Other techniques, such as optical Raman scattering [14] and non-resonant inelastic X-ray scattering (IXS), provide valuable information on multi-magnon, phonon, and charge excitations [93].

Recently, resonant inelastic X-ray spectroscopy (RIXS) has emerged as a powerful and versatile tool for probing a wide range of elementary excitations, including spin, lattice, orbital, and electronic degrees of freedom [9, 43][Table 2.1]. RIXS complements INS and Raman techniques by offering broad energy coverage and full momentum resolution across the Brillouin zone. In this thesis, we present a theoretical investigation of RIXS excitations in one- and two-dimensional cuprates. ***Resonant inelastic X-ray spectroscopy:*** RIXS is an experimental technique that probes elementary excitations in quantum materials by measuring the energy and momentum transfer of photons scattered from a sample. The process occurs in three stages [9, 82, 55]: *Resonant absorption*: A core electron is excited to an unoccupied or partially occupied state via a dipole-allowed transition, triggered by an incoming X-ray photon whose energy is resonantly tuned to a specific atomic absorption edge, thereby creating a intermediate state with a core hole. *Intermediate-state dynamics*: The highly excited state induces transient interactions between the core hole and valence electrons. *Radiative decay*: The core hole is filled, emitting a photon whose energy and momentum loss encodes information about the collective excitations (e.g., spinons, magnons, orbitons, or charge density waves) of the material. The resonance effect can significantly amplify the inelastic scattering cross section—often by several orders [9, 55, 82] of magnitude—and provides a distinctive approach for investigating charge, magnetic, and orbital properties at specific atomic sites within a crystal. RIXS selectively couples to spin and orbital degrees of freedom through polarization-dependent selection rules, enabling the resolution of **spin-conserving (SC)** and **spin-nonconserving (NSC)** channels. The SC channel involves core-hole states without spin-orbit coupling, typically occurring at the K-edge of the element being probed. The core-level with spin-orbit coupling can induce spin-flip, as spin is not a good quantum number, enabling access to both SC and NSC channels. Thus, RIXS is uniquely suited to study magnetic systems where conventional techniques, such as INS and Raman spectroscopy, face limitations in resolution, momentum range, or material compatibility.

## 2.1 Features of RIXS as an experimental method

Compared to other scattering techniques, RIXS offers several distinctive advantages. First, it provides access to a broad scattering phase space, enabling the measurement of excitations over a

Table 2.1: Accessible Low-energy excitations in RIXS process [43].

| **Excitation** | **Optical Raman, IXS and RIXS at K edges** | **RIXS at L edges** |
|---|---|---|
| Lattice | Electron–phonon coupling | Nonthing extra |
| Spin | Bi-magnon (two magnons at different sites)<br>2-spinon (1D spin-1/2 systems) | 1-magnon (with large valence spin–orbit)<br>+1-magnon (direct);<br>+2-magnon (on the same site);<br>+3-magnon (on the same site) |
| Charge | Plasmon<br>Phason mode (charge density wave) | Nonthing extra |
| Orbital | Orbiton (dd excitation) | +Spin–orbiton |

wide range of energy and momentum transfers. RIXS is highly sensitive to the polarization of incident and scattered photons, which allows selective probing of different types of excitations through polarization-dependent selection rules. The technique is also element- and orbital-specific, as the resonance condition can be tuned to particular atomic absorption edges, making it possible to investigate specific electronic states within complex materials [9, 43]. Another important feature of RIXS is its bulk sensitivity, which enables the study of intrinsic material properties without being limited to surface effects. Additionally, RIXS requires only small sample volumes, making it suitable for investigating materials that are difficult to synthesize in large quantities. These unique capabilities make RIXS a versatile and powerful tool for exploring the fundamental excitations (see Table 2.1 from [43]) in quantum materials. The following sections provide a more detailed discussion of each feature and its implications for experimental research .

1. One of the key strengths of RIXS is its ability to simultaneously resolve both the energy and momentum transferred during photon scattering. When comparing the energies of neutrons,

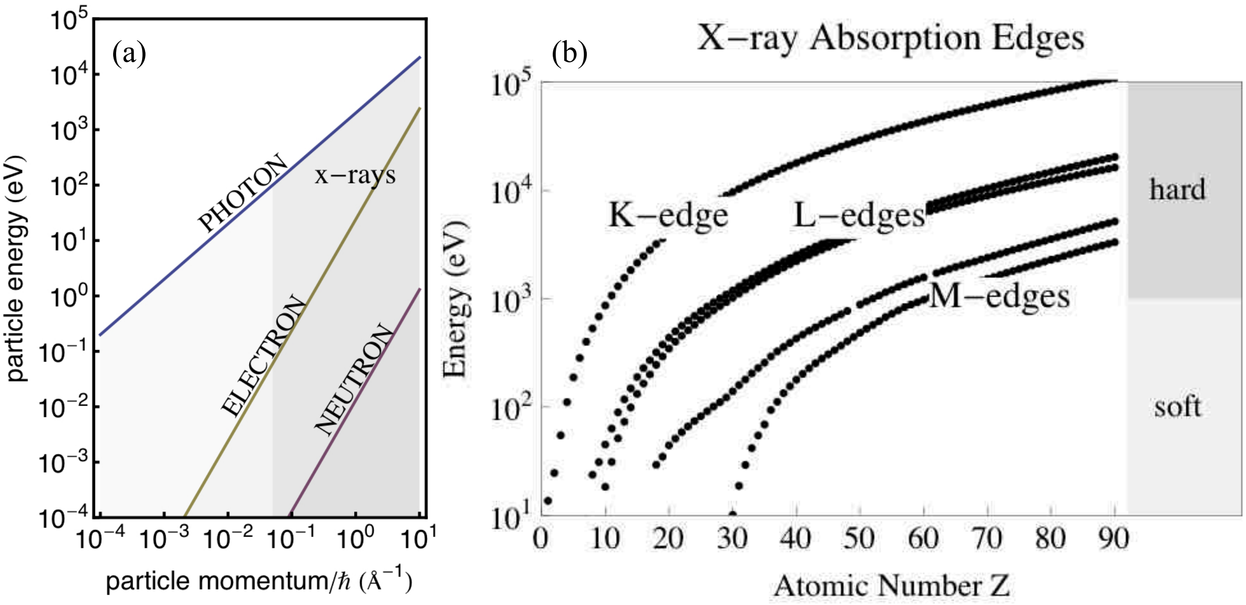

Figure 2.1: Adapted from Ref. [9]. Panel (a) illustrates the kinetic energy and momentum ranges accessible to various elementary particles commonly employed in inelastic scattering experiments. The scattering phase space—representing the range of energy and momentum transfer achievable—is shown for x-rays (blue), electrons (brown), and neutrons (red). Panel (b) presents the energies of characteristic x-ray absorption edges ($K$, $L_1$, $L_3$, $M_1$, and $M_5$) as a function of atomic number $Z$. X-ray energies below 1 keV are classified as soft, while those above are considered hard.

electrons, and x-ray photons with wavelengths similar to the interatomic distances in solids (a few angstroms), x-ray photons possess significantly higher energies than neutrons or electrons, as illustrated in Fig. 2.1(a). This results in a much larger scattering phase space for x-rays—the range of energy and momentum that can be exchanged in a scattering event—making RIXS uniquely capable among spectroscopic techniques. Unlike experiments using visible or infrared light, which are limited in the energy and momentum they can access, RIXS enables the exploration of the full dispersion relations[9, 43] of low-energy excitations in solids, providing comprehensive insight into their fundamental properties.

2. Another notable advantage of RIXS is its ability to exploit photon polarization. By analyzing the polarization of both the incident and scattered photons, researchers can disentangle the nature of the excitations generated within the material. This polarization analysis, guided by selection rules,

enables the identification of the symmetry and character of various excitations[9, 7, 164, 70, 22]. While most experimental setups routinely vary the polarization of the incoming photons, only a limited number of facilities currently allow for the measurement of the scattered photon's polarization [25, 66]. A crucial aspect of polarization changes in RIXS is their direct connection to angular momentum transfer [164, 70, 22]. When the polarization of a photon changes during scattering, it signifies that angular momentum has been exchanged between the photon and the material. Due to the conservation of angular momentum, any angular momentum lost by the scattered photon is imparted to the elementary excitations within the solid. This feature provides a powerful means to probe and characterize the underlying quantum states and excitations in complex materials.

3. RIXS is *element- and orbital-specific*[9]: This technique achieves chemical sensitivity by tuning the incident photon energy to match particular atomic transitions, known as absorption edges, of different elements within a material. By selecting the appropriate absorption edge, RIXS can distinguish between the same element located at sites with different chemical environments, valence states, or crystallographic positions—provided their absorption edges are sufficiently separated. Furthermore, the nature of the electronic excitations that can be probed depends on which x-ray edge is chosen for a given element (for example, the $K$ edge excites $1s$ core electrons, the $L$ edge targets electrons in the $n = 2$ shell, and the $M$ edge involves $n = 3$ electrons). Each edge corresponds to transitions involving different core and valence orbitals, allowing researchers to selectively investigate specific electronic states. The characteristic energies of these absorption edges for various elements are illustrated in Fig. 2.1(b).

4. RIXS is *bulk-sensitive* [9, 43, 82]: Unlike techniques that primarily probe surface properties, RIXS enables the investigation of bulk material characteristics, providing access to intrinsic excitations and correlations within the sample. This bulk sensitivity is especially valuable for complex materials, where surface effects can mask or distort the true physical behavior. The penetration depth of resonant x-ray photons depends on both the material and the experimental geometry. Typically, hard x-rays with energies around 10 keV penetrate on the order of a few $\mu$m into the sample,

while soft x-rays near 1 keV reach depths of about 0.1 $\mu$m [9, 43]. This allows RIXS to probe well beneath the surface, yielding information representative of the material's bulk properties.

5. RIXS is highly effective even with small sample volumes. This is because the interaction between photons and matter is much stronger than that of neutrons, allowing for efficient scattering from limited material. Additionally, modern photon sources can produce vastly more photons per second, focused into much smaller spots, compared to neutron sources. As a result, RIXS experiments can be performed on tiny samples, thin films, surfaces, and nano-scale objects, as well as on bulk single crystals or powders [9, 43](ofcourse you will loose momentum resolution in thta case). This flexibility greatly expands the range of materials that can be studied, including those that are difficult to synthesize in large quantities.

RIXS is capable of detecting a broad spectrum of charge-neutral excitations [9, 43, 7], such as electron–hole continua, excitons, charge-transfer and $dd$ excitations, lattice vibrations, and magnetic modes. This is possible because the orbital angular momentum of the photon can interact with electron spins, as summarized in Table 2.1. While this versatility makes RIXS a powerful tool, it also introduces complexity to the measured spectra, since multiple excitation channels can contribute simultaneously.

Historically, RIXS was less widely used than ARPES or INS, primarily because it requires a high flux of incident photons to obtain sufficient scattered signal for high-resolution measurements in both energy and momentum. Achieving the necessary resolving power—the ratio of incident photon energy to energy resolution—of about $10^4$ posed significant technical challenges[43, 9]. As a result, earlier RIXS experiments were limited to detecting energy losses of approximately $0.5$ eV or higher, making ARPES and neutron scattering more suitable for probing low-energy excitations near the Fermi level.

However, recent advances in instrumentation have dramatically improved the energy resolution and efficiency of RIXS. These developments now allow researchers to access low-energy excitations with high precision, firmly establishing RIXS as a key technique in the study of quantum materials and condensed matter physics.

## 2.2 Probing Elementary Excitations with RIXS

The elementary excitations within a material fundamentally shape its physical properties, governing phenomena such as electrical and thermal transport, as well as the system's response to external stimuli. In essence, a thorough understanding of the excitation spectrum is tantamount to understanding the material itself.

In the previous chapter 1, we discussed how low-energy phenomena in strongly correlated electron systems, such as transition-metal oxides, are often controlled by interactions at much higher energy scales—typically several electronvolts—due to strong electron-electron correlations. These interactions give rise to a rich tapestry of quantum many-body effects, presenting some of the most challenging problems in contemporary condensed matter physics. The essential physics is often captured by model Hamiltonians, whose parameters must be determined through experimental investigation. Spectroscopic techniques, particularly RIXS, play a crucial role in this process by providing direct access to the excitation spectrum and helping to constrain theoretical models.

In the following sections, we examine the energy and momentum scales relevant to RIXS, highlighting its capability to probe the excitation spectrum of solids. We then provide an overview of the types of elementary excitations that RIXS can access, referencing the key literature [9, 43].

**Excitation Energy and Momentum Scale:** Figure 2.2 illustrates that the spectrum of elementary excitations in solids covers a wide energy range—from high-energy plasmons and charge-transfer excitations (in order of eV ), which influence optical properties, down to lower-energy excitons, $dd$ excitations, magnons, and phonons at the meV scale. RIXS is capable of probing the energy and momentum dependence (dispersion) of all these excitations, since the scattered photon exchanges both energy and momentum with the material in a larger scattering-phasespace [Fig. 2.1(a)].

This capability sets RIXS apart from conventional optical techniques like Raman scattering [45].

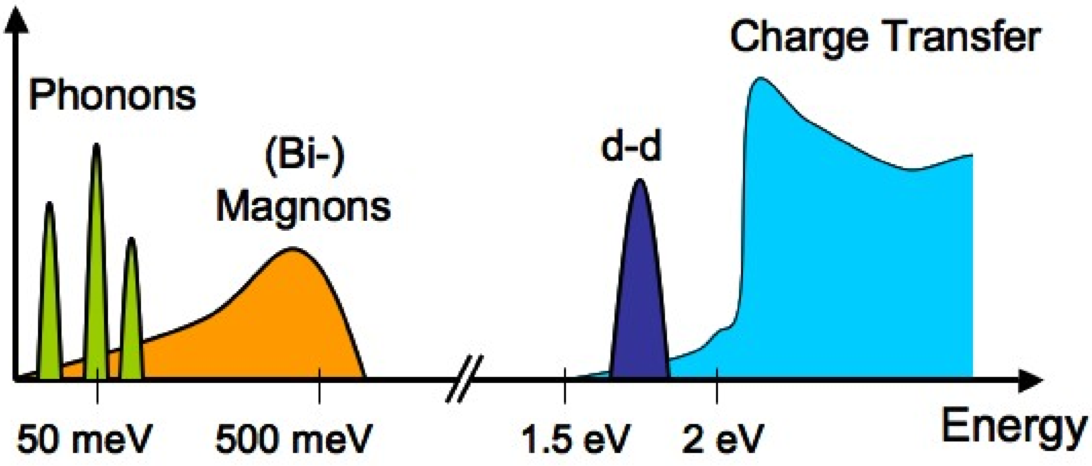

Figure 2.2: Representative elementary excitations in condensed matter systems [9] and their typical energy scales in strongly correlated electron materials, including transition metal oxides.

Photons in the visible range (a few eV) carry very little momentum compared to the typical quasi-momentum of excitations in a solid. For example, a 2 eV photon has a momentum of approximately $\hbar q = 10^{-27}$ kg·m/s, corresponding to a wavevector $q \approx 10^{-3}$ Å$^{-1}$. In contrast, excitations in a crystal with a lattice constant of about 3 Å can have wavevectors up to $q = 2\pi/3 \approx 2$ Å$^{-1}$. Thus, optical light scattering effectively probes only zero-momentum excitations. To investigate the dispersion of excitations across a significant portion of the Brillouin zone, photons with much higher energy—such as x-rays near 1 keV, corresponding to for instance the Cu $L$-edge—are required[9]. RIXS provides this capability, enabling detailed mapping of excitation spectra in quantum materials.

**Overview of elementary excitations** In this paragraph, we briefly outline the various elementary excitations accessible to RIXS, while a detailed discussion of low-dimensional materials—particularly 1D and 2D cuprates—and their phase diagrams is presented in Chapter 1.

*Plasmons:* Plasmons are collective oscillations in the electron density of a material. They can be detected using inelastic X-ray scattering (IXS) or optical techniques, as they occur at finite energy even at zero momentum transfer ($q = 0$). Plasmon-like excitations were also reported in early RIXS studies [79]; however, their resonant enhancement compared to IXS is relatively weak. As a result, limited experimental attention has been devoted to them in RIXS.

*Charge-transfer excitations:* Charge transport in condensed matter systems is governed by the energy cost of moving electrons between sites. In transition-metal oxides, two main energy scales determine this process. The first is the charge-transfer energy, $\Delta = E(d^{n+1}\underline{L}) - E(d^n)$, where $\underline{L}$ denotes a hole on the ligand site, corresponding to an electron hopping from ligand to metal. The second is the on-site Coulomb energy, $U = E(d^{n+1}) + E(d^{n-1}) - 2E(d^n)$, associated with moving a $d$ electron between metal sites. Strongly correlated insulators are classified by the larger of these two energies [184]: if $U > \Delta$, the system is a charge-transfer insulator; if $U < \Delta$, it is a Mott-Hubbard insulator.

Most transition-metal oxides of interest, such as cuprates, nickelates, and manganites, fall in the charge-transfer limit [40, 143, 187, 16], where the lowest-energy optical excitations are charge-transfer in nature. These excitations are central to understanding their physics, raising questions about the gap magnitude (typically a few eV), whether bound excitons form, their degree of localization or mobility, and their lifetimes, symmetries, and temperature dependence. While techniques such as electron-energy-loss spectroscopy (EELS) and optical conductivity have addressed some of these issues[40, 43, 114], RIXS provides a powerful and complementary probe, and has been extensively applied to investigate them.

*Crystal Field and Orbital Excitations:* In many strongly correlated systems, the valence electrons possess an orbital degree of freedom, meaning they can occupy different orbital states. Orbitally active ions are typically magnetic, with partially filled outer shells. This orbital degree of freedom influences the physical properties of the solid directly and indirectly, for example, through coupling to the lattice via the orbital charge distribution, or by determining spin-spin interactions through the Goodenough–Kanamori superexchange rules [10, 61, 85] as discussed in chapter 1.

In many Mott insulators, orbital physics is dominated by the crystal field [117], which splits the orbital levels and fixes the ground state through local, single-ion effects[117, 143, 127]. Excitations between these crystal-field-split $d$ orbitals are known as $dd$ excitations and are routinely observed and well understood in RIXS [147].

If the crystal field splitting is small, orbital degeneracy may persist, allowing inter-site superexchange to generate collective orbital excitations—called orbitons, analogous to magnons [147, 82]. Although definitive proof remains elusive, RIXS offers unique advantages in detecting such modes.

*Magnetic excitations:* Magnetism and long-range magnetic order are among the most well-known consequences of electron–electron interactions in solids. When magnetic order—ferro-, ferri-, or antiferromagnetic—emerges, the global spin-rotation symmetry is broken, giving rise to collective magnetic excitations. The associated low-energy quasiparticles, magnons, and their mutual interactions govern the material's low-temperature magnetic properties. In cuprates, magnon energies can reach $\sim 0.3$ eV with momenta up to $\sim 1$ Å$^{-1}$. Magnon dispersions have been measured at the Cu $L$-edge in thin films of $La_2CuO_4$ [7, 26, 16], and bi-magnon excitations have been observed at the $K$-edge [55, 73].

Disruption of long-range order—through quantum fluctuations from mobile charge carriers or frustration of spin interactions—can produce spin-liquid ground states. RIXS can also detect fractionalized spinon excitations from such states, including spinons [95] and triplons [146].

## 2.3 The RIXS Process

Even though we have discussed the RIXS process in the introduction part of this chapter, we will now provide a more detailed and microscopic picture of the resonant inelastic x-ray scattering process in terms of an example, which is crucial for understanding the theoretical framework and calculations presented in this thesis. To illustrate the RIXS process in detail, let us consider copper-oxide materials as a representative example. In copper oxides, the incident photon energy can be tuned to resonate with the copper $K$, $L$, or $M$ absorption edges, each corresponding to the excitation of a different core electron into an unoccupied valence state (see Figs. 2.3(a) and 2.3(b)). The electronic configuration of $Cu^{2+}$ is [Ar] $3d^9$, where the $3d$ shell is partially filled—a hallmark of transition metal ions.

At the copper $K$-edge, a $1s$ electron is promoted to a $4p$ state by a photon with energy near 9000 eV [55, 73, 40], placing this transition in the hard x-ray regime. The $L_{2,3}$-edge involves the excitation of a $2p$ electron to the $3d$ shell at approximately 900 eV [7, 26], while the $M_{2,3}$-edge corresponds to a $3p \rightarrow 3d$ transition around 80 eV [40, 43], both in the soft x-ray range. Alternatively, by tuning to the oxygen $K$-edge, one can excite an O $1s$ electron into an empty $2p$ state, requiring about 500 eV[40, 43].

Upon absorption of a soft or hard x-ray photon, the system enters a highly excited and unstable intermediate state with a deep core hole. This state decays rapidly, typically within 1–2 femtoseconds [55, 9]. Several decay channels are possible; for example, the Auger process involves a non-radiative transition where an electron fills the core hole and another electron is emitted. However, RIXS is governed by radiative (fluorescent) decay, in which the core hole is filled by an electron and a photon is emitted.

The energy and momentum of the emitted photon can differ from those of the incident photon through two distinct scattering mechanisms: *direct* and *indirect* RIXS. The following discussion clarifies the distinction between these two processes.

### 2.3.1 Direct RIXS

In the direct RIXS process, the incident photon excites a core electron into an unoccupied state within the valence band, as illustrated in Fig. 2.3(a). This excitation leaves behind a core hole. The system then relaxes when an electron from a filled valence state fills the core hole, emitting a scattered photon in the process.

The outcome of this sequence is the creation of an electron-hole pair: an electron occupies a previously empty valence state, while a hole is left in the filled valence band. This electron-hole excitation can move through the material, carrying both energy $\omega_{\mathbf{k}}$ and momentum, $\mathbf{q}$. Conservation laws dictate that the momentum transfer is given by $\mathbf{q} = \mathbf{k}' - \mathbf{k}$ and the energy transfer by $\omega =$

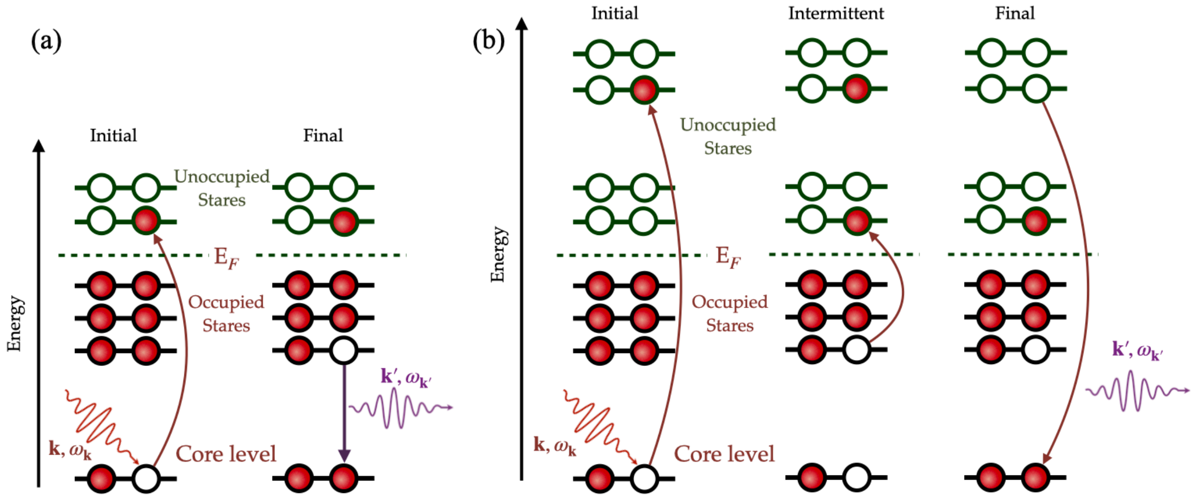

Figure 2.3: Panel (a): Direct RIXS process. The incident x-ray photon excites an electron from a deep core level to an empty valence state. The resulting core hole is subsequently filled by an electron from the valence band, emitting a scattered x-ray photon. This process generates a valence excitation with momentum transfer $\hbar(\mathbf{k}' - \mathbf{k})$ and energy transfer $\hbar(\omega_{\mathbf{k}} - \omega_{\mathbf{k}'})$. Panel (b): Indirect RIXS process. Here, the incident photon excites a core electron into the valence shell. Excitations are produced via the Coulomb interaction $U_c$ between the core hole (and sometimes the excited electron) and the surrounding valence electrons.

$\omega_{\mathbf{k}'} - \omega_{\mathbf{k}}$, where $\hbar\mathbf{k}$ and $\hbar\omega_{\mathbf{k}}$ are the momentum and energy of the incoming photon, and $\hbar\mathbf{k}'$ and $\hbar\omega_{\mathbf{k}'}$ are those of the outgoing photon.

For direct RIXS to occur, both transitions—the initial excitation from the core to the valence state and the subsequent decay from the valence band to refill the core hole—must be allowed. Typical examples include a dipole transition from $1s \rightarrow 2p$ followed by $2p \rightarrow 1s$ decay, as seen at the $K$-edge of elements like oxygen, carbon, and silicon. In transition metals, direct RIXS at the $L$-edge involves $2p \rightarrow 3d$ absorption and $3d \rightarrow 2p$ emission. In these cases, RIXS directly probes the electronic structure of the valence and conduction bands. While the direct transitions largely determine the spectral features, interactions in the intermediate state—such as those arising from the strong core-hole potential—can also influence the observed spectra [9, 55, 82, 137].

### 2.3.2 Indirect RIXS

The indirect RIXS process involves a more subtle mechanism compared to direct RIXS. In this case, the probability of a core electron being directly promoted to a conduction-band state by the incoming photon is low or forbidden by selection rules (of example dipole selection rule). Instead, the photon excites a core electron (for example, from the $1s$ level) into a high-energy, empty state far above the Fermi level—typically several electronvolts higher (for example, from the $4p$ level). The same electron then returns to fill the core hole, as illustrated in Fig. 2.3(b). A well-known example is RIXS at the transition-metal $K$-edges ($1s \rightarrow 4p$ transitions) [9, 55, 82].

If no further interactions occurred, this process would be purely elastic, with no energy loss. However, the creation of a core hole in the intermediate state introduces a strong, localized potential that interacts with the surrounding $3d$ valence electrons. These valence electrons respond by screening the core hole, and in doing so, they are scattered by its potential. This scattering generates electron-hole excitations within the valence band. When the excited electron decays back to the core level, these excitations remain in the system, resulting in an inelastic scattering event.

Thus, indirect RIXS is fundamentally driven by the ”shakeup” of valence electrons caused by the presence of the core hole in the intermediate state. Even when the $1s$ core hole and the excited $4p$ electron form a bound exciton near the absorption edge, the essential physics remains unchanged—the valence electrons interact with this exciton, leading to the creation of excitations [9, 55, 82, 137, 125]. This mechanism enables indirect RIXS to probe a wide range of collective excitations in quantum materials.

## 2.4 Comparison between RIXS and other scattering techniques

Resonant Inelastic X-ray Scattering (RIXS) is part of a broader family of scattering techniques used to study the collective excitations of quantum materials. These excitations—such as phonons, magnons, orbitons, and plasmons—are distinct from single-particle excitations, which are typically probed by Angle-Resolved Photoemission Spectroscopy (ARPES).

RIXS can be viewed as a combination of X-ray Absorption Spectroscopy (XAS) and X-ray Emission Spectroscopy (XES). First, an incident photon excites a deep-lying core electron into the valence shell or conduction band, creating a core hole (XAS step). Second, the system decays radiatively, emitting a photon whose energy is measured (XES step). When the incident photon energy is tuned to an absorption edge, the scattering becomes *resonant*, enhancing sensitivity to specific elements, orbital symmetries, and spin states. The core-level resonance also introduces additional selection rules and polarization dependencies, enabling measurements such as magnetic circular dichroism (MCD).

We have already introduced the principles and capabilities of RIXS. Here we only compare it with related probes. A concise comparative overview of related spectroscopic techniques is provided in Table 2.2 [43] at the end of this chapter.

### 2.4.1 Non-Resonant Inelastic X-ray Scattering (IXS)

Inelastic X-ray Scattering (IXS) is the non-resonant analogue of RIXS, in which photons scatter from the charge density without involving core-level resonances. Governed mainly by the Thomson scattering cross-section, IXS is particularly sensitive to collective charge excitations such as phonons and plasmons [150, 15]. Because it does not require resonance, the incident x-ray energy can be freely tuned, enabling sub-meV resolution using backscattering crystal optics. IXS is a powerful probe of phonons across the Brillouin zone but is less effective for magnetic excitations due to the small magnetic scattering cross-section.

### 2.4.2 Electron Energy Loss Spectroscopy (EELS)

EELS is the electron-based analogue of IXS and involves inelastic scattering of electrons from the sample [78, 4]. Two geometries are common:

- **Transmission EELS (T-EELS)** uses high-energy (keV) electrons to probe bulk excitations in thin samples [132, 133].

- **Reflection EELS (R-EELS)** employs lower-energy (10–100 eV) electrons to probe surface excitations [170].

EELS offers high sensitivity at low momentum transfers ($q \approx 0$) but suffers from multiple scattering and is incompatible with strong magnetic fields.

### 2.4.3 Raman Scattering

Optical Raman scattering is conceptually similar to RIXS but uses visible or ultraviolet photons, restricting momentum transfer to near the Brillouin zone center. Raman can probe low-energy excitations with excellent energy resolution, and resonant Raman scattering can enhance specific modes. RIXS complements Raman by accessing the full Brillouin zone in the soft to hard x-ray regime.

### 2.4.4 Inelastic Neutron Scattering (INS)

Inelastic Neutron Scattering (INS) probes phonons and magnetic excitations via neutron-nucleus and neutron-spin interactions [153, 171, 71, 35]. INS routinely achieves sub-meV resolution, making it powerful for low-energy dynamics, but requires large sample volumes due to the weak neutron-matter interaction.

### 2.4.5 Comparative Advantages and Constraints

The performance of RIXS depends on the photon energy regime:

- **Soft x-ray RIXS**: high resolution (20–40 meV), limited momentum coverage.
- **Hard x-ray RIXS**: full Brillouin zone access, lower resolution.

Regarding sample environments:

- INS: compatible with high fields and ultra-low temperatures.
- Hard x-ray RIXS: feasible under high pressure.

- Soft x-ray RIXS: vacuum and geometry limitations.
- EELS: restricted in magnetic fields and high-pressure setups.

In summary, RIXS uniquely combines element specificity, momentum resolution, and sensitivity to charge, orbital, and spin excitations. IXS excels in phonon mapping with ultra-high resolution, EELS probes low-$q$ excitations, Raman accesses zone-center modes, and INS provides unmatched access to low-energy spin and lattice dynamics in bulk materials. A comprehensive understanding of quantum materials often emerges from combining these complementary techniques.

## 2.5 A short Review of RIXS findings in low dimensional quantum magnets

Over the past decade, resonant RIXS has emerged as a powerful probe of single- [7] and multi-spin excitations [55] in correlated quantum materials. Traditionally, INS has been the primary method to study magnetic correlations by measuring low-energy magnon dispersions and the dynamic susceptibility $\chi(\mathbf{q}, \omega)$ [9, 43]. Although highly precise, INS requires large single crystals and faces challenges in materials containing neutron-absorbing elements such as Cd or Gd [Sec. 2.4.4]. In contrast, RIXS uses photons that, through spin–orbit coupling, can transfer angular momentum $\Delta L_z = 0, 1, 2$ to spin degrees of freedom, enabling both single- ($\Delta S_z = 1$) and multi-magnon ($\Delta S_z = 2$) excitations [161, 7, 55]. Recent advances in instrumentation have improved the energy resolution to below $0.1$ eV, allowing direct observation of elementary magnetic excitations. Benchmark RIXS studies on NiO, $La_2CuO_4$ [26, 24, 73], and $Sr_2CuO_3$ [145] have demonstrated its capability to probe Heisenberg magnetism across three, two, and one dimensions. The detection of two-triplon excitations in $Sr_{14}Cu_{24}O_{41}$ [146] and bi-magnon modes in $La_2CuO_4$ and $CaCuO_2$ [23] confirms the reliability of theoretical interpretations of RIXS spectra. Microscopically, spin excitations arise from strong core-level spin–orbit coupling ($\sim$10 eV [9]), which mediates the interaction between photon-induced orbital moments and electron spins. Even without spin–orbit effects, magnetic scattering can occur in the $\Delta L_z = 0$ channel, analogous to two-magnon Raman processes [45], as seen at transition-metal and oxygen $K$-edges [73]. Although RIXS offers lower energy resolution than optical probes, its momentum-resolved capability provides unique access to dispersive magnetic phenomena and open questions in quantum magnetism.

This Section is structured to provide a clear overview of how RIXS probes magnetic excitations in quantum magnets. The following Subsections, 2.5.2 and. 2.5.3, present recent theoretical and experimental developments in the study of magnetic materials with interactions confined to one and two dimensions respectively.

### 2.5.1 Coupling to Magnetic Excitations with RIXS

RIXS couples to magnetic excitations through two main channels: *direct* and *indirect* scattering. In **direct RIXS**, accessible at transition-metal (TM) like Ni and Cu $L$ or $M$ edges ($2p, 3p \rightarrow 3d$), the strong spin–orbit coupling of the $2p$ core hole enables single spin-flip processes [26, 82, 9, 43]. For Cu, the $2p$ level splits into $J = 1/2$ ($L_2$) and $J = 3/2$ ($L_3$) states, both resolved in XAS and selectively accessible in RIXS [26]. The coupling between spin and orbital angular momentum allows $\Delta S_z = 1$ excitations that are forbidden in optical spectroscopy.

In **indirect RIXS**, relevant at the transition-metal $K$ edge ($1s \rightarrow 4p$), the core hole modifies local superexchange interactions [55]. This process conserves total spin, giving rise to multi-spin excitations with $\Delta S_z = 0$, such as bimagnons or two-triplon states. A similar mechanism operates at the oxygen $K$ edge [145]. At $L$ and $M$ edges, both channels may contribute simultaneously.

RIXS also probes changes in the magnitude of local magnetic moments, such as $\Delta S = 1$ or 2 transitions in ions like Ni$^{2+}$, governed by Hund's coupling $J_H$ ($\sim$1 eV), which appear at higher energies than conventional $\Delta S = 0$ excitations set by the exchange constant $J$ ($\sim$100 meV). When single spin flips are allowed, RIXS directly probes magnon dispersions [7]: the photon scatters from equivalent atomic sites, producing a collective excitation with momentum $\hbar\mathbf{q}$. The RIXS cross-section then factorizes into a local form factor—set by polarization and geometry—and the

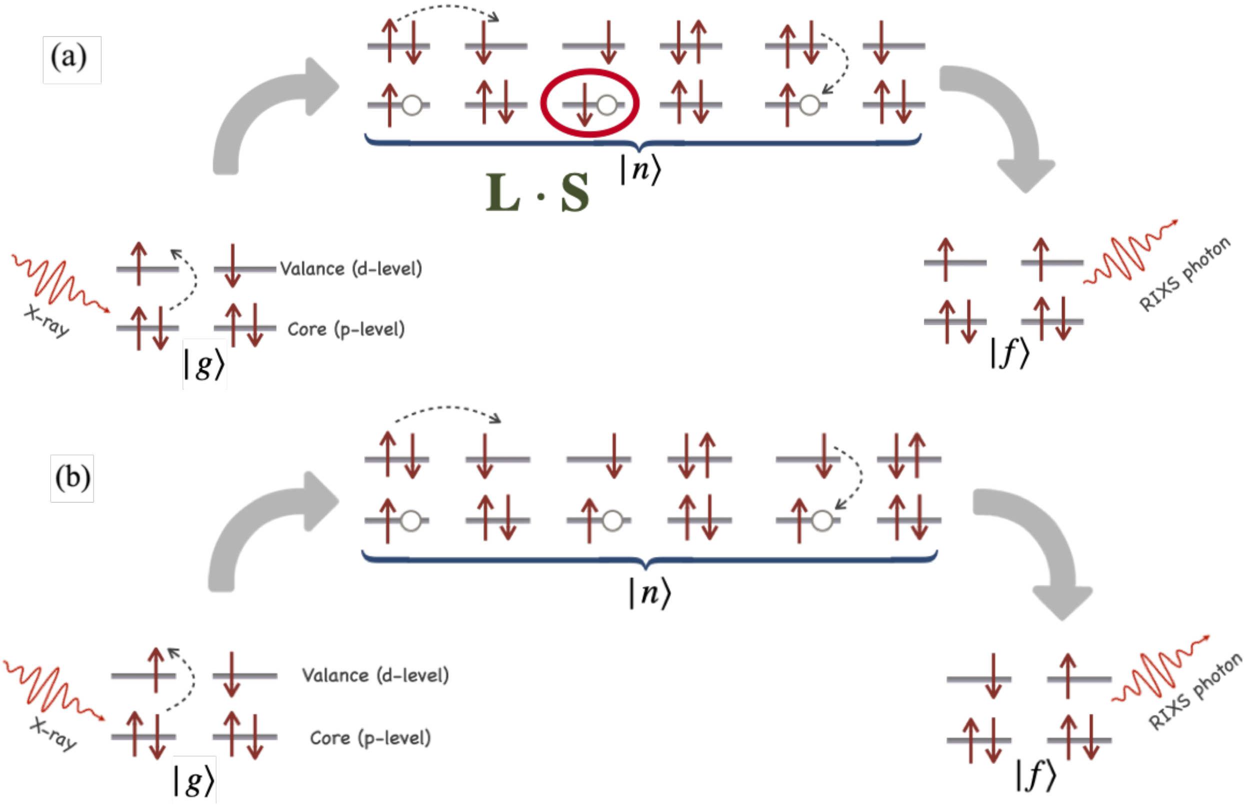

Figure 2.4: This figure illustrates the direct magnetic RIXS process in both non-spin-conserving (NSC) and spin-conserving (SC) channels [137]. Panel (a) shows the NSC mechanism in a two-site, two-orbital model. The sequence highlights the initial state with a fully occupied deep $p$-orbital, the intermediate state where X-ray absorption creates a core hole, and the final state where spin angular momentum is transferred. Panel (b) presents the SC mechanism within the same model. Here, the process again begins and ends with a filled $p$-orbital, while the intermediate state involves a transient core hole. Together, the two panels emphasize how the presence of the intermediate core-hole enables magnetic excitations in both channels through distinct pathways.

spin susceptibility $\chi(\mathbf{q}, \omega)$ [6, 70]. Momentum-resolved RIXS thus provides direct access to the $\mathbf{q}$-dependent structure of correlated spin systems.

### Direct RIXS

Direct RIXS can generate spin-flip excitations without changing the orbital occupation of the valence states. Such processes create single-magnon quasiparticles corresponding to $\Delta S^z = 1$. To illustrate, consider a two-site, two-orbital model (Fig. 2.4) where $p$ orbitals represent core states and $d$ orbitals represent valence states. The ground state $|g\rangle$ has fully filled core levels and half-filled $d$

orbitals with total spin $S^z_T = 0$. Absorption of an incident photon excites a core electron into the $d$ level, producing an intermediate state $|n\rangle$ that can decay into final states with either $\Delta S^z = 0$ or $\pm 1$, corresponding to the spin-conserving (SC) and non-spin-conserving (NSC) channels, respectively.

In the **NSC channel**, the strong spin–orbit coupling of the $p$-orbital core hole plays a crucial role. During the intermediate state, the spin of the core hole can change, preventing the same electron from refilling the core level. Instead, a different valence electron de-excites to fill the hole, leaving behind a flipped spin in the valence shell. This process generates a single spin excitation with $\Delta S^z = \pm 1$, as depicted in Fig. 2.4(a). The NSC channel is therefore particularly effective at probing spin-flip processes and provides direct insight into the spin dynamics and magnetic interactions of the system [95, 145, 125].

In the **SC channel**, by contrast, the scattering does not involve a net change in total spin projection. Instead, the dynamics arise from electron hopping within the valence band, which produces two opposite spin flips. As a result, the total spin projection is conserved with $\Delta S^z = 0$, as illustrated in Fig. 2.4(b). Although spin-conserving, this channel is still sensitive to magnetic excitations and carries valuable information about exchange interactions and collective spin dynamics in the system [95, 145, 125].

### Indirect RIXS

In indirect RIXS, the magnetic system is not coupled to the core hole through a direct spin interaction. Instead, the presence of the core hole modifies the local superexchange interaction $J$, thereby enabling magnetic excitations [55, 149, 73]. Since this perturbation does not commute with the magnetic Hamiltonian, it can generate two-spin-flip excitations with $\Delta S^z = 0$. This mechanism is especially relevant at the transition-metal $K$ edges, where the creation of a core hole alters the magnetic exchange interactions between neighboring spins. The mechanism can be understood through the conventional superexchange process between two half-filled sites. Electron hopping creates a virtual doubly occupied state with energy cost $U$, yielding $J \propto t^2/U$, where $t$ is the hopping amplitude. The creation of a core hole locally alters this energy by $\pm U_c$, leading to an effective

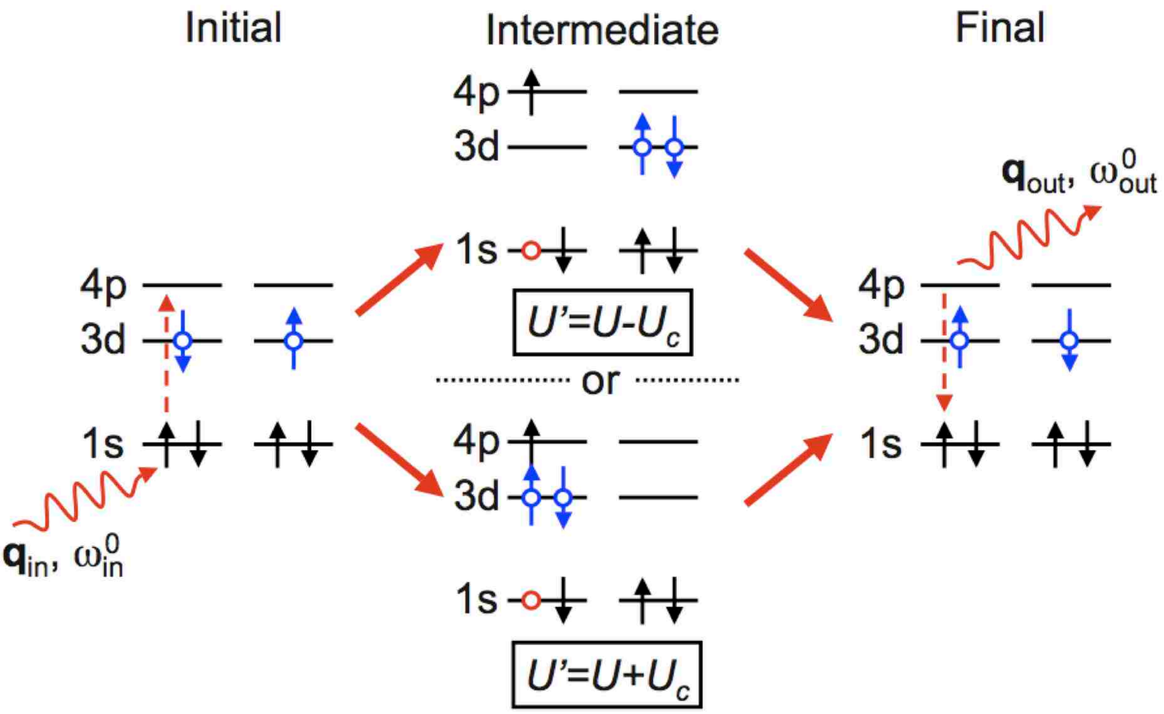

Figure 2.5: Schematic of the indirect magnetic RIXS mechanism at the $Cu^{2+}$ $K$ edge [55]. In the intermediate state, the $3d$ holes may either screen or fail to screen the core hole. As a result, the on-site Coulomb repulsion $U$ is effectively modified to $U'$, which accounts for the additional core-hole potential $U_c$. Open circles denote holes, and arrows indicate their spin orientation.

$U' = U \pm U_c$ and hence a modified $J$. Figure 2.5 illustrates this for the $Cu^{2+}$ $K$ edge [55], where the local change in $J$ drives magnetic excitations in the valence shell.

Experimentally, Cu $K$-edge RIXS measurements on $La_2CuO_4$ and $Nd_2CuO_4$ revealed a clear feature near $500$ meV, attributed to two-magnon excitations [73, 48]. Theoretical modeling within the Ultrashort Core-hole Lifetime (UCL) expansion [44, 55] reproduced this response and showed that longer-range interactions and finite temperature introduce a small single-magnon component to the RIXS signal.

A related process occurs at the transition-metal $L$ edges, where the photo-excited $3d$ electron temporarily disrupts local superexchange bonds. For $Cu^{2+}$, the intermediate $3d^{10}$ configuration blocks exchange entirely, locally setting $J = 0$ [23]. Indirect RIXS is also active at the oxygen

$K$ edge, where strong O $2p$–TM $3d$ hybridization allows the photo-excited electron to modify superexchange pathways and create two-magnon excitations [145].

In summary, indirect RIXS probes magnetic dynamics through core-hole-induced modulation of exchange interactions, naturally generating multi-spin excitations across across different absorption edges.

### 2.5.2 1D systems – Chains and ladders

When magnetic ions are coupled via Heisenberg interactions in a one-dimensional (1D) chain, their collective excitations fractionalize into quasiparticles known as spinons [20]. If two chains are coupled side by side, they form a spin ladder. When the inter-chain coupling (the rungs of the ladder) dominates, the ground state consists of spin singlets localized on the rungs. Excitations out of this ground state correspond to singlet-to-triplet transitions, giving rise to $S = 1$ triplons. These triplons disperse due to coupling along the legs of the ladder. The term **triplon** is used to emphasize that these triplet excitations are distinct from magnons, which arise in long-range ordered antiferromagnets [148]. More complex ladder geometries, such as those with three or more coupled chains, also exist but have not yet been explored by RIXS.

The compound $Sr_{14}Cu_{24}O_{41}$ was the first 1D cuprate studied with RIXS at sufficiently low energies to resolve elementary magnetic excitations [146]. Its crystal structure contains alternating layers of spin chains and ladders. Under pressure, this system becomes superconducting when doped, making it particularly interesting since it does not share the usual two-dimensional $CuO_2$ perovskite structure of high-$T_c$ cuprates. The ladder subsystem hosts a spin-liquid ground state composed of rung singlets, and excitations correspond to dispersive spin-1 triplons. In contrast, the edge-sharing chains have weak superexchange interactions, mediated by $90°$ Cu-O-Cu bonds, and their excitations remain unresolved in current RIXS experiments due to overlap with the elastic line.

At the Cu $L_3$ edge of $Sr_{14}Cu_{24}O_{41}$, [146] observed two-triplon excitations on the spin-liquid

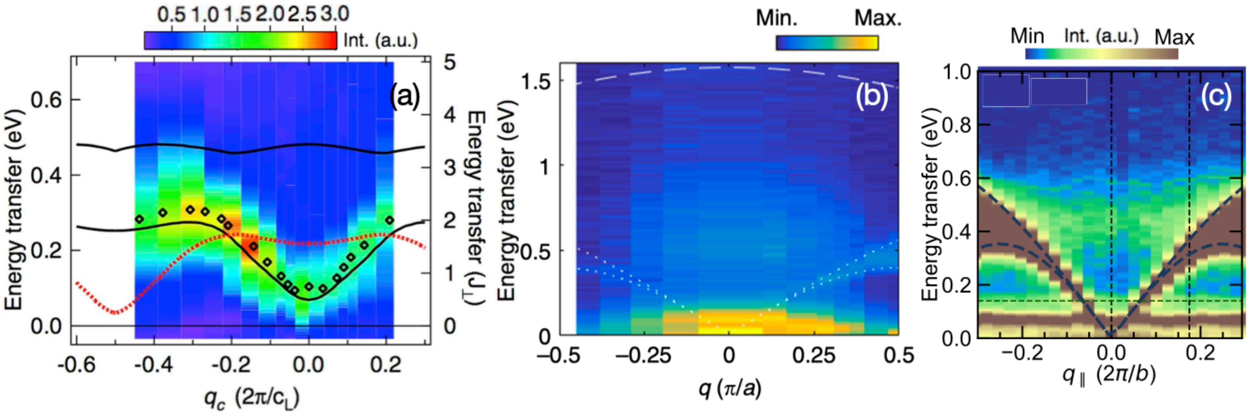

Figure 2.6: This figure brings together experimental and theoretical insights into magnetic excitations observed by RIXS across different edges and models. Panel (a) shows RIXS spectra after subtraction of the elastic contribution [146]. The center of mass, obtained from Gaussian fits, is indicated by open black diamonds, while theoretical dispersions for one-triplon (red dashed line) and two-triplon (black solid line) excitations are superimposed. The right axis is scaled in units of the rung coupling $J$, derived from a single-band Hubbard model. Panel (b) presents experimental oxygen $K$-edge RIXS spectra as a function of momentum and energy transfer [145], highlighting the sensitivity of this edge to collective spin excitations. Panel (c) displays Cu $L_3$-edge RIXS intensity maps along the chain direction [95]. Here, the color scale emphasizes the spectral weight, with brown corresponding to maximum intensity. The two-spinon continuum boundaries are outlined by blue dashed lines, while the upper energy limit of phonon excitations is marked by horizontal green dashed lines.

ladder. These excitations were found to be gapped by $100 \pm 30$ meV at the $\Gamma$-point [Fig. 2.6(a)]. Importantly, this region of the Brillouin zone is inaccessible to inelastic neutron scattering (INS) due to vanishing intensity, although neutron studies can still detect the single-triplon gap away from the $\Gamma$-point. In chapter 5 we will show that even in a simple 1D chain if the periodicity of the spin chain reduced to trimer periodicity it gives rise to new kinds of sharp excitation due to singlet to triplet transition characterized as quasiparticle mode, quite different from the this triplon.

To study spin chains, $Sr_2CuO_3$ serves as a model material. It is a corner-sharing chain with strong antiferromagnetic superexchange ($J \sim$ 200-250 meV) along the chain, making spin excitations well resolved by RIXS. The inter-chain coupling is an order of magnitude smaller, ensuring robust 1D behavior. Recent O-$K$ edge RIXS experiments on $Sr_2CuO_3$ have revealed spin-conserving four-spinon excitations that appear separately outside the conventional two-spinon phasespace [145], as shown in Fig. 2.6(b). The presence of this four-spinon continuum demonstrates that spin dynamics in 1D chains are richer than the simple two-spinon picture. Moreover, the continuum extends up to $\sim 1.5$ eV, well beyond the $\sim 0.5$ eV limit accessible to INS, showcasing the unique strength of RIXS in probing high-energy excitations in low-dimensional magnets. Subsequent Cu-$L_3$ edge RIXS measurements on $SrCuO_2$ confirmed the presence of the same four-spinon continuum [95].

Beyond spin, RIXS has also provided direct evidence for orbital fractionalization in 1D cuprates. In $Sr_2CuO_3$, orbitons—quasiparticles carrying orbital excitations—have been observed with a distinct dispersion across the Brillouin zone, clearly separated from spinons [147]. This demonstrates the unique ability of RIXS to disentangle the spin, charge, and orbital degrees of freedom of the electron in 1D Mott insulators.

In summary, RIXS studies of 1D cuprate chains and ladders have revealed fractionalized quasiparticles such as spinons, triplons, and orbitons. They have also uncovered multi-spinon continua in accessible by INS. These findings establish RIXS as an essential probe of emergent quantum excitations in low-dimensional correlated materials.

### 2.5.3 2D systems – Magnons and Bimagnons

Among the broad class of (quasi) two-dimensional magnetic systems, experimental RIXS studies have so far been carried out almost exclusively on two-dimensional antiferromagnetic cuprates [55, 73, 26, 7, 23]. Theoretical work has also considered related 2D iridates [8]. The emphasis on cuprates is natural, given their central role in high-$T_c$ superconductivity. In the undoped case, cuprates are well described as two-dimensional Heisenberg antiferromagnets that develop long-range magnetic order at low temperatures. Their fundamental excitations are magnons, collective spin-wave modes of the ordered state. Upon carrier doping, long-range magnetic order is suppressed and superconductivity emerges. Besides single-magnon excitations [26, 7], RIXS also has access to higher-order magnetic processes such as bimagnons, which involve the simultaneous creation of two magnons [55, 73]. In the undoped compounds, these low-energy magnetic modes are well separated from higher-energy charge excitations. With doping, however, charge and spin degrees of freedom strongly mix, and so does their RIXS response. In the following, I review how these excitations manifest in RIXS measurements.

### Single magnon excitations

In many cuprates, single spin-flip excitations can be observed in direct RIXS experiments, i.e., at the Cu $L$ and $M$ absorption edges [26, 7]. Examples include $La_2CuO_4$, $CaCuO_2$, $Sr_2CuO_2Cl_2$, and $Nd_2CuO_4$, where the Cu spins (localized in the $3d_{x^2-y^2}$ orbital) lie in the $xy$-plane. These materials are prototypical two-dimensional Heisenberg antiferromagnets, in which a spin-flip excitation corresponds to a single-magnon final state. A similar situation occurs in strongly spin-orbit coupled iridates such as $Sr_2IrO_4$, where RIXS can also resolve elementary magnetic modes [8].

The RIXS cross section for these spin excitations factorizes into two parts: (i) an atomic spin-flip amplitude, which depends on the photon polarization and spin orientation, and (ii) a collective spin susceptibility, which depends solely on the transferred momentum. The connection between the atomic factors and fundamental X-ray absorption spectra has been analyzed in [70]. In antiferromagnetic cuprates, the susceptibility peaks at the ordering vector $\mathbf{q} = (\pi, \pi)$ and decreases linearly to zero near the Brillouin-zone center.

Direct experimental evidence for single-magnon excitations was first obtained at the Cu $L_3$ edge in thin films of $La_2CuO_4$ [26]. The authors demonstrated that the peak in the magnetic RIXS spectrum (Fig. 2.7(a)) follows the magnon dispersion measured by neutron scattering with remarkable accuracy [Fig. 2.7(b)]. This result highlights that RIXS can resolve spin excitations in thin films, where neutron experiments are not feasible.

Further work by [64] measured the magnon dispersion in $Sr_2CuCl_2O_2$, a 2D antiferromagnetic insulator. They found a pronounced 70 meV dispersion between the zone-boundary points ($\pi$,0) and ($\pi$/2,$\pi$/2). Modeling the data with a $t$-$t'$-$t''$-$U$ Hubbard Hamiltonian, the authors concluded that electronic hopping beyond nearest-neighbor Cu sites plays a significant role.

RIXS measurements on underdoped $La_{2-x}Sr_xCuO_4$ ($x = 0.08$) also revealed rich magnetic

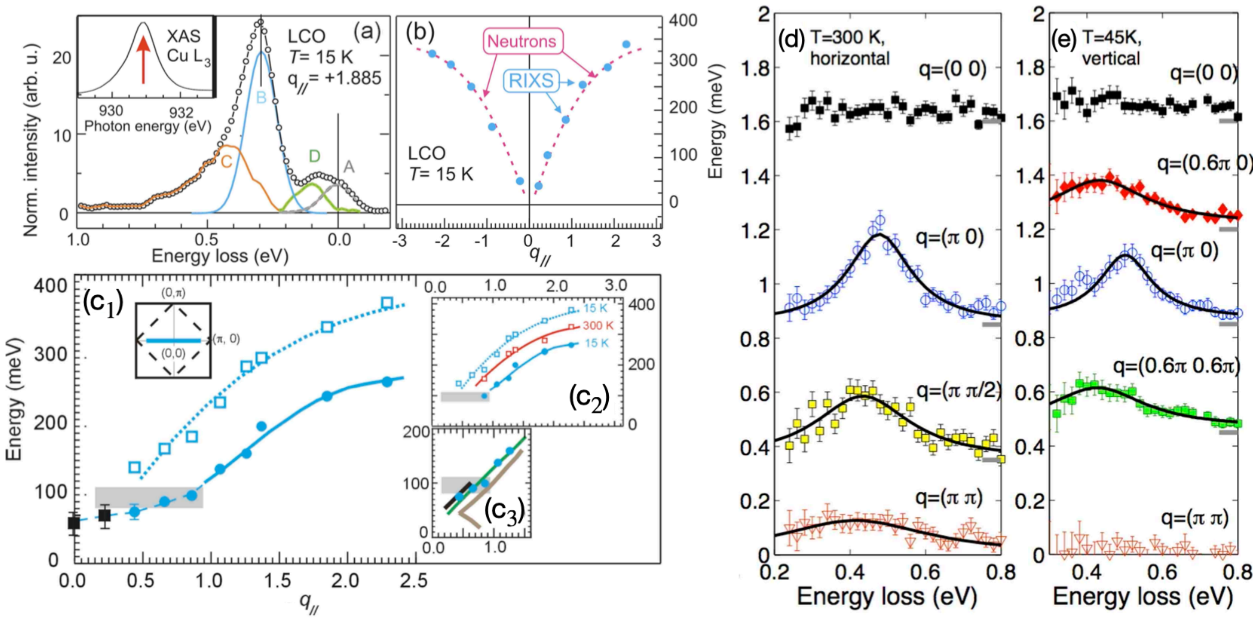

Figure 2.7: Panel (a) shows Cu $L_3$-edge RIXS spectra of La$_2$CuO$_4$, measured with an energy resolution of 140 meV [26]. The momentum transfer, projected onto the CuO$_2$ plane, is along the $(\pi, 0)$ direction. A decomposition of the low-energy spectral weight reveals that the dominant feature follows the single-magnon dispersion. Panel (b) compares single-magnon dispersions obtained from neutron scattering with those measured by RIXS at the Cu $L_3$ edge of La$_2$CuO$_4$. Panel (c) highlights the magnetic excitation spectrum measured by RIXS at the Cu $L_3$ edge in underdoped La2 $-\, x$Sr$_x$CuO$_4$ ($x = 0.08$) at $T = 15$K with an energy resolution of 140 meV. The main panel (c1) shows two distinct branches: a higher-energy LCO-like mode (open blue squares) and a lower-energy branch (filled blue circles). At small $q_{\|}$ (black squares), the separation between the two branches is not well resolved. Inset (c$_2$) compares dispersions measured at room temperature (red diamonds) and low temperature (blue circles and squares). Inset (c$_3$) displays the low-energy branch measured with RIXS near $(0, 0)$ (blue circles), along with neutron scattering results near $(\pi, \pi)$ for different doping levels (thin black, green dashed, and brown thick lines). Panel (d) shows Cu $K$-edge ($1s \to 4p$) RIXS spectra of La$_2$CuO$_4$ measured at selected momentum-transfer points in the two-dimensional Brillouin zone [48, 73]. Panel (e) compares spectra recorded with $\pi$-polarization at room temperature and $\sigma$-polarization at 45 K, using an incident photon energy of 8994 eV. Solid lines correspond to Lorentzian fits, and the elastic peak has been subtracted in all cases.

behavior [26]. The observed asymmetry in the cross section under $\mathbf{q} \to -\mathbf{q}$ could be attributed primarily to magnetic scattering, consistent with theoretical predictions [26, 7]. At low temperatures, two dispersing branches appear: a high-energy mode, within $\sim 10\%$ of the undoped magnon dispersion, and a low-energy mode consistent with neutron data on doped compounds [Fig. 2.7(c)].

Importantly, the equivalence between $\mathbf{q} = (\pi, \pi)$ and $(0, 0)$ no longer holds once long-range order is lost at finite doping. At elevated temperatures, the two branches merge, suggesting that they reflect microscopic phase separation. The excitations extend down to a transferred momentum of 0.44 Å$^{-1}$, implying magnetic domains significantly larger than the associated real-space scale of $\sim$15 Å. Interestingly, this patch size exceeds values extracted from slower probes, leading to the conclusion that the underdoped system is dynamically phase separated.

In iridates, strong relativistic spin-orbit coupling fundamentally reshapes the spin dynamics. For Ir$^{4+}$, the ground state is a Kramers doublet that can be described by an effective pseudo-spin $S = 1/2$. In Sr$_2$IrO$_4$, the $t_{2g}$ analog of La$_2$CuO$_4$, these pseudo-spins interact via superexchange, forming a Heisenberg antiferromagnet. Theoretical calculations for Ir $L$-edge RIXS in octahedral symmetry [8] predict that, in addition to spin-orbit excitations, the technique can directly access the magnon spectrum. Notably, intensity is absent at the $L_2$ edge but strong at the $L_3$ edge, consistent with experimental findings [8].

### Bi-magnon excitations

In *direct* RIXS, the photon can transfer angular momentum to the electron spins, changing the spin angular momentum of the material by one or two units. In *indirect* RIXS this direct transfer is forbidden, so the leading magnetic excitations are *bi-magnons*, which have been observed in many two-dimensional cuprates and are now well understood.

The first momentum-resolved observation of bimagnons in cuprates was reported at the Cu $K$-edge [73]. Using an energy resolution of $120$ meV at $T = 20$ K, La$_2$CuO$_4$ and Nd$_2$CuO$_4$ were studied, and a peak near $500$ meV was observed at $\mathbf{q} = (\pi, 0)$, consistent with a bimagnon excitation. The peak disappeared with hole doping and with polarization perpendicular to the $z$-axis. The intensity was zero at $\mathbf{q} = (0, 0)$ and $(\pi, \pi)$, despite the bimagnon density of states being largest there, and was maximal at $(\pi, 0)$ (see Fig. 2.7(d),(e)).

A follow-up investigation [48] confirmed this momentum dependence and showed that the peak intensity decreases with temperature, vanishing only around $T = 500$ K, well above the Néel temperature $T_N = 320$ K. This behavior resembles Raman and neutron scattering results. The peak width ($\sim 160$ meV) was close to the instrumental resolution, and its energy ($\sim 500$ meV) was higher than the $\sim 400$ meV predicted by magnon theory. This discrepancy was attributed to a strong momentum dependence of magnon-magnon interactions, which are large at $\mathbf{q} = (0, 0)$ but weaker at $(\pi, 0)$. Sr doping caused the peak to shift rapidly to lower energy and lose intensity.

On the theoretical side, calculations for small Hubbard clusters showed that spin-related excitations, such as two-magnon Raman modes, naturally appear in $K$-edge RIXS spectra [161, 67]. It was later proposed that bimagnons couple to the RIXS intermediate state because the core hole locally modifies the superexchange constant $J$ [163, 44] (see Sec. 2.5.1), successfully reproducing the observed lack of intensity at $\mathbf{q} = (0, 0)$ and $(\pi, \pi)$.

Further Hubbard-model studies explored polarization dependence and magnon interactions. In one approach [166], the $B_{1g}$ channel showed a bimagnon dispersing from $\sim 2.8J$ at the zone center to $4J$ at $(\pi, 0)$, while the $A_{1g}$ intensity was strongest at $(\pi, 0)$. A related analysis [46] predicted that the bimagnon peak shifts from $(0, 0)$ to $(\pi, 0)$ as magnon-magnon interactions strengthen, and also found finite intensity at $\mathbf{q} = (\pi, \pi)$.

Finally, bimagnon RIXS scattering via the core-hole was studied at finite temperatures, including longer-range superexchange interactions [55]. Using the *Ultra-short Core-hole Lifetime (UCL) expansion* [44] and comparing with $K$-edge experiments [73], it was shown that higher-order terms in the expansion generate finite bimagnon spectral weight even at $\mathbf{q} = (0, 0)$.

In summary, this chapter has provided a comprehensive overview of the fundamental mechanisms underlying magnetic RIXS processes, emphasizing both theoretical and experimental advances in the study of higher-order spin excitations in cuprates. We have discussed key experimental findings alongside the theoretical models that establish RIXS as a versatile and powerful technique for probing spin dynamics in quantum magnets. The following chapters will present our original results and detail the progress made in extending these concepts to new systems and phenomena.

Table 2.2: Comparison of resonant inelastic X-ray scattering with related techniques [43].

| **Experiment** | **Abbreviation** | **Description** | **Notes** |
|---|---|---|---|
| Inelastic X-ray scattering | IXS | Inelastic scattering of X-rays | 1meV, momentum transfer Not resonant |
| Resonant elastic X-ray scattering | REXS | Resonant elastic X-ray scattering | No energy loss, scattering/diffraction in ordered systems |
| Resonant inelastic X-ray scattering | RIXS | Combination of X-ray absorption and emission spectroscopy | 20 meV Element-specific; sensitive to collective excitations in lattice, charge, orbital, and spin degrees of freedom Polarization options (linear and circular dichroism) |
| Electron energy loss spectroscopy | EELS | Inelastic scattering of electrons | 10 meV, momentum transfer Combination with microscopy Resonant EELS |
| Raman spectroscopy | — | Inelastic scattering of optical/ultraviolet photons | <1 meV, no momentum transfer Resonant Raman |
| Inelastic neutron scattering | INS | Inelastic scattering of neutrons | <1 meV, momentum transfer Sensitive to magnons |
| Angle-resolved photoemission spectroscopy | ARPES | X-ray photoemission | <1 meV, momentum transfer Band mapping of occupied states |

# Chapter 3

# Theoretical frameworks & Numerical Techniques

## 3.1 RIXS Cross-section

In this section, we outline the theoretical framework underlying the RIXS cross-section, which is central to interpreting experimental spectra and connecting them to the underlying quantum excitations.

Earlier we discussed the RIXS process with an example of copper-oxide materials, where the incident photon energy can be tuned to resonate with the copper $K$, $L$, or $M$ absorption edges. Lets try to understand the RIXS cross-section for Cu $L$-edge. In this process incident X-ray photon excites a core electron from a $2p$ orbital into the valence band's state ($3d$), leaving behind a short-lived core hole at $2p$. After a brief interval, this core hole is filled by a valence electron, resulting in the emission of an outgoing photon. The difference in energy between the incoming and outgoing photons, $\omega = \omega_{\text{in}} - \omega_{\text{out}}$, directly corresponds to the energy of the excitation created within the material.

The complete, polarization-dependent RIXS cross-section is given by the Kramers-Heisenberg (KH) formula [43, 9]:

$$I_\epsilon(\mathbf{q},\omega) = \sum_F |\langle F|\, \mathcal{O}_{\mathbf{q},\epsilon}\, |G\rangle|^2\, \delta(E_F - E_G - \omega) \tag{3.1}$$

where $|G\rangle = |g\rangle \otimes |1\rangle_{\epsilon,\omega_{\text{in}}} \otimes |2p^6\rangle$ and $|F\rangle = |f\rangle \otimes |1\rangle_{\epsilon',\omega_{\text{out}}} \otimes |2p^6\rangle$ denote the initial and final states including valence ($|g\rangle, |f\rangle$), photon ($|1\rangle_{\epsilon,\omega_{\text{in}}}, |1\rangle_{\epsilon',\omega_{\text{out}}}$), and core levels ($|2p^6\rangle$). The energies are $E_G = E_g + E_{2p^6} + \omega_{\text{in}}$ and $E_F = E_f + E_{2p^6} + \omega_{\text{out}}$.

The operator $\mathcal{O}_{\mathbf{q},\hat{\epsilon}} = 1/\sqrt{L}\sum_j e^{i\mathbf{q}\cdot j}\mathcal{O}_{j,\hat{\epsilon}}$ captures the intermediate-state evolution in the RIXS process:

$$\mathcal{O}_{j,\epsilon} = D^{\dagger}_{j,\epsilon^F}\frac{1}{\omega_{\text{in}} - \mathcal{H} + i\Gamma} D_{j,\epsilon^I} \tag{3.2}$$

*Note: Equation (3.1) follows from second-order time-dependent perturbation theory in the light–matter interaction. At resonance, the intermediate-state energy denominator becomes small, making the second-order term dominant and gives rise to the Kramers–Heisenberg scattering amplitude.* Here we consider a system with $L$ lattice sites, where the polarization-dependent dipole transition operators for the incoming ($\hat{\epsilon}^I$) and outgoing ($\hat{\epsilon}^F$) photons are defined as $D_{j,\hat{\epsilon}^{F/I}} = \sum_{\sigma,\alpha,\beta}\left(A_{\alpha}^{\hat{\epsilon}^{F/I}}\, p^{\dagger}_{j\alpha\sigma} d_{j\sigma} + \text{h.c.}\right)$, where $p_{j\alpha\sigma}$ and $d_{j\sigma}$ annihilate a hole in the $2p$ and $3d$ shells, respectively, with spin $\sigma$. The coefficients $A_{\alpha}^{\hat{\epsilon}^{F/I}}$ are dipole matrix elements between the $2p_{\alpha}$ and $3d_{x^2-y^2}$ orbitals: $A_{\alpha}^{\hat{\epsilon}^{F/I}} = \langle d_{x^2-y^2,\sigma}\,|\,\hat{\epsilon}^{F/I}\cdot\hat{r}\,|\,p_{\alpha\sigma}\rangle$. The parameter $\Gamma$ denotes the inverse core-hole lifetime. At the Cu $L$-edge, the RIXS process involves the sequence: $3d^{*1}2p^0 \rightarrow 3d^{*0}2p^1 \rightarrow 3d^{*1}2p^0$, where $3d^*$ denotes a hole in the single-band notation [77].

We employ the single-band Hubbard model, which captures the essential low-energy physics of correlated materials—particularly relevant for charge and spin excitations in cuprates, as discussed in Chapter 1 probed by RIXS. While directly applicable to cuprates, these results can be generalized to other multi-orbital correlated systems. The Hamiltonian is defined on a two-dimensional square lattice as $\mathcal{H} = H + H_c$, with

$$H = -t\sum_{\langle\mathbf{i},\mathbf{j}\rangle,\sigma} d^{\dagger}_{\mathbf{i}\sigma}d_{\mathbf{j}\sigma} - t'\sum_{\langle\langle\mathbf{i},\mathbf{j}\rangle\rangle,\sigma} d^{\dagger}_{\mathbf{i}\sigma}d_{\mathbf{j}\sigma} + U\sum_{\mathbf{i}} n^{d}_{\mathbf{i}\uparrow}n^{d}_{\mathbf{i}\downarrow}, \tag{3.3}$$

$$H_c = (\epsilon^d - \epsilon^p)\sum_{\mathbf{i},\alpha,\sigma} n^{p}_{\mathbf{i}\alpha\sigma} + U_c\sum_{\mathbf{i},\alpha,\sigma,\sigma'} n^{d}_{\mathbf{i}\sigma}n^{p}_{\mathbf{i}\alpha\sigma'} + \lambda\sum_{\mathbf{i},\alpha,\alpha',\sigma,\sigma'} p^{\dagger}_{\mathbf{i}\alpha\sigma}\,\chi^{\sigma\sigma'}_{\alpha\alpha'}\,p_{\mathbf{i}\alpha'\sigma'}. \tag{3.4}$$

Here, $t$ ($t'$) denotes the nearest- (next-nearest-) neighbor hopping, and $U$ is the on-site Hubbard repulsion. The operator $d^{\dagger}$ in the single-band model creates a $3d^*$ hole, distinct from the physical Cu $3d_{x^2-y^2}$ hole in the multiband model [49, 51, 165, 50, 40]. In $H_c$, the first term accounts for the energy difference ($\epsilon^d - \epsilon^p$) between $3d$ and $2p$ shells, the second term represents the core-hole potential $U_c$, and the third term describes the $2p$ spin-orbit coupling $\lambda$. The spin-orbit matrix elements are defined as $\chi^{\sigma\sigma'}_{\alpha\alpha'} \equiv \langle p_{\alpha\sigma} \,|\, \mathbf{l}\cdot\mathbf{s} \,|\, p_{\alpha'\sigma'} \rangle$, with $\mathbf{l}\cdot\mathbf{s}$ being the spin-orbit coupling operator.

### 3.1.1 Ultra-short core-hole lifetime expansion of Kramers-Heisenberg formalism

The ultra-short core-hole lifetime (UCL) approximation is a powerful simplification for the RIXS cross-section, valid when the intermediate core-hole state has a very short lifetime (on the order of a few femtoseconds), which implies a large inverse lifetime broadening parameter $\Gamma$ (much larger than the relevant energy scales of the intermediate-state Hamiltonian). Within the *fast-collision approximation*, this means that the dynamics of the valence electrons during the intermediate state are effectively "frozen," as the system does not have sufficient time to evolve before the core hole decays. As a result, one can *integrate out* the intermediate state—that is, formally eliminate the explicit dependence on the short-lived core-hole degrees of freedom—thereby reducing the problem to an effective scattering operator that acts only within the valence subspace. When the incident photon energy $\omega_{\text{in}}$ is tuned to resonance with the Cu $L$-edge, the RIXS intensity can be written in the form [82]:

$$I_\epsilon(\mathbf{q},\omega) = |\mathcal{M}_\epsilon|^2 \sum_f \frac{1}{\sqrt{L}} \sum_j e^{i\mathbf{q}\cdot j} \left| \langle f | \tilde{D}_{\text{in},j}\, \tilde{\mathcal{O}}\, \tilde{D}_{\text{out},j} | g \rangle \right|^2 \delta(E_f - E_g - \omega), \tag{3.5}$$

where

$$\tilde{\mathcal{O}} = \frac{1}{-H + i\Gamma}. \tag{3.6}$$

Here, $\mathcal{M}_\epsilon$ is the polarization-dependent atomic form factor (See appendix A.1.4), which incorporates the effect of incoming and outgoing photon polarizations, and $H$ is the *valence-band Hamiltonian*. The states $|g\rangle$ and $|f\rangle$ denote the ground state and excited states of $H$, with corresponding energies $E_g$ and $E_f$.

The operators $\tilde{D}_{\text{in},j}$ and $\tilde{D}_{\text{out},j}$ are the residual parts of the original dipole operators after contributions absorbed into $\mathcal{M}_\epsilon$. Their explicit form depends on the scattering channel under consideration (See Appendix A.1.3). In particular, for the non–spin-conserving (NSC) channel, it has been shown [82] that $\tilde{D}_{\text{in},j}$ reduces to the identity operator, while $\tilde{D}_{\text{out},j}$ corresponds to the spin-flip operator $S_j^x$.

A further simplification is provided by the *ultra-short core-hole lifetime* (UCL) approximation, in which $\tilde{\mathcal{O}}$ is expanded in powers of $H$ over $i\Gamma$:

$$\tilde{\mathcal{O}} = \sum_{l=0}^{\infty} \frac{H^l}{(i\Gamma)^{l+1}}. \tag{3.7}$$

The UCL expansion is valid when the relevant eigenenergy scale of intermediate state Hamiltonian is much much smaller than $\Gamma$ ( for example $4t/\Gamma \ll 1$, a condition satisfied for cuprates at the Cu $L$-edge [95, 82, 125]). Physically, the UCL approach captures the hierarchy of many-body excitations that emerge from successive commutations of the valence Hamiltonian with local operators, providing a systematic route to evaluate single- and multi-spin contributions to the RIXS cross-section. A comprehensive derivation of the UCL expansion, including correlation terms of various orders for different model Hamiltonians, is presented in Appendix A.1.

## 3.2 Exact RIXS vs UCL Expansion

In this section, we test the accuracy of the UCL expansion using a simple two-site model. The analysis and results presented here are reproduced from our recent work [137]. We first calculate the *exact* Kramers-Heisenberg RIXS cross-section for the SC channel (for simplicity), and then compare it with the result from the UCL expansion.

*Model and Parameters:* We use a two-site system with valence and core levels representing $d$ and $p$ orbitals, respectively [137]. The ground state ($|g\rangle$) has fully occupied core ($p$) levels and half-filled valence ($d$) levels, with the total spin projection $S_T^z = 0$ as illustrated in Fig. 3.1(a). The model includes the charge-transfer energy ($\epsilon_d - \epsilon_p$), energy needed to excite an electron from $p$ to $d$), the interaction between core and valence electrons ($U_c$), and the Hubbard interaction ($U$) on the valence sites. We have followed the Hamiltonian in 3.4 simplifying it to two site and neglecting the spin-orbit coupling in the $p$-orbitals, which is only relevant for the non-spin-conserving (NSC)

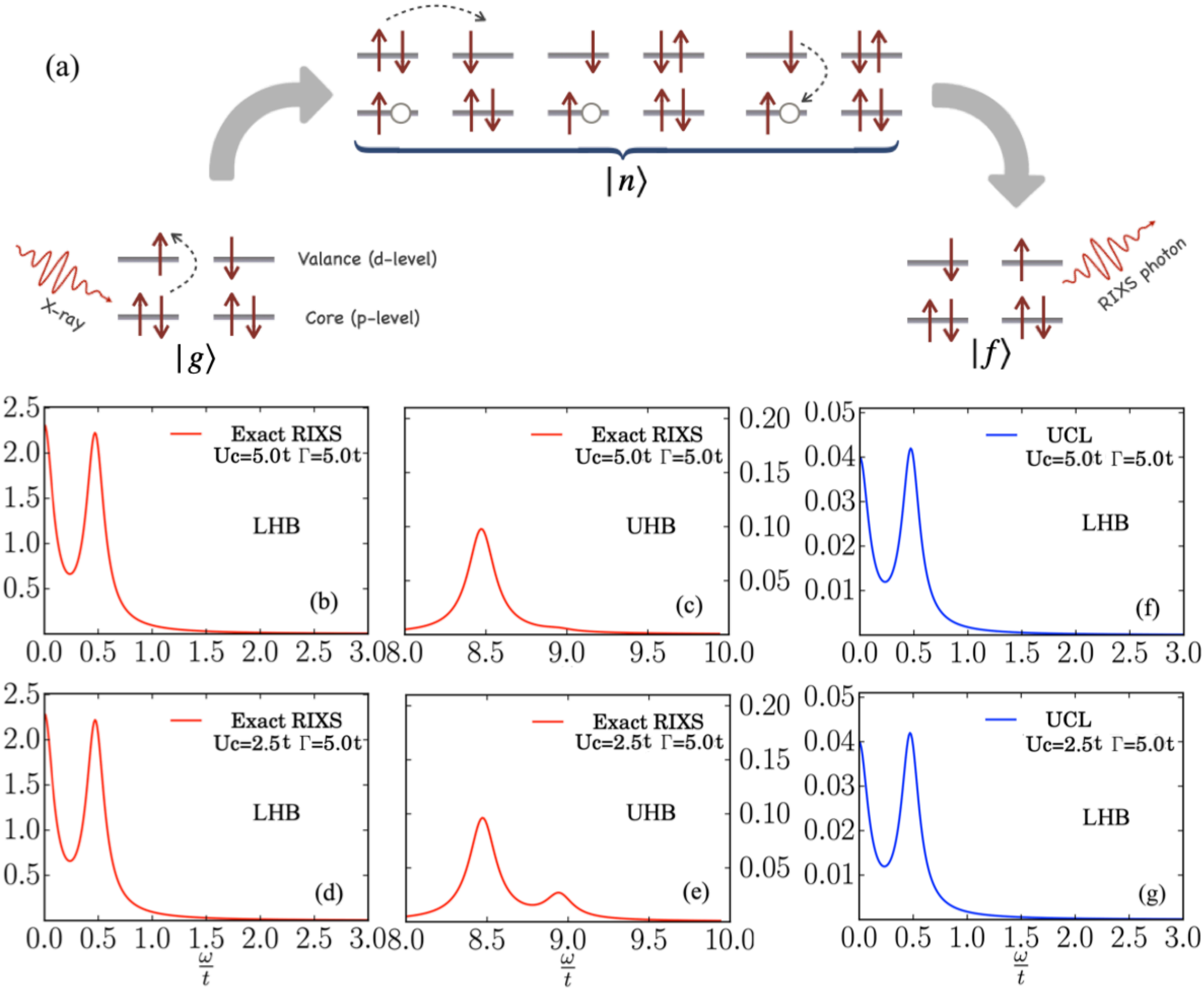

Figure 3.1: Panel (a) depicts the spin-conserving RIXS mechanism in a two-site, two-orbital model, showing the initial, intermediate, and final electronic configurations [137]. The core level, represented as a deep $p$-orbital, is fully occupied before and after the process, while the intermediate state features a core hole created by X-ray absorption. Panels (b) and (d) display the exact RIXS spectra from the lower Hubbard band (LHB) for core-valence interaction strengths $U_c = 5t$ and $U_c = 2.5t$, respectively, as calculated using Eq. 3.1 and 3.2. Panels (c) and (e) present the corresponding spectra from the upper Hubbard band (UHB). Panels (f) and (g) show the low-energy RIXS spectra obtained via the UCL approximation for $U_c = 5t$ and $U_c = 2.5t$. All calculations use a fixed inverse core hole lifetime of $\Gamma = 5t$.

channel. The Hamiltonian is given by:

$$H = -t \sum_{\sigma} d^{\dagger}_{1\sigma} d_{2\sigma} + \text{h.c.} + U \sum_{i} n^{d}_{i\uparrow} n^{d}_{i\downarrow} + (\epsilon_d - \epsilon_p) \sum_{i\sigma} n^{d}_{i\sigma} + U_c \sum_{i\sigma\sigma'} n^{d}_{i\sigma} n^{p}_{i\sigma'}. \tag{3.8}$$

Here, $t$ is the hopping amplitude for valence electrons, and $n^d_{i\sigma}$ and $n^p_{i\sigma}$ are the number operators for valence and core electrons, respectively. Here we are focusing on the SC channel for demonstration purpose.

An incident X-ray photon excites a core electron into the $d$-level. The system then evolves in the excited state, and finally, the core hole is refilled, emitting a RIXS photon. This process is depicted in Fig. 3.1(a). The final state $|f\rangle$ features a double spin-flip, ensuring $S_z^T$ is conserved, as expected for the SC channel.

For our calculations, we set $U = 8t$ and consider two values for $U_c$: $2.5t$ and $5t$. The choice of large $U$ reflects the Heisenberg physics in the lower Hubbard band, and $U_c \approx 2U/3$ is typical for cuprates [82, 137]. The charge-transfer energy $(\epsilon_d - \epsilon_p)$ is set to a large value, $1000t$. To satisfy the RIXS resonance condition, the incoming X-ray energy $\omega_{in}$ is chosen equal to $\epsilon_d - \epsilon_p$, which excites a core electron to the $d$-level at the same site (with $\hbar = 1$). We also set the core-hole lifetime broadening $\Gamma = 5t$, which is much larger than $|4t^2/U(= 0.5)|$.

*Exact RIXS cross-section:—* To calculate the exact RIXS results, we use Eq. 3.1 and insert a complete set of eigenstates $\{|n\rangle\} = |n\rangle_d^{+1} \otimes |0\rangle_{\epsilon,\omega} \otimes |2p^5\rangle$ of $\mathcal{H}$, where the system contains a core-hole $(|2p^5\rangle)$ and the d-level is occupied by three electrons $(|n\rangle_d^{+1})$. Figure 3.1(a) (middle panel) illustrates how the system evolves when the core-hole is present. Panels (b)-(c) and (d)-(e) display the exact RIXS excitations for $U_c = 2.5t$ and $U_c = 5t$, respectively, with $\Gamma = 5t$. Two distinct features are observed: for $U_c = 2.5t$, the low- and high-energy features appear in panels (b) and (c); for $U_c = 5t$, they are shown in panels (d) and (e). The exact RIXS results reveal both the lower (LHB) and upper (UHB) Hubbard sub-bands, which are separated by $U$ [137]. Within the LHB, two features separated by approximately $|4t^2/U| = 0.5$ are visible. The LHB consists of singly occupied sites, and these two levels correspond to singlet and triplet excitations with zero $S_T^z$ in the Heisenberg model, which emerges in the large $U$ limit of the half-filled Hubbard model.

The main influence of $U_c$ arises in the intermediate state, where at least one d-site becomes doubly occupied. The effects of $U$ and $U_c$ appear as small high-energy features separated by $U$, as shown in Fig. 3.1(c) and (e) for the two $U_c$ values. The value of $U_c$ mainly modifies these high-energy features. We have verified that the LHB contribution remains largely unchanged even when $\Gamma = t$ [137]

*UCL-expansion results:*— We now compare these findings with those from the UCL expansion applied to the same model. For the SC channel, we present the $l = 1$ order results, since the $l = 0$ term mainly affects charge fluctuations, which are strongly suppressed at large $U$ and half-filling, as previously noted [82]. Figures 3.1 (f) and (g) display the low-energy UCL RIXS spectra for $U_c = 5t$ and $U_c = 2.5t$, respectively. We observe that the pattern and positions of the low-energy excitations are unchanged compared to the exact low-energy RIXS results. However, the overall intensity is noticeably lower. A direct comparison between panels (b) and (f), and between (d) and (g), shows that while the energy positions of the low-energy excitations are identical, the overall intensity in the UCL spectra is much lower than in the exact results. This discrepancy arises because the exact RIXS spectra include both the elastic peak and background contributions [82], whereas the UCL results contain only inelastic features and are truncated at first order, neglecting higher-order terms. This indicates that varying $U$ and $U_c$ does not significantly affect the results for parameter values relevant to cuprates. These conclusions, drawn from a simple two-site model, are consistent with previous reports in the literature [82].Hence, we use the UCL based approach in this thesis.

## 3.3 Numerical methods

So far, we have established that RIXS is a powerful tool for probing quantum correlations in quantum materials. The UCL expansion offers an effective approach for calculating RIXS spectra and can be explored using simple model calculations. However, despite its simplicity, the UCL expansion does not always yield analytical solutions for RIXS spectra for thermodynamically large systems, especially in complex materials, except in certain exactly solvable cases. Due to the exponential increase in Hilbert space with system size, numerical methods become indispensable for computing RIXS spectra in realistic materials. In this section, we review the numerical methods utilized in this thesis to compute RIXS spectra for realistic strongly correlated systems.

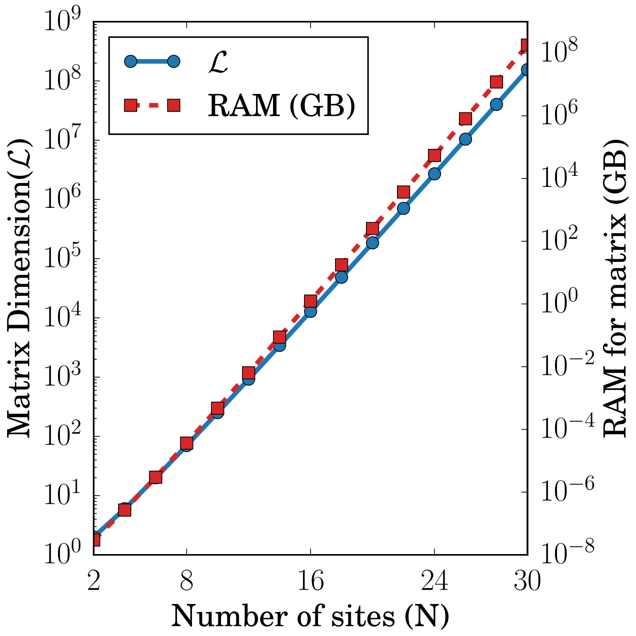

Figure 3.2: Exponential growth of the maximum Hilbert-space dimension and the corresponding RAM requirement for spinless fermions at half filling.

### 3.3.1 Exact Diagonalization

Exact diagonalization (ED) is a powerful numerical technique for solving quantum many-body systems by directly diagonalizing the Hamiltonian matrix in a chosen basis. A key advantage is that ED provides exact results, making it ideal for benchmarking. However, the Hilbert space dimension grows exponentially with system size, restricting calculations to $\lesssim 18$ sites for spinless fermions, $\lesssim 16$ sites for spin-$\frac{1}{2}$ Heisenberg systems, and $\lesssim 12$ sites for spinfull fermions. As depicted in Fig. 3.2, the exponential growth of Hilbert-space dimension and corresponding memory requirement rapidly limits the accessible system size in exact diagonalization studies, as exemplified by spinless fermions at half filling. This limits applicability to small systems but allows direct computation of quantities such as Eq. 3.5, yielding the full RIXS spectrum with no approximations. For the t-J and Heisenberg models, ED enables the calculation of RIXS spectra by evaluating dynamical correlation functions, as implemented in [124]. The method employs high-performance linear algebra routines from LAPACK and Intel's MKL library to efficiently compute eigenvalues, eigenvectors, and spectral functions.

### 3.3.2 Lanczos Method and RIXS Calculations

The Lanczos method [98, 131] is a powerful iterative algorithm for extracting extremal eigenvalues and eigenvectors of large sparse matrices, such as the Hamiltonians describing strongly correlated electron systems. Although primarily suited for ground-state calculations, the Lanczos method can be extended to evaluate excitation [40] spectra relevant to RIXS. However, numerical artifacts such as ghost states and loss of orthogonality demand careful control to obtain physically meaningful results. Starting from a normalized initial vector $|\phi_0\rangle$, typically chosen to have nonzero overlap with the ground state $|\psi_0\rangle$, the method generates an orthogonal basis in which the Hamiltonian becomes tridiagonal:

$$|\phi_{n+1}\rangle = \hat{H}|\phi_n\rangle - a_n|\phi_n\rangle - b_n^2|\phi_{n-1}\rangle, \tag{3.9}$$

with coefficients

$$a_n = \frac{\langle\phi_n|\hat{H}|\phi_n\rangle}{\langle\phi_n|\phi_n\rangle}, \quad b_n^2 = \frac{\langle\phi_n|\phi_n\rangle}{\langle\phi_{n-1}|\phi_{n-1}\rangle}, \tag{3.10}$$

and $b_0 = 0$, $|\phi_{-1}\rangle = 0$. The resulting tridiagonal matrix

$$H = \begin{pmatrix} a_0 & b_1 & 0 & \cdots \\ b_1 & a_1 & b_2 & \cdots \\ 0 & b_2 & a_2 & \cdots \\ \vdots & \vdots & \vdots & \ddots \end{pmatrix} \tag{3.11}$$

can be diagonalized efficiently, with convergence of low-energy states typically reached within $\mathcal{O}(100)$ steps.

#### Application to RIXS

For RIXS, the key quantity is the dynamical correlation function

$$I(\omega) = -\frac{1}{\pi}\,\mathrm{Im}\left[\langle\psi_0|\hat{O}^\dagger \frac{1}{\omega + E_0 + i\epsilon - \hat{H}}\hat{O}|\psi_0\rangle\right], \tag{3.12}$$

where $\hat{O}$ is the effective scattering operator, $E_0$ is the ground-state energy, and $\epsilon$ a small broadening factor. The Lanczos procedure is initialized with

$$|\phi_0\rangle = \frac{\hat{O}|\psi_0\rangle}{\sqrt{\langle\psi_0|\hat{O}^\dagger\hat{O}|\psi_0\rangle}}, \tag{3.13}$$

and iterated to obtain a continued-fraction representation of the Green's function:

$$I(\omega) = -\frac{1}{\pi}\,\mathrm{Im}\left[\frac{\langle\psi_0|\hat{O}^\dagger\hat{O}|\psi_0\rangle}{z - a_0 - \frac{b_1^2}{z-a_1-\frac{b_2^2}{z-a_2-\cdots}}}\right], \tag{3.14}$$

with $z = \omega + E_0 + i\epsilon$. This approach yields excitation energies and spectral weights with high accuracy, making it an essential tool for benchmarking approximate methods and interpreting RIXS spectra in low-dimensional quantum systems.

### 3.3.3 DMRG and MPS-based Time Evolution

The density matrix renormalization group (DMRG) [175, 176] is one of the most powerful numerical techniques for studying strongly correlated one-dimensional (and quasi-one-dimensional) quantum systems. In modern formulations, DMRG is naturally expressed in the language of matrix product states (MPS) and matrix product operators (MPO). This representation not only enables efficient ground-state search but also facilitates time evolution of quantum states using algorithms such as the time-evolving block decimation (TEBD) [168, 169, 167].

**Matrix Product State Representation:**

A generic quantum state of a chain of $L$ sites can be written as

$$|\psi\rangle = \sum_{\sigma_1,\ldots,\sigma_L} c_{\sigma_1\ldots\sigma_L}\,|\sigma_1\rangle \otimes \cdots \otimes |\sigma_L\rangle, \tag{3.15}$$

where $\sigma_i$ labels the local basis at site $i$. In the MPS representation, the coefficients are factorized into products of low-rank tensors:

$$c_{\sigma_1\ldots\sigma_L} = A^{[1]\sigma_1}A^{[2]\sigma_2}\cdots A^{[L]\sigma_L}, \tag{3.16}$$

where $A^{[i]\sigma_i}$ is a matrix (or vector at the boundaries) of dimension $\chi_{i-1} \times \chi_i$. Here, $\chi_i$ is the bond dimension controlling the accuracy of the approximation.

A simple tensor diagram for an open-boundary MPS is shown in Fig. 3.3.

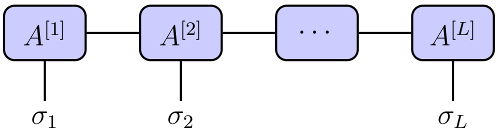

Figure 3.3: Tensor diagram of an open-boundary MPS. Horizontal legs represent virtual bonds of dimension $\chi_i$; vertical legs represent physical indices $\sigma_i$.

### Ground-State Search via DMRG

DMRG works by variationally minimizing the expectation value of the Hamiltonian

$$E = \frac{\langle\psi|H|\psi\rangle}{\langle\psi|\psi\rangle} \tag{3.17}$$

with respect to the tensors $A^{[i]}$ in the MPS representation. This is done by sweeping back and forth along the chain, optimizing one (or two) sites at a time while keeping the rest fixed. The key step is truncation: the reduced density matrix of a bipartition is diagonalized, and only the $\chi$ largest Schmidt values are kept. This ensures an optimal low-rank approximation in the least-squares sense.

### Time Evolution with TEBD

The TEBD algorithm implements real or imaginary time evolution of an MPS under a nearest-neighbor Hamiltonian $H$. We start from the time-dependent Schrödinger equation:

$$|\psi(t+\delta t)\rangle = e^{-iH\delta t}|\psi(t)\rangle. \tag{3.18}$$

If $H$ is a sum of nearest-neighbor terms,

$$H = \sum_j h_{j,j+1}, \tag{3.19}$$

the exponential can be approximated using a second-order Suzuki–Trotter decomposition:

$$e^{-iH\delta t} \approx \left(\prod_{j \text{ odd}} e^{-ih_{j,j+1}\delta t/2}\right)\left(\prod_{j \text{ even}} e^{-ih_{j,j+1}\delta t}\right)\left(\prod_{j \text{ odd}} e^{-ih_{j,j+1}\delta t/2}\right) + \mathcal{O}(\delta t^3). \tag{3.20}$$

Each local evolution operator $U_{j,j+1} = e^{-ih_{j,j+1}\delta t}$ acts on a pair of neighboring sites and can be applied directly to the corresponding MPS tensors. After applying $U_{j,j+1}$, the updated two-site tensor is decomposed back into MPS form via a singular value decomposition (SVD): The bond dimension is truncated back to $\chi_{\text{max}}$ by discarding small singular values, controlling computational cost while maintaining accuracy.

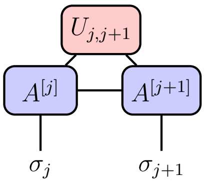

### 3.3.4 Calculation of dynamical correlation

To calculculate dynamical correlation functions, we can use the MPS representation of the ground state calulated using DMRG and apply the time evolution operator to obtain the time-dependent state using TEBD algorithm. A minimal TEBD code requires:

1. Initializing the state as an MPS (ground state from DMRG or a product state).
2. Precomputing the two-site gates $U_{j,j+1}$.
3. Applying gates in the odd-even sequence of the Trotter decomposition.
4. Performing SVD-based truncation after each gate application.
5. Repeating the process for the desired number of time steps.

The choice of $\delta t$ and $\chi_{\text{max}}$ controls the trade-off between accuracy and computational cost. For real-time dynamics, unitarity is preserved up to Trotter errors; for imaginary-time evolution ($\delta t \to$

$-i\delta\tau$), the algorithm projects onto the ground state. Then we can calculate the dynamical correlation function in the frequency domain using the Fourier transform.

# Chapter 4

# Multi-Magnon Excitations in RIXS of 2-D Antiferromagnets

*Chapters 2 and 3 provided a detailed overview of RIXS for investigating magnetic excitations in strongly correlated materials. In this chapter, we focus on the Heisenberg model with both nearest- and next-nearest-neighbor hopping, which is relevant for describing magnetic excitations in the cuprate family (see Sec. 1.1 in Chapter 1). The RIXS cross-section is evaluated within the framework of the ultra-short core-hole lifetime (UCL) expansion of the Kramers–Heisenberg scattering amplitude (Sec. 3.1.1, chapter 3), using linear spin wave theory (LSWT) and exact diagonalization. This chapter covers the results in Ref. [125], consider both spin-conserving (SC) and non-conserving channels (NSC). In addition to the well-studied single- and bi-magnon excitations (See sec. 2.5.3 in chapter 2), we show that three-magnon processes in the NSC channel play a key role in explaining certain features of RIXS spectra in undoped two-dimensional cuprates [125]. This analysis places constraints on the dispersion of three-magnon modes across the Brillouin zone and opens up new directions for probing higher-order quasiparticle excitations with RIXS.*

## 4.1 Introduction

From the discussions in the previous chapters, it is evident that a thorough understanding of quasiparticle excitations is crucial for unraveling the complex behavior of strongly correlated systems such as cuprates and nickelates. Among these materials, high-$T_c$ cuprates have attracted the most attention in condensed matter physics due to their intriguing properties. From the details discussion on high-$T_c$ cuprate in chapter 1, it is clear that even after decades of research, the microscopic pairing mechanism of high-$T_c$ superconductivity is still elusive. Among the various proposed mech-

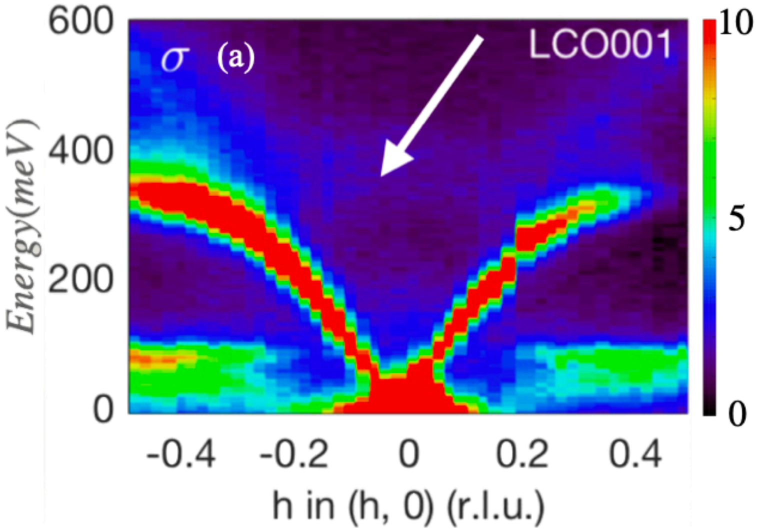

Figure 4.1: RIXS intensity maps for $La_2CuO_4$ at the Cu $L_3$ edge [139]. The white arrow indicates the weakly dispersing broad unknown feature.

anisms, spin fluctuations arising from the antiferromagnetic correlations of the undoped parent compounds are the most promising candidates [143, 40].Traditionally, inelastic neutron scattering (INS) has been the primary technique for investigating spin dynamics. More recently, RIXS has emerged as a powerful complementary method, providing access to high-energy magnetic excitations [57, 9]. Notably, Cu $L$-edge RIXS experiments have detected both single- and multi-magnon excitations [7, 145, 96], establishing RIXS as an essential tool for probing collective spin phenomena beyond the capabilities of conventional INS.

The NSC channel of RIXS has traditionally been viewed as analogous to INS, capturing primarily single-magnon excitations. However, recent Cu L-edge RIXS measurements on the 2D cuprate $La_2CuO_4$ [139] reveal a weakly dispersive, broad high-energy (∼350 meV) feature as shown in Fig. 4.1 that cannot be explained by either single [7]- or bimagnon [55] excitations, indicating the presence of unconventional or higher-order spin excitations beyond the standard magnon framework. The INS community has likewise observed higher-order excitations, including four-spinon continua in 1D cuprates [118, 97], multi-triplon states in spin ladders [122, 177], and fractionalized magnons in 2D cuprates [41]. These findings provide strong motivation for refining the theoretical framework of RIXS, particularly for understanding multi-magnon contributions in 2D cuprates [105, 129, 72, 139, 111, 21].

For example, studies of apical oxygen effects have linked high-energy features near $(\pi, 0)$ in RIXS spectra to magnetic excitations [111], echoing earlier INS interpretations that attributed similar features to magnon-magnon interactions [41]. These complexities underscore the need for robust theoretical approaches to interpret emergent RIXS spectra. Inspired by recent progress in identifying correlation functions corresponding to higher-order terms in the UCL expansion for 1D systems [95], here we extend this analysis to the 2D Heisenberg antiferromagnet, relevant for both cuprates [139] and IL nickelates [104].

In this chapter, we explore distinct magnetic excitations in the SC and NSC channels of the RIXS cross-section by employing standard linear spin-wave theory (LSWT) on the 2D antiferromagnetic Heisenberg model. In particular, we show that the weakly dispersive multi-magnon feature (Fig. 4.1) observed in $La_2CuO_4$ [139] can be qualitatively interpreted as a three-magnon excitation. We further support the LSWT-based interpretation with exact diagonalization results, thereby providing a more comprehensive picture of higher-order magnetic excitations in 2D quantum magnets.

This chapter is organized as follows. In Sec. 4.2, we introduce the spin Hamiltonian for 2D Heisenberg antiferromagnets and describe its mapping to magnon degrees of freedom. We also define the response functions corresponding to higher-order terms in the UCL expansion of the RIXS cross-section. In Sec. 4.4, we present and analyze the SC and NSC channel results, comparing LSWT predictions with exact diagonalization in the NSC channel. Finally, in Sec. 4.5, we summarize our findings and discuss their implications in light of recent Cu $L$-edge RIXS experiments on 2D cuprates.

## 4.2 Model and Method

The two-dimensional (2D) antiferromagnets realized in 2D cuprates consist of the $CuO_2$ plaquettes (see Sec. 1.1 in Chapter 1). The corresponding one-band Hubbard model can be mapped to the spin half Heisenberg model (see Sec. 1.1.3 in Chapter 1) and can very well capture the low energy spin dynamics realized in materials [94, 120, 103, 107]. We, therefore, here, start with the 2D spin model on a square lattice given by

$$H = J_1 \sum_{\langle ij \rangle} \mathbf{S}_i \cdot \mathbf{S}_j + J_2 \sum_{\langle\langle ij \rangle\rangle} \mathbf{S}_i \cdot \mathbf{S}_j. \tag{4.1}$$

Here, $\langle \cdots \rangle$ and $\langle\langle \cdots \rangle\rangle$ indicate the sum over nearest neighbors (NN) and next-nearest neighbors (NNN) sites, respectively. $J_1$ and $J_2$ are the superexchange couplings between NN and NNN sites. $\mathbf{S}_i$ is the spin at site-$i$ The values of the exchange couplings vary across different 2D cuprates due to structural details and Cu-O-Cu bond angles discussed in chapter 1. Typically, for $La_2CuO_4$ (LCO) the $J_1$ lies in the range of 138-148 meV and $J_2 \sim$ 2-10 meV [55, 35]. For $YBa_2Cu_3O_6$ (YBCO) $J_1 \sim$ 93-108 meV and $J_2 \sim -4.7$ meV [173].

### 4.2.1 Linear Spin Wave Theory for $H$:

In our analysis, we choose the $z$-axis as the quantization axis for the antiferromagnet (AFM) and describe the system on a bipartite lattice composed of two sublattices, A and B. We primarily consider nearest-neighbor (NN) AFM exchange interactions. Although next-nearest-neighbor (NNN) AFM exchange is well established in the cuprate family, we also include ferromagnetic (FM) NNN exchange interactions in our study for completeness from a theoretical perspective. To describe the low-energy excitations, we map the spin Hamiltonian onto magnons within the framework of linear spin-wave theory (LSWT), employing the standard bipartite lattice representation with sublattices A and B. In the AFM ground state, the Hamiltonian can then be expressed in terms of bosonic operators through the Holstein–Primakoff (HP) transformation, introduced as follows:

$$\text{For sub lattice A} = \begin{cases} \hat{S}_i^{+} &= \sqrt{2S}\sqrt{1-\frac{a_i^\dagger a_i}{2S}}\,a_i \\ \hat{S}_i^{-} &= \sqrt{2S}a_i^\dagger\sqrt{1-\frac{a_i^\dagger a_i}{2S}} \\ \hat{S}_i^{z} &= S - a_i^\dagger a_i \end{cases} \tag{4.2}$$

$$\text{For sub lattice B} = \begin{cases} \hat{S}_i^{+} &= \sqrt{2S}b_i^\dagger\sqrt{1-\frac{b_i^\dagger b_i}{2S}} \\ \hat{S}_i^{-} &= \sqrt{2S}\sqrt{1-\frac{b_i^\dagger b_i}{2S}}\,b_i \\ \hat{S}_i^{z} &= -S + b_i^\dagger b_i \end{cases} \tag{4.3}$$

To diagonalize the Hamiltonian $\hat{H}$ in Eq: 4.1, we introduce the Bogoliubov transformation in reciprocal space defined as:

$$\begin{bmatrix} \alpha_{\mathbf{k}} \\ \\ \beta^\dagger_{-\mathbf{k}} \end{bmatrix} = \begin{bmatrix} u_{\mathbf{k}} & v_{\mathbf{k}} \\ \\ v_{-\mathbf{k}} & u_{-\mathbf{k}} \end{bmatrix} \begin{bmatrix} a_{\mathbf{k}} \\ \\ b^\dagger_{-\mathbf{k}} \end{bmatrix} \tag{4.4}$$

where,

$$\begin{aligned} u_{\mathbf{k}} &= \sqrt{\frac{1}{2} + \frac{(J_0^{AB} - J_0^{AA} + J_{\mathbf{k}}^{AA})}{2\sqrt{(J_0^{AB} - J_0^{AA} + J_{\mathbf{k}}^{AA})^2 - (J_{\mathbf{k}}^{AB})^2}}} \\ v_{\mathbf{k}} &= sign(J_{\mathbf{k}}^{AB})\sqrt{u_{\mathbf{k}}^2 - \frac{1}{2}} \end{aligned} \tag{4.5}$$

$$\begin{aligned} J_{\mathbf{k}}^{AB} &= J_1(\cos(k_x a) + \cos(k_y a)) \\ J_{\mathbf{k}}^{AA} &= J_{\mathbf{k}}^{AA} = 2J_2(\cos(k_x a)\cos(k_y a)) \end{aligned} \tag{4.6}$$

Here $a$ is the lattice constant.

Hence,

$$\hat{H} = \sum_{\mathbf{k}} \epsilon_{\mathbf{k}}(\alpha_{\mathbf{k}}^\dagger \alpha_{\mathbf{k}} + \beta_{\mathbf{k}}^\dagger \beta_{\mathbf{k}}) + \text{const} \tag{4.7}$$

$$\epsilon_{\mathbf{k}} = 2S\sqrt{(J_0^{AB} - J_0^{AA} + J_{\mathbf{k}}^{AA})^2 - (J_{\mathbf{k}}^{AB})^2} \tag{4.8}$$

Here we use $S = 1/2$ as 2D cuprates are known to host spin-1/2 2D Heisenberg model.

## 4.3 The RIXS intensity

The RIXS cross-section can be expressed within the Kramers–Heisenberg (KH) formalism in the simplified form (Eq. 3.5):

$$I_\epsilon(\mathbf{q},\omega) = |\mathcal{M}_\epsilon|^2 \sum_f \frac{1}{\sqrt{L}} \sum_j e^{i\mathbf{q}\cdot j} \left| \langle f|\tilde{D}_{\text{in},j}\,\tilde{O}\,\tilde{D}_{\text{out},j}|g\rangle \right|^2 \delta(E_f - E_g - \omega), \tag{4.9}$$

as outlined earlier in Sec. 3.1 of Chapter 3.

where

$$\tilde{O} = \frac{1}{-\hat{H} + i\Gamma}, \tag{4.10}$$

where $\hat{H}$ represents the *valence-band Hamiltonian*, and $\Gamma$ is the inverse of the core-hole lifetime. The factor $\mathcal{M}_\epsilon$ denotes the polarization-dependent atomic form factor, which incorporates the effects of both incoming and outgoing photon polarizations. The operators $\tilde{D}_{\text{in},j}$ and $\tilde{D}_{\text{out},j}$ correspond to the residual dipole operators after absorbing contributions into $\mathcal{M}_\epsilon$, with their explicit form depending on the particular scattering channel considered (see Sec. 3.1 of Chapter 3).

As discussed in Sec. 3.1.1 of Chapter 3, we adopt the ultra-short core-hole lifetime (UCL) approximation, which introduces the broadening factor $\Gamma$. Within this framework, a perturbative expansion in $J/\Gamma$ yields two distinct contributions to the RIXS intensity: the non-spin-conserving (NSC, $\Delta S = 1$) channel and the spin-conserving (SC, $\Delta S = 0$) channel (see Appendix A.2). Throughout this work we set $\hbar = 1$. The total RIXS intensity can then be written as $I_{\text{RIXS}} \propto \sum_l S_l^{\text{NSC}}(\mathbf{q},\omega) + \sum_l S_l^{\text{SC}}(\mathbf{q},\omega)$, where $\mathbf{q} = \mathbf{k}_{\text{out}} - \mathbf{k}_{\text{in}}$ is the momentum transfer to the lattice. The proportionality constant depends on polarization-dependent matrix elements $\mathcal{M}_\epsilon$ (see Ref. [7]).

In Appendix A.2, we provide explicit derivations of the UCL expansion for both channels. Below, we summarize the relevant response functions that we use in our analysis.

—

## Non-spin-conserving channel

The RIXS intensity in the NSC channel can be written as a series expansion in powers of $1/\Gamma$, with the $l^{\text{th}}$ order contribution given by

$$S_l^{\text{NSC}}(\mathbf{q},\omega) = \frac{1}{\Gamma^{2l+2}} \sum_f \left| \langle f | \frac{1}{\sqrt{N}} \sum_i e^{i\mathbf{q}\cdot\mathbf{R}_i} O_{i,l}^{\text{NSC}} | g \rangle \right|^2 \times \delta\left(E_f - E_g - \omega\right),$$

where $N$ is the total number of lattice sites. From Eq. A.43 in Appendix A.2, the operators are explicitly:

- $O_{i,0}^{\text{NSC}} = S_i^x$ for $l = 0$,
- $O_{i,1}^{\text{NSC}} = \sum_j J_{i,j} S_i^x \, \mathbf{S}_i \cdot \mathbf{S}_j$ for $l = 1$, where $i$ is the site where the core-hole is created,
- $O_{i,2}^{\text{NSC}} = \sum_{j,k} J_{i,j} J_{i,k} S_i^x (\mathbf{S}_i \cdot \mathbf{S}_j)(\mathbf{S}_i \cdot \mathbf{S}_k)$ for $l = 2$.

Later in this work, we provide pictorial representations of the bond summations appearing in $O_{i,1}^{\text{NSC}}$ and $O_{i,2}^{\text{NSC}}$.

—

## Spin-conserving channel

Similarly, the $l^{\text{th}}$ order contribution in the SC channel is given by

$$S_l^{\text{SC}}(\mathbf{q},\omega) = \frac{1}{\Gamma^{2l+2}} \sum_f \left| \langle f | \frac{1}{\sqrt{N}} \sum_i e^{i\mathbf{q}\cdot\mathbf{R}_i} O_{i,l}^{\text{SC}} | g \rangle \right|^2 \times \delta\left(E_f - E_g - \omega\right),$$

with operators (see Eq. A.44 in Appendix A.2):

- $O_{i,0}^{\text{SC}} = n_i$,
- $O_{i,1}^{\text{SC}} = \sum_j J_{i,j} \, \mathbf{S}_i \cdot \mathbf{S}_j$,
- $O_{i,2}^{\text{SC}} = \sum_{j,k} J_{i,j} J_{i,k} (\mathbf{S}_i \cdot \mathbf{S}_j)(\mathbf{S}_i \cdot \mathbf{S}_k)$.

It should be noted that the zeroth-order term ($l = 0$) does not generate magnetic excitations and contributes only to the elastic part of the RIXS cross-section.

—

In this treatment, our focus is exclusively on the many-body contributions to the RIXS cross-section. Although atomic form factors also influence experimental spectra, our primary objective is to isolate and analyze the many-body excitation structure revealed by RIXS.

## 4.4 Results and Discussions

As mentioned above we study the spin Hamiltonian defined in Eq. 4.1 within the framework of linear spin wave theory (LSWT). In the previous section we analyzed the RIXS intensity under the UCL approximation of the KH formalism, where we showed that the spectra can be expressed in terms of correlation functions in both spin-conserving (SC) and non-spin-conserving (NSC) channels. Throughout this work, we restrict ourselves to terms up to second order in the UCL expansion.

Our analysis is performed in the regime $|J_2| < J_1$. Here, a positive (negative) $J_2$ tends to destabilize (stabilize) the $J_2 = 0$ antiferromagnetic (AFM) ground state.

For clarity, Fig. 4.2(a) shows the Brillouin zone (BZ) and the momentum path considered in this study. Unless otherwise stated, we present our results along the standard high-symmetry path $\Gamma(0,0) \to X(\pi,0) \to M(\pi,\pi) \to \Gamma(0,0)$.

Since higher-order corrections in the NSC channel are relatively less explored, we begin our discussion with this channel. Afterwards, we turn to the SC channel and extend the analysis to include long-range contributions to the correlation functions.

### 4.4.1 Non spin conserving channel

In this section, we present results till the second-order correction in the UCL approximations discussed in Appendix A.2. One defining feature of the NSC channel is the presence of an *odd* number of spin flips. This arises due to the additional spin-flip induced by the strong spin–orbit coupling

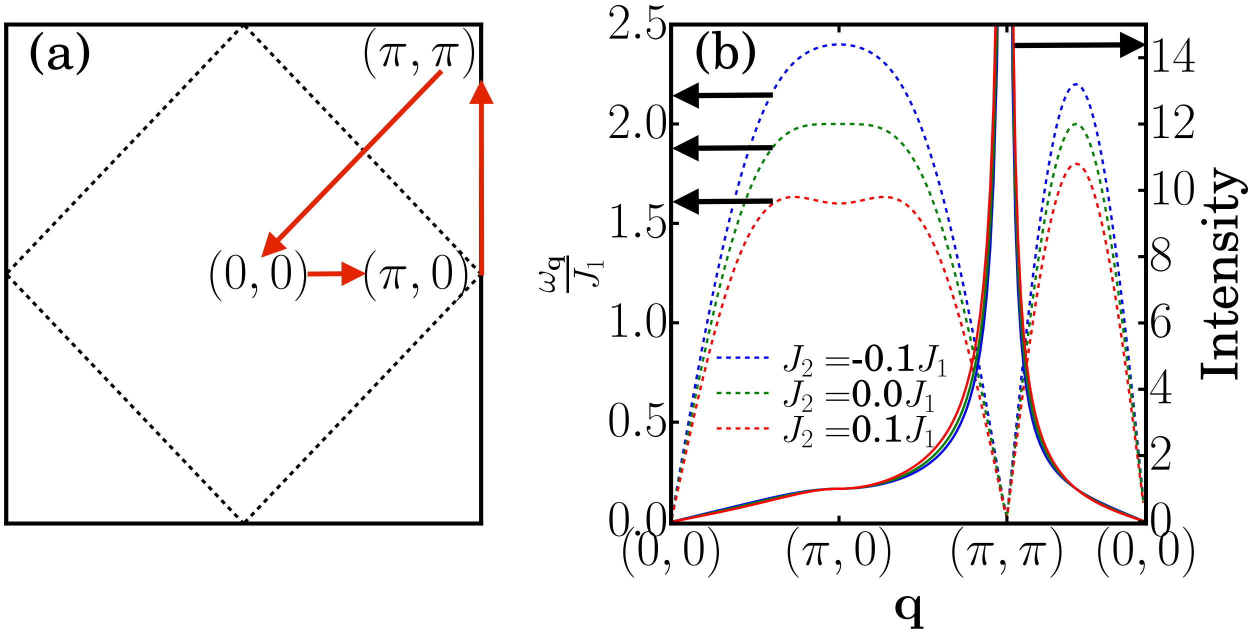

Figure 4.2: Panel (a) displays the magnetic Brillouin zone boundary (dashed lines). Panel (b) presents the magnon dispersion (dashed line) together with the momentum dependence of the one-magnon RIXS intensity (solid lines) for the two-dimensional extended Heisenberg model. The momentum path follows the arrows indicated in panel (a) [125]

of the intermediate core-hole orbital (see Sec.2.5.1 in Chap.3). For this reason, the NSC channel is typically absent at the $K$-edge.

### Zeroth order

At zeroth order in the UCL expansion, the NSC channel produces a single spin flip through the core-hole orbital. The corresponding scattering operator is given by

$$O^{\mathrm{NSC}}_{\mathbf{q},0} = \sum_i e^{i\mathbf{q}\cdot\mathbf{r}_i} S^x_i. \tag{4.11}$$

Where we have chosen the spin-flip direction along the $x$-axis within the lattice plane. This choice is necessary because the bipartite AFM ground state fixes the quantization axis (under LSWT). If a rotationally invariant ground state were possible, one could equivalently select any spin component [95]. In LSWT, this operator maps onto the AFM magnon basis as

$$O^{\mathrm{NSC}}_{\mathbf{q},0} \approx \sqrt{\frac{2SN}{2}}(u_{\mathbf{q}} - v_{\mathbf{q}})(\alpha_{\mathbf{q}} + \beta_{\mathbf{q}} + \alpha^{\dagger}_{-\mathbf{q}} + \beta^{\dagger}_{-\mathbf{q}}) \tag{4.12}$$

which shows that the operator can create a magnon from the vacuum, giving rise to single-magnon scattering.

The calculated zeroth-order spectrum is shown in Fig. 4.2(b) for the 2D AFM lattice with nearest-neighbor (NN) and next-nearest-neighbor (NNN) couplings. This spectrum is equivalent to the dynamical spin structure factor $S(\mathbf{q}, \omega)$, which is measurable in inelastic neutron scattering (INS) and supports the experimental findings reported in Ref. [26]. The magnon dispersion obtained within LSWT is plotted alongside the integrated intensity.

We observe that negative $J_2$ leads to a hardening of the magnon dispersion, most prominently at $(\pi, 0)$ and, to a lesser degree, at $(\pi/2, \pi/2)$. In contrast, positive $J_2$ softens the spectrum. These modifications are also reflected in the redistribution of spectral weight: for $J_2 < 0$, the intensity sharpens around $(\pi, \pi)$, whereas for $J_2 > 0$ the AFM order is weakened. The hardening observed for $J_2 < 0$ is consistent with earlier reports [7]. Furthermore, studies exploring how varying $J_2/J_1$ modifies RIXS features in 2D cuprates [129] align with our findings.

### Higher-order terms in the NSC channel

At higher orders, the NSC channel involves an odd number of spin flips through combinations of single- and double-spin-flip processes. This allows both one- and multi-magnon excitations to appear simultaneously. Schematics of these first and second-order contributions are shown in Fig. 4.3(a) and (b) respectively.

Since The first and second-order terms are governed by the three-magnon density of states (DOS), $A_{3M}(\omega) = \sum_{\omega', \omega''} A_{1M}(\omega - \omega' - \omega'')A_{1M}(\omega')A_{1M}(\omega'')$. Were $A_{1M}(\omega) = \sum_{\mathbf{k}} \delta(\omega - \epsilon_{\mathbf{k}})$ is the one-magnon DOS, and the dispersion $\epsilon_{\mathbf{k}}$ is given in Eq. 4.8.

Figures 4.3(c)–(e) display the three-magnon DOS for $J_2 = -0.1, 0.0,$ and $0.1$. For negative $J_2$, both the energy and spectral weight of the DOS shift to higher values (hardening), while positive

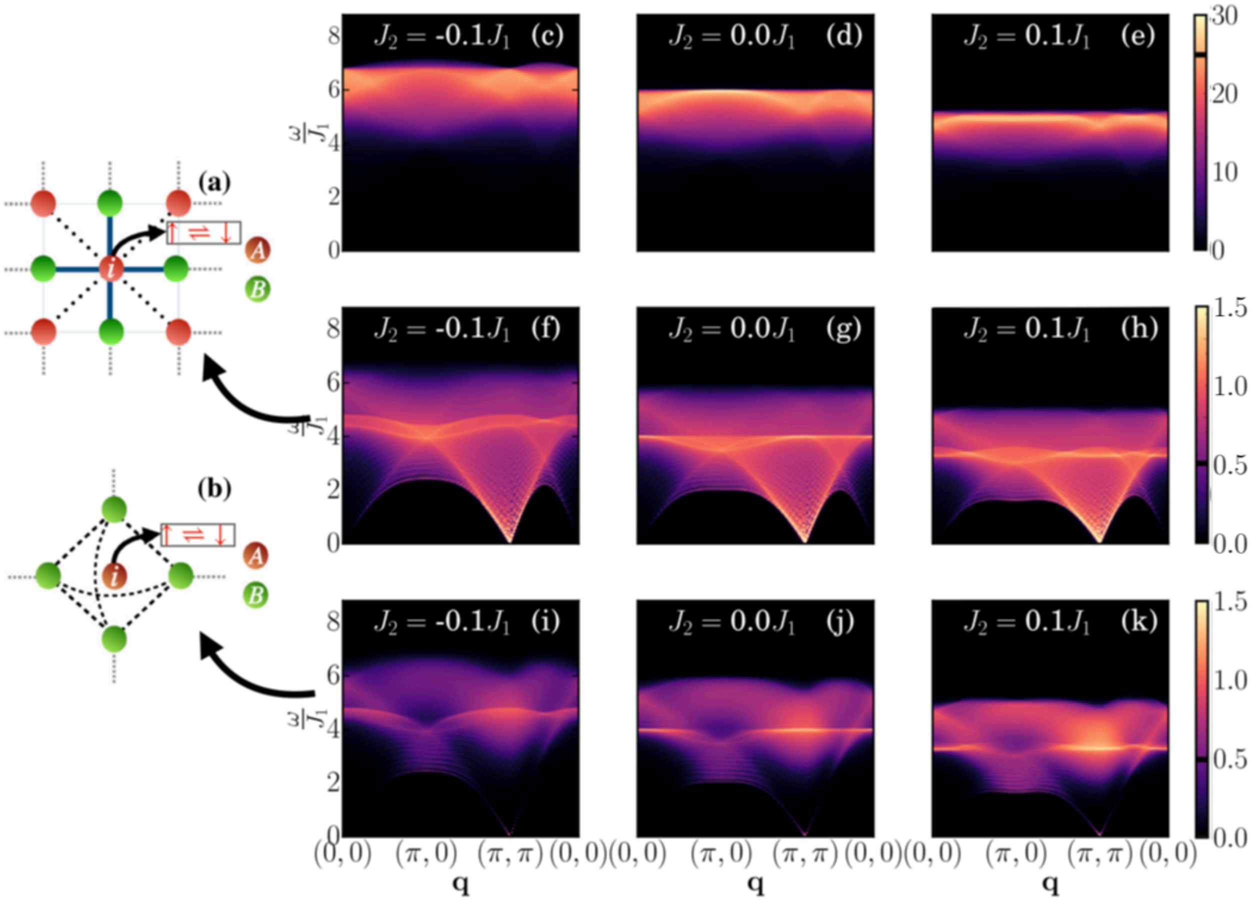

Figure 4.3: Resonant inelastic x-ray scattering (RIXS) spectra in the non-spin-conserving (NSC) channel [125].Panels (a) and (b) illustrate schematic representations of the first- and second-order contributions to the NSC RIXS spectra, corresponding to Eq. 4.13 and Eq. 4.20, respectively.The three-magnon density of states (DOS) for the extended Heisenberg antiferromagnet is shown in (c) $J_2 = -0.1J_1$, (d) $J_2 = 0$, and (e) $J_2 = 0.1J_1$. Panels (f)–(h) display the first-order RIXS spectra of UCL expansion for the same set of parameters, while (i)–(k) present the corresponding second-order spectra of UCL expansion. The color scale is constructed using a piecewise definition with threshold $U_0$ (indicated by the black marker on the color bar):for intensities below $U_0$ a linear scale is applied, while values above $U_0$ are shown on a logarithmic scale, $S(\mathbf{q},\omega) = U_0 + \mathrm{ln}_{10}[S(\mathbf{q},\omega)] - \mathrm{ln}_{10}(U_0)$. Here, $f(\mathbf{q},\omega)$ represents the three-magnon DOS in panels (c)–(e) and the RIXS intensity in panels (f)–(k).

$J_2$ causes softening. Notably, the three-magnon DOS shows only weak momentum dependence compared to single-magnon cases.

*First order*:— At first order in the UCL expansion, the correction appears with a prefactor of $O(J^2/\Gamma^4)$, where $J$ is the characteristic magnetic exchange scale ($J_1$) (see Appendix A.43). The scattering operator reads

$$O^{\mathrm{NSC}}_{\mathbf{q},1} = \sum_{i,j} e^{i\mathbf{q}\cdot\mathbf{ri}} J_{i,j} S^x_i (\mathbf{S}_i \cdot \mathbf{S}_j). \tag{4.13}$$

with $i, j$ denoting NN and NNN sites. This operator describes a single spin flip accompanied by double spin flips, schematically shown in Fig. 4.3(a).

Keeping only the linear terms in LSWT, the operator 4.13 can be mapped to bipartite bosons as

$$S^x_i \, \mathbf{S}_i \cdot \mathbf{S}_j \;\approx\; \sqrt{2S}\,\big(a^\dagger_i + a_i\big)\,\Big(-S^2 + S\big(a_i b_j + a^\dagger_i b^\dagger_j + a^\dagger_i a_i + b^\dagger_j b_j\big)\Big)\,. \tag{4.14}$$

We can express the operator as

$$O^{\mathrm{NSC}}_{\mathbf{q},1} = O^{\mathrm{NSC}}_{\mathbf{q},1'} + O^{\mathrm{NSC}}_{\mathbf{q},1''}. \tag{4.15}$$

The first contribution, $O^{\mathrm{NSC}}_{\mathbf{q},1'}$, contains only a single bosonic operator and can therefore be directly mapped onto a single-magnon excitation. In contrast, the second contribution, $O^{\mathrm{NSC}}_{\mathbf{q},1''}$, involves three bosonic operators and corresponds to a three-magnon excitation, explicitly given by

$$O^{\mathrm{NSC}}_{\mathbf{q},1''} = \frac{S^{3/2}}{\sqrt{2N}} \sum_{\mathbf{k},\mathbf{p}} [f_0(\mathbf{k},\mathbf{p},\mathbf{q}) \alpha^\dagger_{-\mathbf{p}} \beta^\dagger_{-\mathbf{k}} \alpha^\dagger_{\mathbf{k}+\mathbf{p}+\mathbf{q}} + f_1(\mathbf{k},\mathbf{p},\mathbf{q}) \beta^\dagger_{-\mathbf{p}} \beta^\dagger_{-\mathbf{k}} \alpha^\dagger_{\mathbf{k}+\mathbf{p}+\mathbf{q}}]$$

where

$$\begin{aligned} f_0(\mathbf{k},\mathbf{p},\mathbf{q}) &= -\{((J^{AB}_{\mathbf{p}+\mathbf{q}} + J^{NNN}_{\mathbf{k},\mathbf{p},\mathbf{q}})u_{\mathbf{p}} - ((J^{AB}_0 + J^{NNN}_{\mathbf{k},\mathbf{p},\mathbf{q}})v_{\mathbf{p}})u_{\mathbf{k}} v_{\mathbf{k}+\mathbf{p}+\mathbf{q}} \\ &\quad + ((J^{AB}_0 + J^{NNN}_{\mathbf{k},\mathbf{p},\mathbf{q}})u_{\mathbf{p}} - (J^{AB}_{\mathbf{p}+\mathbf{q}} + J^{NNN}_{\mathbf{k},\mathbf{p},\mathbf{q}})v_{\mathbf{p}})v_{\mathbf{k}} u_{\mathbf{k}+\mathbf{p}+\mathbf{q}}\} \\ &\quad + (J^{AB}_{\mathbf{k}+\mathbf{p}+\mathbf{q}} u_{\mathbf{p}} - J^{AB}_{\mathbf{k}} v_{\mathbf{p}}) v_{\mathbf{k}+\mathbf{p}+\mathbf{q}} v_{\mathbf{k}} + (J^{AB}_{\mathbf{k}} u_{\mathbf{p}} - J^{AB}_{\mathbf{k}+\mathbf{p}+\mathbf{q}} v_{\mathbf{p}}) u_{\mathbf{k}+\mathbf{p}+\mathbf{q}} u_{\mathbf{k}} \end{aligned} \tag{4.16}$$

$$\begin{aligned} f_1(\mathbf{k},\mathbf{p},\mathbf{q}) &= -\{((J^{AB}_0 + J^{NNN}_{\mathbf{k},\mathbf{p},\mathbf{q}})u_{\mathbf{p}} - (J^{AB}_{\mathbf{p}+\mathbf{q}} + J^{NNN}_{\mathbf{k},\mathbf{p},\mathbf{q}})v_{\mathbf{p}})u_{\mathbf{k}} v_{\mathbf{k}+\mathbf{p}+\mathbf{q}} \\ &\quad + ((J^{AB}_{\mathbf{p}+\mathbf{q}} + J^{NNN}_{\mathbf{k},\mathbf{p},\mathbf{q}})u_{\mathbf{p}} - (J^{AB}_0 + J^{NNN}_{\mathbf{k},\mathbf{p},\mathbf{q}})v_{\mathbf{p}})v_{\mathbf{k}} u_{\mathbf{k}+\mathbf{p}+\mathbf{q}}\} \\ &\quad + (J^{AB}_{\mathbf{k}} u_{\mathbf{p}} - J^{AB}_{\mathbf{k}+\mathbf{p}+\mathbf{q}} v_{\mathbf{p}}) v_{\mathbf{k}+\mathbf{p}+\mathbf{q}} v_{\mathbf{k}} + (J^{AB}_{\mathbf{k}+\mathbf{p}+\mathbf{q}} u_{\mathbf{p}} - J^{AB}_{\mathbf{k}} v_{\mathbf{p}}) u_{\mathbf{k}+\mathbf{p}+\mathbf{q}} u_{\mathbf{k}} \end{aligned} \tag{4.17}$$

and $J^{NNN}_{\mathbf{k},\mathbf{p},\mathbf{q}} = J^{AA}_{\mathbf{k}+\mathbf{p}+\mathbf{q}} + J^{AA}_{\mathbf{k}} - J^{AA}_0 - J^{AA}_{\mathbf{p}+\mathbf{q}}$

The resulting spectra for $J_2 = -0.1, 0.0$, and $0.1$ are shown in Figs. 4.3(f)–(h). The response contains both weak one-magnon signatures and more prominent three-magnon features. For $J_2 = 0$, the three-magnon spectrum exhibits three characteristic bands: [1] a dispersing band up to $4J_1$ with a width of $\sim 4J_1$, [2] a nearly flat band around $4J_1$, [3] a higher-energy dispersive band reaching $\sim 5J_1$.

When $J_2$ is finite, these features shift: for $J_2 < 0$, they harden, while for $J_2 > 0$, they soften, consistent with the trends observed in the one-magnon sector shown in Fig. 4.3(f) and (h).

*Second Order*:— The second-order term contributes at $O(J^4/\Gamma^6)$ and involves one spin flip combined with the product of two double spin flips: .

$$O^{\mathrm{NSC}}_{\mathbf{q},2} = \sum_{\langle i,j,k \rangle} e^{i\mathbf{q}\cdot\mathbf{r_i}} J_{ij} J_{ik} S^x_i (\mathbf{S}_i \cdot \mathbf{S}_j)(\mathbf{S}_i \cdot \mathbf{S}_k). \tag{4.18}$$

Using spin algebra [55, 95], the double-spin terms can be reduced to

$$J_{i,j} J_{i,k} (\mathbf{S}_i \cdot \mathbf{S}_j)(\mathbf{S}_i \cdot \mathbf{S}_k) \approx -\frac{1}{2} J^2_{i,j} (\mathbf{S}_i \cdot \mathbf{S}_j) + \frac{1}{4} J_{i,j} J_{i,k} (\mathbf{S}_j \cdot \mathbf{S}_k) \tag{4.19}$$

The four-spin term can be effectively decomposed into two contributions: one involving nearest-neighbor (NN) interactions and the other describing longer-range processes. The first contribution involves spin operators with indices $i$ and $j$ running over NN sites. Since this part has the same mathematical structure as the first-order operator (differing only by a prefactor), it does not introduce any new physical features. For this reason, our analysis focuses on the second contribution of Eq. 4.19.

This second term describes long-range double spin-flip processes, where the indices $j$ and $k$ correspond to NN sites of the core-hole site $i$. A schematic representation of these processes is shown in Fig. 4.3(b).

The new correlation arising at this order is therefore given by

$$O^{\mathrm{NSC}}_{\mathbf{q},2'} = \sum_{i,j,k} e^{i\mathbf{q}\cdot\mathbf{r}_i} J_{i,j} J_{i,k} S^x_i (\mathbf{S_j} \cdot \mathbf{S}_k) \tag{4.20}$$

As discussed for the first order, the HP transformation for this also yields two terms

$$S_i^x\, \mathbf{S}_i \cdot \mathbf{S}_j \;\approx\; \sqrt{2S}\,\left(a_i^\dagger + a_i\right)\Big(-S^2 + S\big(a_i b_j + a_i^\dagger b_j^\dagger + a_i^\dagger a_i + b_j^\dagger b_j\big)\Big) \tag{4.21}$$

Again, the operator can be rewritten as; $O^{\mathrm{NSC}}_{\mathbf{q},2'} = O^{\mathrm{NSC},1}_{\mathbf{q},2'} + O^{\mathrm{NSC},2}_{\mathbf{q},2'}$. The first term, $O^{\mathrm{NSC},1}_{\mathbf{q},2'}$, turns out to contribute to only a single spin-flip excitations akin to zeroth order. The second term has a distinct form and can contribute to multi-particle excitations. After the Bogoliubov transformation, the second term is given by

$$\begin{aligned} O^{\mathrm{NSC},2}_{\mathbf{q},2'} \approx & \frac{S^{3/2}}{\sqrt{2N}} \sum_{\mathbf{k},\mathbf{p}} f(\mathbf{k},\mathbf{p},\mathbf{q})[(v_{\mathbf{p}} u_{\mathbf{k}+\mathbf{q}-\mathbf{p}} v_{\mathbf{k}} - u_{\mathbf{p}} v_{\mathbf{k}+\mathbf{q}-\mathbf{p}} u_{\mathbf{k}})\alpha^\dagger_{\mathbf{p}} \alpha^\dagger_{\mathbf{k}+\mathbf{q}-\mathbf{p}} \beta^\dagger_{-\mathbf{k}} \\ & + (v_{\mathbf{p}} v_{\mathbf{k}+\mathbf{q}-\mathbf{p}} u_{\mathbf{k}} - u_{\mathbf{p}} u_{\mathbf{k}+\mathbf{q}-\mathbf{p}} v_{\mathbf{k}})\beta^\dagger_{\mathbf{p}} \alpha^\dagger_{\mathbf{k}+\mathbf{q}-\mathbf{p}} \beta^\dagger_{-\mathbf{k}}] \end{aligned} \tag{4.22}$$

where $f(\mathbf{k},\mathbf{p},\mathbf{q}) = (J_1)^2[-6\{\cos(q_x - p_x) + \cos(q_y - p_y)\} + 2\{\cos(2k_x + q_x - p_x)$ $+ \cos(2k_y + q_y - p_y)\} + 4\{\cos(k_y)\cos(k_x + q_x - p_x) + \cos(k_x)\cos(k_y + q_y - p_y)\}]$

We have thus mapped this higher-order term to three-magnon excitations in the antiferromagnetic lattice. While the structure is similar to the first-order contribution, it takes a distinct form.

In Fig. 4.3, panels (i)–(k) display the corresponding three-magnon response function obtained from Eq. 4.20. The three-magnon spectral weight exhibits a pronounced peak near $\omega = 4J_1$ at $\mathbf{q} = 0$ for $J_2 = 0$, and this feature remains finite across the entire Brillouin zone. A clear signature of the single-magnon excitation is visible as a sharp dispersing band in panel (i), whose bandwidth agrees well with the single-magnon spectrum shown in Fig. 4.2(b). However, its overall intensity is strongly suppressed, and at $\mathbf{q} = 0$ this contribution vanishes due to the absence of one-magnon density of states. Similar spectral features are observed in panels (j) and (k) of Fig. 4.3.

The broad, continuum-like feature spanning the Brillouin zone in panels (i)–(k) originates from the operator $O^2_{\mathbf{q}}$, which does not commute with the unperturbed Hamiltonian $H$ for any $\mathbf{q}$.

As in the first-order case, the inclusion of finite $J_2$ modifies the spectrum. Panels (i) and (k) reveal that positive $J_2$ ($J_2 > 0$) leads to a softening of the modes, while negative $J_2$ ($J_2 < 0$) results in hardening. Moreover, the spectral weight is enhanced for $J_2 > 0$ and suppressed for $J_2 < 0$. The latter effect can be understood as the strengthening of the underlying antiferromagnetic order when $J_2 < 0$, which makes AFM spin-flip excitations more dominant and reduces the three-magnon contribution.

We conclude our linear spin-wave theory (LSWT) analysis of the non-spin-conserving (NSC) channel by summarizing, in Fig. 4.4(a), the combined contributions to the RIXS intensity up to second order. For this calculation, we have set $\Gamma/J_1 = 5$ following Ref. [55]. The results demonstrate that higher-order contributions are significant compared to the single-magnon signal, and must therefore be included to fully capture the NSC channel response.

**Non-spin-conserving channel: Exact Diagonalization**

To benchmark the LSWT results, we performed small-cluster exact diagonalization (ED) calculations on the spin Hamiltonian in Eq. 4.1. Figures 4.4(b) and (c) present the three-magnon susceptibility on a $4 \times 4$ lattice at first and second order, respectively. In panel (b), a weak peak is

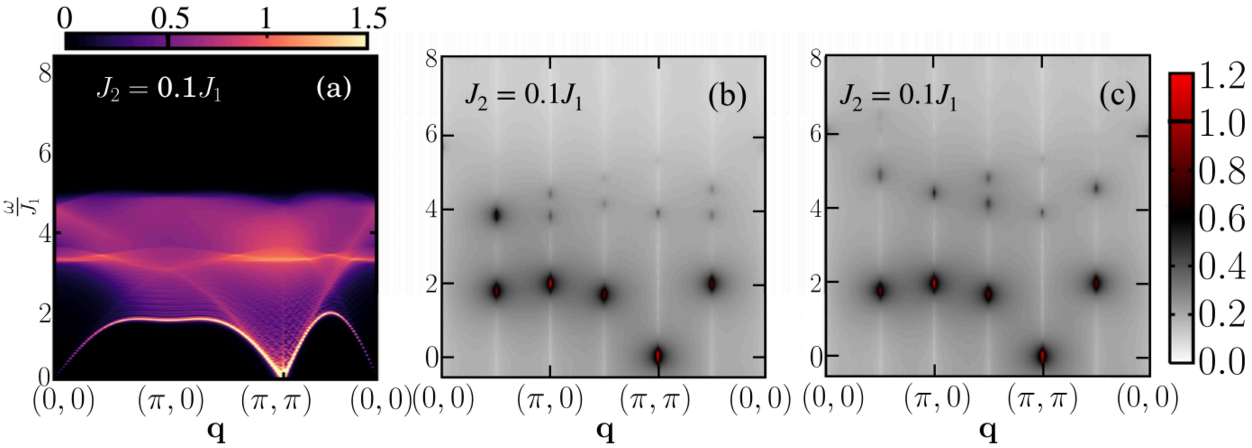

Figure 4.4: Comparison between linear spin-wave theory (LSWT) and exact diagonalization (ED) on a $4 \times 4$ cluster for the non-spin-conserving (NSC) channel [125]. Panel (a) shows the total NSC contribution obtained from LSWT, including terms up to second order in the UCL expansion, with $\Gamma = 5J_1$. Panels (b) and (c) display the ED results for the first- and second-order contributions, respectively, at $J_2 = 0.1J_1$.Vertical markers in (b) and (c) indicate the allowed momentum transfer values. The color maps are generated using the same piecewise scaling scheme as in Fig. 4.3, with the threshold $U_0$ marked in black on the color bars.

visible at $\mathbf{q} = (0,0)$ that disperses across the Brillouin zone, consistent with the LSWT predictions. Furthermore, a clear separation is observed between low-energy excitations, lying in the range $0 \leq \omega \lesssim 2J_1$, and higher-energy excitations centered above $4J_1$.

In panel (c), the low-energy branch is slightly pushed below $2J_1$, while remaining distinct from the higher-energy continuum. By analyzing the contributions of basis states to different peaks across the Brillouin zone, we find that excitations below $\omega/J_1 = 2$ are dominated by single-spin-flip basis states. This strongly supports the conclusion that the low-energy LSWT spectra originate from single-magnon excitations. In contrast, the higher-energy features are composed of multi-spin-flip states, consistent with a three-magnon origin.

Due to the severe finite-size limitations of ED, the absolute excitation energies are somewhat overestimated. Nevertheless, these results provide a valuable qualitative check on the NSC channel. The key outcome is that the NSC channel generates robust high-energy excitations with finite spectral weight distributed throughout the Brillouin zone.

### 4.4.2 Spin-conserving channel

In the spin-conserving (SC) channel, higher-order corrections involve an even number of spin flips, which can generate magnetic excitations. Here, we analyze the dynamical correlation functions associated with two-magnon processes. For completeness, we also evaluate the correlation function with next-nearest-neighbor (NNN) interactions, which emphasizes why the non-spin-conserving (NSC) channel is essential for capturing the distinctive features observed in the RIXS spectra of two-dimensional antiferromagnets.

At leading order, this channel naturally maps onto two-magnon excitations. The corresponding density of states (DOS), $A_{2M}(\omega)$, can be written as the convolution of two one-magnon DOS,

$$A_{2M}(\omega) = \sum_{\omega'} A_{1M}(\omega - \omega')A_{1M}(\omega'), \tag{4.23}$$

where

$$A_{1M}(\omega) = \sum_{\mathbf{k}} \delta(\omega - \epsilon_{\mathbf{k}}), \tag{4.24}$$

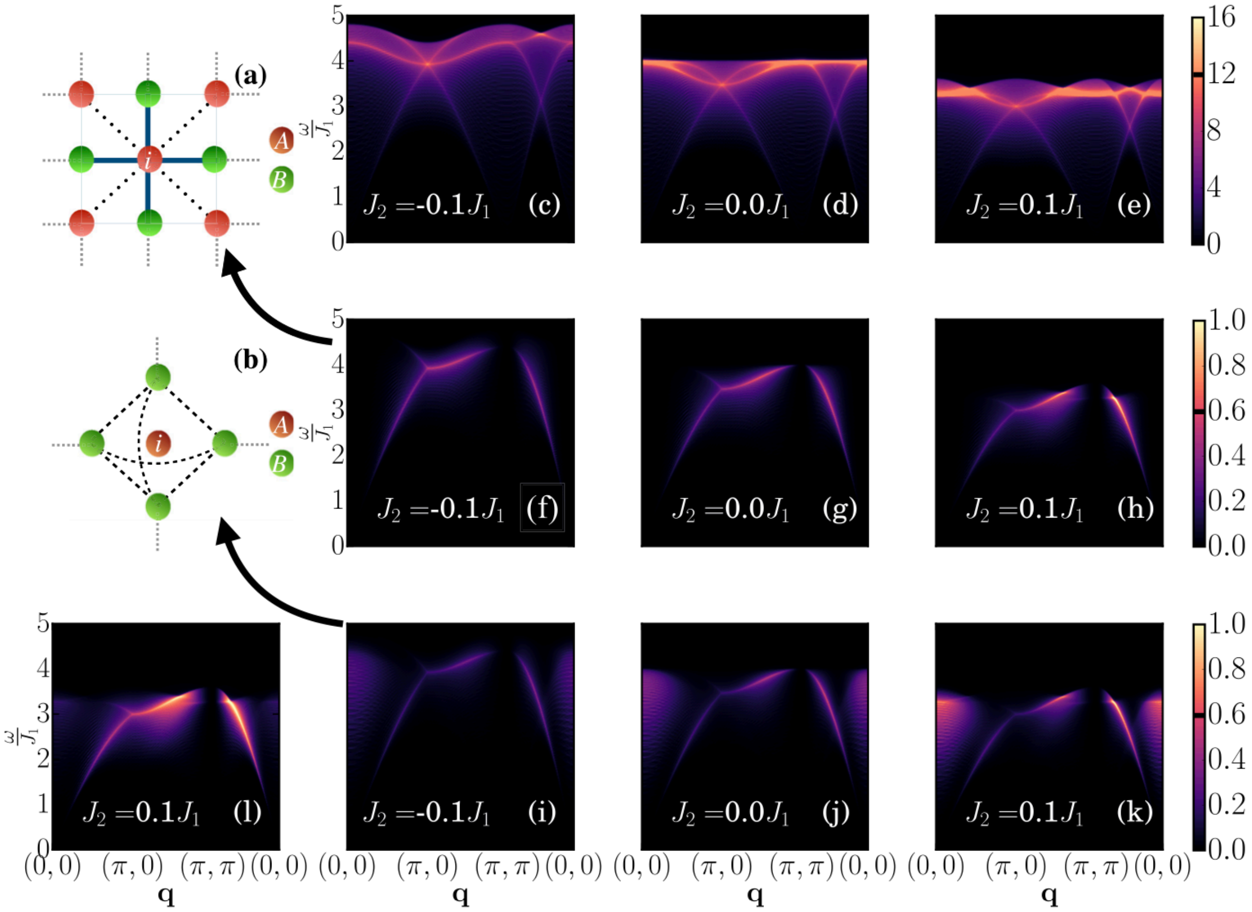

Figure 4.5: Resonant inelastic x-ray scattering (RIXS) spectra in the spin-conserving (SC) channel [125].Panels (a) and (b) show schematic diagrams of the first- and second-order contributions to the SC RIXS spectra, corresponding to Eq. 4.25 and Eq. 4.28, respectively.The two-magnon density of states (DOS) for the extended Heisenberg antiferromagnet is presented in (c) $J_2 = -0.1J_1$, (d) $J_2 = 0$, and (e) $J_2 = 0.1J_1$. The first-order spectra obtained from the UCL expansion are displayed in panels (f)–(h), while the corresponding second-order spectra are shown in panels (i)–(k). Panel (l) presents the combined SC intensity, including contributions from both first- and second-order terms in the ultrashort core-hole lifetime (UCL) expansion, evaluated at $\Gamma = 5J_1$.The colormaps follow the same piecewise scaling scheme described in Fig. 4.3, with the threshold value $U_0$ indicated in black on the color bars.

as defined in Eq. 4.8. The calculated two-magnon DOS for $J_2 = -0.1, 0$, and $0.1$ are shown in Fig. 4.5(c)–(e).

*First Order*:– At first order in the UCL expansion, of order $O(J^2/\Gamma^4)$, the dominant contribution arises from double spin flips. The associated scattering operator is given by

$$O^{\mathrm{SC}}_{\mathbf{q},1} = \sum_{i,j} e^{i\mathbf{q}\cdot\mathbf{r}_i} J_{i,j}\,\mathbf{S}_i \cdot \mathbf{S}_j, \tag{4.25}$$

where the summation runs over both nearest-neighbor (NN) and NNN bonds, consistent with the Hamiltonian $H$. These bonds are illustrated in Fig. 4.5(a).

Applying the Holstein-Primakoff (HP) transformation, Eq. 4.25 becomes

$$O^{\mathrm{SC}}_{\mathbf{q},1} \approx S \sum_{\mathbf{k}\in BZ} \Big[ f_0(\mathbf{k},\mathbf{q})\big(a^\dagger_{\mathbf{k}-\mathbf{q}/2} a_{\mathbf{k}+\mathbf{q}/2} + b^\dagger_{\mathbf{k}-\mathbf{q}/2} b_{\mathbf{k}+\mathbf{q}/2}\big) + f_1(\mathbf{k},\mathbf{q})\big(a_{\mathbf{k}-\mathbf{q}/2} b_{-\mathbf{k}-\mathbf{q}/2} + a^\dagger_{\mathbf{k}+\mathbf{q}/2} b^\dagger_{-\mathbf{k}-\mathbf{q}/2}\big)\Big], \tag{4.26}$$

which after the Bogoliubov transformation takes the form

$$\begin{aligned} O^{\mathrm{SC}}_{\mathbf{q},1} \approx S \sum_{\mathbf{k}\in BZ} \Big[ &- f_0(\mathbf{k},\mathbf{q})\big(u_{\mathbf{k}+\mathbf{q}/2} v_{\mathbf{k}-\mathbf{q}/2} + u_{\mathbf{k}-\mathbf{q}/2} v_{\mathbf{k}+\mathbf{q}/2}\big) \\ &+ f_1(\mathbf{k},\mathbf{q})\big(u_{\mathbf{k}+\mathbf{q}/2} u_{\mathbf{k}-\mathbf{q}/2} + v_{\mathbf{k}+\mathbf{q}/2} v_{\mathbf{k}-\mathbf{q}/2}\big)\Big]\big(\alpha_{\mathbf{k}+\mathbf{q}/2}\beta_{-\mathbf{k}+\mathbf{q}/2} + \alpha^\dagger_{\mathbf{k}-\mathbf{q}/2}\beta^\dagger_{-\mathbf{k}-\mathbf{q}/2}\big), \end{aligned} \tag{4.27}$$

where

$$\begin{aligned} f_0(\mathbf{k},\mathbf{q}) &= J^{AA}_{\mathbf{k}+\mathbf{q}/2} + J^{AA}_{\mathbf{k}-\mathbf{q}/2} + J^{AA}_0 + J^{AA}_{\mathbf{q}} + J^{AB}_0 + J^{AB}_{\mathbf{q}}, \\ f_1(\mathbf{k},\mathbf{q}) &= J^{AB}_{\mathbf{k}+\mathbf{q}/2} + J^{AB}_{\mathbf{k}-\mathbf{q}/2} \end{aligned}$$

The resulting RIXS intensity is presented in Fig. 4.5(f)–(h). Several features stand out. Notably, the spectral weight vanishes at $\mathbf{q} = (0,0)$ and $\mathbf{q} = (\pi,\pi)$, in agreement with experimental observations at the Cu $K$-edge in La$_2$CuO$_4$ [73], as anticipated from Eq. 4.26. At $\mathbf{q} = (0,0)$, the operator commutes with the Hamiltonian $H$, i.e. $[H, O_{\mathbf{q}=(0,0)}] = 0$, implying that the they have the same eigenbasis, which forces $\langle f|O_{\mathbf{q}=(0,0)}|g\rangle = 0$. Similarly, in an antiferromagnetic ground state the intensity vanishes at $\mathbf{q} = (\pi,\pi)$ because it is the reciprocal lattice vector associated with Néel order. In this case, $O_{\mathbf{q}=(\pi,\pi)}$ is antisymmetric under interchange of the two sublattices ($A \leftrightarrow B$), while the ground state is symmetric, ensuring that $\langle f|O_{\mathbf{q}=(\pi,\pi)}|g\rangle = \sum_{i\in A,j} \mathbf{S}_i\cdot\mathbf{S}_j - \sum_{i\in B,j} \mathbf{S}_i\cdot\mathbf{S}_j = 0$.

We also find that negative $J_2$ shifts the two-magnon DOS and spectral weight to higher energies (hardening), while positive $J_2$ produces the opposite effect (softening).

*Second Order*:– At second order in the UCL expansion, of order $O(J^4/\Gamma^6)$, the scattering operator is given by

$$O^{\mathrm{SC}}_{\mathbf{q},2} = \sum_{i,j,k} e^{i\mathbf{q}\cdot\mathbf{r}_i} J_{i,j} J_{i,k} (\mathbf{S}_i \cdot \mathbf{S}_j)(\mathbf{S}_i \cdot \mathbf{S}_k). \tag{4.28}$$

This expression can be simplified in analogy to the NSC channel (see Eq. 4.19). Two distinct contributions appear: a two-magnon term with a different prefactor, and a new term of the form

$$\frac{1}{4} J_{i,j} J_{i,k} (\mathbf{S}_j \cdot \mathbf{S}_k). \tag{4.29}$$

The latter arises from bonds connecting sites $j$ and $k$, as illustrated in Fig. 4.5(b).

Following the same procedure as before, this yields

$$O^{\mathrm{SC}}_{\mathbf{q},2'} \approx \sqrt{2S} \sum_{\mathbf{k}} f(\mathbf{k},\mathbf{q}) \big( u_{\mathbf{k}} v_{\mathbf{k}+\mathbf{q}} + u_{\mathbf{k}+\mathbf{q}} v_{\mathbf{k}} \big) \alpha^{\dagger}_{\mathbf{k}} \beta^{\dagger}_{-\mathbf{k}-\mathbf{q}}, \tag{4.30}$$

with the prefactor

$$\begin{aligned} f(\mathbf{k},\mathbf{q}) = (J_1)^2 \Big[ &- 6\{\cos(q_x) + \cos(q_y)\} + 2\{\cos(2k_x + q_x) + \cos(2k_y + q_y)\} \\ &+ 4\{\cos(k_y)\cos(k_x + q_x) + \cos(k_x)\cos(k_y + q_y)\} \Big]. \end{aligned} \tag{4.31}$$

The corresponding spectra are displayed in Fig. 4.5(i)–(k). For $J_2 = 0$, shown in panel (j), dispersive features are visible within the energy window allowed by the two-magnon DOS. Unlike the first-order contribution, however, we now observe finite spectral weight near $\mathbf{q} = (0,0)$, spread over $3J_1 \lesssim \omega \lesssim 4J_1$. This weight is mostly confined between $\mathbf{q} = (0,0)$ and $\mathbf{q} \approx (\pi/2, 0)$. In addition, a second feature reminiscent of the first-order two-magnon contribution appears at intermediate momentum transfer. Thus, the primary correction at second order is the emergence of finite intensity around $\mathbf{q} = (0,0)$.

Importantly, while the two-magnon part of the operator commutes with $H$ at $\mathbf{q} = (0,0)$ for both first and second orders, the additional term $\frac{1}{4} J_{i,j} J_{i,k} (\mathbf{S}_j \cdot \mathbf{S}_k)$ does not commute with $H$, and hence produces finite spectral weight at second order.

These features remain present for $J_2 = \pm 0.1 J_1$, with $J_2 > 0$ ($J_2 < 0$) leading to their enhancement (suppression), consistent with expectations.

We conclude this section by presenting in Fig. 4.5(l) the combined first- and second-order contributions to the RIXS intensity in the SC channel. Unlike the NSC channel, the zeroth-order term in the SC channel does not contribute to spin excitations. For comparison with the NSC case, we have set $J_1/\Gamma = 5$. As shown, the second-order feature at $\mathbf{q} = (0, 0)$ remains highly suppressed in the full SC response.

## 4.5 Conclusion

In this work, we have carried out a comprehensive study of the RIXS cross-section for two-dimensional antiferromagnets (AFMs) in both the NSC and SC channels, including second-order corrections in the UCL expansion of the Kramers-Heisenberg formalism relevant for the Cu $L$-edge of cuprates. These corrections were analyzed using linear spin-wave theory (LSWT). Our analysis reveals the presence of three-magnon excitations in the NSC channel [125]. We find that these excitations carry finite weight at both first- and second-order levels. Importantly, the three-magnon spectrum exhibits a distinct high-energy feature characterized by a quasi-flat band that extends across the Brillouin zone, in clear contrast to the two-magnon excitations reported previously. Furthermore, the NSC results obtained from LSWT show qualitative agreement with exact diagonalization calculations on small clusters.

Experimentally, the Cu $L$-edge RIXS response in 2D cuprates is dominated by the NSC channel. We therefore compare our findings with the Cu $L_3$-edge RIXS data of $La_2CuO_4$ reported in Ref. [139]. The data show a broad excitation feature around $\omega \approx 350$ meV (Fig. 4.1) that disperses weakly across the Brillouin zone and extends up to $\mathbf{q} = (0, 0)$, in addition to the established one- and two-magnon features. Using $J_1 \approx 150$ meV, our calculations reproduce the qualitative spread of the RIXS spectra, allowing us to interpret this high-energy feature as a three-magnon excitation [125]. However, within LSWT, the predicted energy of the three-magnon lies higher than that observed in experiment. This discrepancy is not unexpected, as three-magnon excitations are expected to soften once magnon–magnon interactions are included. Indeed, Ref. [134] has reported significant softening of three-magnon excitations in the dynamical spin structure factor, though extending such an analysis to the RIXS cross-section lies beyond the present scope.

We have also analyzed the SC channel, incorporating extended correlation functions with longer-range interactions relevant for the Cu $L$-edge. Our results indicate that such interactions do not qualitatively modify the spectral features of the first- and second-order corrections. Instead, it is the higher-order terms in the NSC channel that play a central role in capturing the additional magnetic excitations observed in high-resolution $L$-edge RIXS experiments.

Overall, our results provide new insight into the origin of multi-magnon excitations in the RIXS spectra of 2D AFMs [139], and their possible role in the pairing mechanism of high-$T_c$ superconductors. While our primary focus here has been on direct RIXS at the Cu $L$-edge, we note that LSWT can also be applied to study indirect RIXS, with the SC channel corresponding to the latter case [55]. The demonstrated importance of higher-order corrections in the RIXS cross-section highlights new opportunities for probing higher-order magnetic excitations in quantum materials. In particular, the persistence of these multi-magnon features even at small momentum transfer provides a promising pathway for exploring quantum magnets in regimes where access to large momentum transfer is limited.

# Chapter 5

# Unveiling Field-Tuned Fractionalized and High energy Excitations in Spin-Trimer Chains with RIXS

*High-energy spin excitations play a central role in correlated materials, but their microscopic origins are often obscured by material complexity. In this chapter, we show that the spin-$\frac{1}{2}$ trimer chain realized in* $\mathrm{Cu_3(P_2O_6OH)_2}$*, characterized by a periodic antiferromagnetic exchange pattern* $J_1$*-*$J_1$*-*$J_2$ *with* $J_1 < J_2$ *(Ref.[126]), provide a simple and ideal system to study these excitations using RIXS. By applying DMRG (see Sec. 3.3.3 in chapter 3), ED, and real-space renormalization group (RG) techniques, we demonstrate that trimerization modifies the conventional Heisenberg spinon continuum and leads to several distinct high-energy sharp RIXS features. These features originate from composite quasiparticle modes associated with local trimer excitations and strong inter-trimer interactions. Furthermore, we show that the RIXS spectra evolve under an applied magnetic field, revealing gapless* $S = 1$ *bosonic modes above a gapped* $1/3$ *magnetization plateau. The predicted energy scales are accessible with current RIXS experiments, positioning trimer chains as a model system for investigating universal high-energy quasiparticles in low-dimensional quantum magnets.*

## 5.1 Introduction

Low-dimensional quantum magnets are fertile ground for emergent quantum phases and fractionalized excitations. In one dimension (1D), where strong correlations and reduced dimensionality constrain dynamics, spin-1/2 chains and ladders have yielded deep insights into confinement-deconfinement phenomena [151, 152, 183], quantum criticality [186, 75, 119, 84, 140, 76], and spin fractionalization [154, 28, 157, 155, 29]. Beyond simple chains, systems with enlarged unit cells produce additional structure in the excitation spectrum, enabling novel quasiparticles and emergent transitions [47, 19, 32, 137]. These advances are driven by the synthesis of model 1D compounds [31, 88, 39] and by spectroscopies that access both local and nonlocal spin dynamics, including inelastic neutron scattering (INS) and resonant inelastic X-ray scattering (RIXS) [62, 83, 115, 9], as well as spin echo [174] and terahertz probes [52].

The spin-1/2 Heisenberg antiferromagnetic chain (HAC) is the paradigmatic integrable 1D model with gapless spinon excitations [20]. However, integrability is broken by exchange modulation and frustration, leading to reconstructed continua and new composite modes. A prominent example is $Na_2Cu_3Ge_4O_{12}$, a $J_1$-$J_1$-$J_2$ antiferromagnetic trimer chain with $J_1 > J_2$, small intra-trimer frustration $J_3$, and inter-trimer exchange $J_2$ [see Fig. 1.5(c) in Chapter 1]. Recent work has established the coexistence of gapless spinons with gapped composite excitations—doublons and quartons—arising from trimer excitations dressed by spinons [19, 137]. *While Ref. [137] is not formally part of this thesis, the author is an equal contributor; importantly, that study motivates and frames the results presented in this chapter.*

*Spin trimer with $J_1 > J_2$.* In Ref. [137], we performed a comprehensive theoretical study of RIXS in frustrated spin-1/2 trimer chains, focusing on $Na_2Cu_3Ge_4O_{12}$. Our goals were twofold: (i) to identify fractionalized magnetic excitations and other collective modes present in the material, and (ii) to determine how these excitations appear in RIXS—complementing earlier INS measurements [18, 19] that are less sensitive to certain low-energy processes. We employed the ultrashort core-hole lifetime (UCL) expansion (Sec. 3.1.1) to decompose the RIXS cross section into spin-conserving (SC) and non-spin-conserving (NSC) channels. The minimal spin model combines intra-trimer exchanges $J_1$ and $J_3$ (the latter a next-nearest-neighbor, frustrating coupling) with inter-trimer exchange $J_2$:

$$H = \sum_i \left( J_1\, \mathbf{S}_i^a \cdot \mathbf{S}_i^b + J_2\, \mathbf{S}_i^b \cdot \mathbf{S}_i^c + J_1\, \mathbf{S}_i^c \cdot \mathbf{S}_{i+1}^a + J_3\, \mathbf{S}_i^a \cdot \mathbf{S}_i^c \right),$$

where $i$ indexes the unit cells and $\{a, b, c\}$ label the three spins in each trimer (see Sec. 1.2.1,

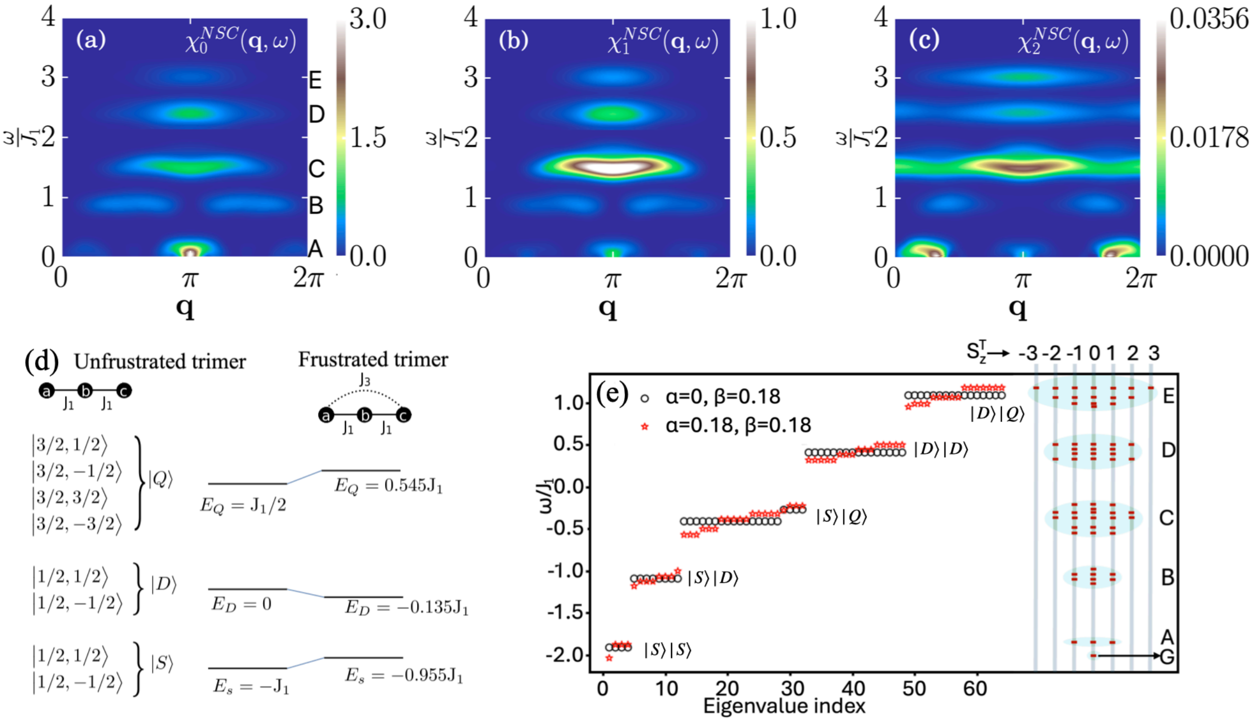

Figure 5.1: RIXS spectra in the non-spin-conserving (NSC) channel from the UCL expansion for $J_1 = 1.0$ and $J_2 = J_3 = 0.18J_1$ on a chain with $N = 24$ sites [137]. Panels (a), (b), and (c) show the zeroth-, first-, and second-order contributions, respectively. To enhance visibility above $\omega = 2.135J_1$, intensities are scaled by factors of 500, 100, and 100 in (a), (b), and (c). In (c), the low-energy window $\omega < 0.5J_1$ is additionally scaled by 10 to highlight fine structure. Panel (d) shows the level spectrum of a single trimer without (left) and with (right) frustration. The total spin $S^T$ and its $z$-component $S_z^T$ (identical in both cases) are indicated. Spinon $|S\rangle$, doublon $|D\rangle$, and quarton $|Q\rangle$ labels are marked. The middle and right columns list eigenvalues for the unfrustrated and frustrated trimers. Panel (e) (left) compares eigenvalues for two decoupled (black circles) and coupled (red stars) trimers; (right) the coupled spectrum is resolved by total $S_z^T$ (gray vertical guides). The antiferromagnetic ground state lies in $S_z^T = 0$. Features A-E correspond to excitations identified in (a), with energies measured relative to the ground state. The blue shading highlights spectral broadening upon coupling trimers.

Chapter 1).

We computed multi-spin dynamical correlation functions and RIXS spectra at zeroth, first, and second order in the UCL expansion using Lanczos diagonalization (Sec. 3.3.2, Chapter 3) and the Fock-space recursive Green's function (F-RGF) approach [135, 136] on a 24-site chain. The NSC spectra are shown in Fig. 5.1(a-c).

By comparing these spectra with exact diagonalization (ED) of one- and two-trimer clusters

[Fig. 5.1(d,e)] and with large-system calculations, we identified the dominant low-energy continuum in the NSC channel (feature A) as gapless spin-1/2 spinon. At intermediate energies we reproduced the previously reported propagating composite modes—**doublons** ($|D\rangle$, feature B) and **quartons** ($|Q\rangle$, feature C)—which carry the fingerprints of single-trimer excitations dressed by spinons [18, 19]. Importantly, we predicted two additional high-energy modes at $\omega \approx 2.4 J_1$ (feature D) and $\omega \approx 3.0 J_1$ (feature E), which originate from two-trimer excitations [Fig. 5.1(e)] and were not resolved in earlier INS experiments. We further analyzed momentum dependence and higher-order UCL contributions, established spin selection rules that differentiate SC and NSC channels, and showed that weak intra-trimer frustration $J_3$ does not qualitatively change these conclusions by comparison with $J_3 = 0$.

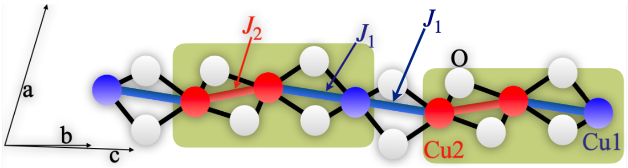

Figure 5.2: Schematic positions of Cu and O atoms in $Cu_3(P_2O_6OH)_2$ [126]. Blue, red, and white circles denote Cu1, Cu2, and O atoms bonded to Cu. Black bars mark Cu-O bonds; red and blue bars indicate the shortest and second-shortest Cu-Cu separations, associated with exchange couplings $J_1$ and $J_2$. The green shaded part is the unit cell choice.

*Spin trimer with $J_1 < J_2$.* The second part of this chapter, based on Ref. [126], we investigate for the first time the qualitatively distinct, strongly coupled regime, exemplified by the frustration-free linear Cu-based trimer chain compound $Cu_3(P_2O_6OH)_2$ [Fig. 5.2], which realizes the inverted hierarchy $J_1 < J_2$ [68]. In this material, inter- and intra-trimer coupling become comparable, placing the system outside the weak-trimer limit relevant to $Na_2Cu_3Ge_4O_{12}$. The character of spin excitations on the $J_1 < J_2$ side of the $J_1 = J_2$ Heisenberg point has not been systematically addressed. Do high-energy modes originate from local or extended processes? How do they relate to spinons, and what are their spectroscopic fingerprints? Moreover, this class of trimer chains exhibits a robust 1/3 magnetization plateau [68] which is adiabatically distinct from the previous material. How the magnetization constraint reshapes multi-spin RIXS responses—and its role in

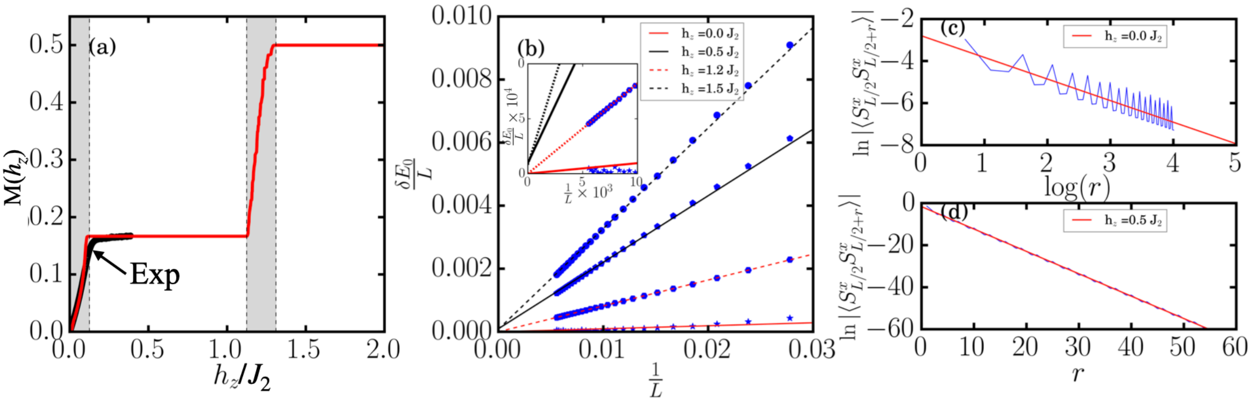

Figure 5.3: (a) Magnetization $M(h_z)$ (solid line) showing a 1/3 plateau at $M = 1/6$ and full saturation at $M = 0.5$, compared with experimental data from Ref. [68] (open circles). (b) Finite-size scaling of the excitation gap. (c) Correlation function $C^x(r) = \langle S^x_{L/2} S^x_{L/2+r} \rangle$ in the gapless phase, exhibiting power-law decay. (d) The same correlator in the gapped phase, exhibiting exponential decay.

shaping spin dynamics and emergent quasiparticles remains unclear—motivating a comprehensive analysis of their spectroscopic signatures and underlying quasiparticles.

We tackle these questions for $Cu_3(P_2O_6OH)_2$ using density matrix renormalization group (DMRG), exact diagonalization (ED), and effective low-energy modeling. We analyze both single-spin INS and multi-spin RIXS channels at zero field and across the 1/3 plateau.

Our study reveals that high-energy features in the spectra arise from *composite* quasiparticles, which are formed by excitations of *unconventional* trimer unit cells due to strong coupling between trimers. These composite modes are selectively enhanced by nonlocal multi-spin processes induced by RIXS, allowing direct experimental access to their internal structure. At zero magnetic field, RIXS detects a gapless excitation, identified as spinons using real-space renormalization techniques. In the mid- to high-energy range, the spectra show signatures of one- and two-trimer unit excitations, which we resolve using exact diagonalization. Applying a magnetic field modifies these features and leads to a crossover into a gapless $S = 1$ bosonic phase above the 1/3 magnetization plateau. Overall, our findings provide a general framework for understanding field-tunable high-energy spin dynamics in trimerized quantum magnets, and demonstrate that strongly coupled trimer chains are a promising platform for probing fractionalization and emergent quasiparticles.

## 5.2 Hamiltonian & RIXS perturbation

We model $Cu_3(P_2O_6OH)_2$ as a spin-1/2 antiferromagnetic trimer chain with $J_1$-$J_1$-$J_2$ couplings [Fig. 5.2]. The ratio $J_1/J_2 = 0.27$ is consistent with the structural analysis in chapter 1 (Sec. 1.2.1). We model $Cu_3(P_2O_6OH)_2$ as a spin-$\frac{1}{2}$ antiferromagnetic trimer chain with $J_1$-$J_1$-$J_2$ couplings [Fig. 5.2], where $J_1/J_2 = 0.27$ matches structural analysisin chapter 1 (Sec. 1.2.1). The Hamiltonian uses an *asymmetric* ($J_1$-$J_2$) unit cell [Fig. 5.2], linking local excitations to RIXS spectra. This choice avoids level crossings seen with symmetric $J_1$-trimer cells for $J_2 \gg J_1$. We refer to the ($J_1$-$J_2$) cell as the trimer unit cell or isolated trimer. Therefore the Hamiltonian is

$$H = \sum_{j}^{L/3} \left( J_1\, \mathbf{S}_j^1 \cdot \mathbf{S}_j^2 + J_2\, \mathbf{S}_j^2 \cdot \mathbf{S}_j^3 + J_1\, \mathbf{S}_j^3 \cdot \mathbf{S}_{j+1}^1 \right), \tag{5.1}$$

where $j$ indexes unit cells and $\{1, 2, 3\}$ label spins within each trimer.

Within the ultra-short core-hole lifetime (UCL) approximation [9, 82, 95, 125, 106], the Cu $L$ edge RIXS cross-section is expanded in the inverse core-hole lifetime $\Gamma$ (see Sec. 3.1.1, chapter 3). The $l$th-order contribution to the intensity in the non-spin-conserving (NSC) channel is

$$S^l(\mathbf{q}, \omega) = \frac{1}{\Gamma^{2l+2}} \sum_f \left| \left\langle f \left| \frac{1}{\sqrt{L}} \sum_i e^{i\mathbf{q}\cdot\mathbf{R}_i} O_{i,l} \right| g \right\rangle \right|^2 \delta(E_f - E_g - \omega), \tag{5.2}$$

with $O_{i,0} = S_i^x$, $O_{i,1} = \sum_{j\in \mathrm{NN}(i)} J_{ij} S_i^x\, \mathbf{S}_i \cdot \mathbf{S}_j$, and $O_{i,2} = \sum_{j\neq k \in \mathrm{NN}(i)} J_{ij} J_{ik} S_i^x\, (\mathbf{S}_i \cdot \mathbf{S}_j)(\mathbf{S}_i \cdot \mathbf{S}_k)$. See A.43 in Appendix A.2 Here, $|g\rangle$ and $|f\rangle$ are the ground and excited eigenstates of $H$ with energies $E_g$ and $E_f$, respectively. The $l = 0$ term creates single spin-flip excitations, whereas higher orders ($l > 0$) capture multi-spin correlations.

## 5.3 Results

### 5.3.1 Fractional magnetization plateau

We compute the ground state and the magnetization for a chain of length $L = 120$ using MPS-DMRG (iTensor [54]). Magnetization plateaus [Fig. 5.3(a)] satisfy $N_0(S - M) = I$, where $N_0$ is the number of spins per unit cell, $S$ is the spin magnitude (here $1/2$), $M \equiv S^z_T/L\,(= 1/6)$ is the magnetization per site, and $I$ is an integer. For $I = 1$ this gives $M = 1/6$, i.e., a 1/3 plateau [123].

The magnetization curve $M(h)$ [Fig. 5.3(a)] increases smoothly at low field, shows a 1/3 plateau between $0.179J_2$ and $1.1J_2$, and then evolves continuously to full polarization above $1.3J_2$. With $J_2 = 110$ K (9.48 meV), this plateau spans $14$-$85$ T, consistent with experiments [68, 69] (open circles Fig. 5.3(a)), using $h_z(T) = h_z J_2/(g\mu_B)$ with $g = 2.12$.

Shaded regions in Fig. 5.3(a) indicate gapless behavior, confirmed by finite-size scaling of the first excitation gap $\delta E_0/L$ [Fig. 5.3(b)], which extrapolates to zero; in contrast, the plateau and the fully polarized state are gapped. In the gapless phases, the spin correlations $C^x(r) = \langle S^x_{L/2} S^x_{L/2+r}\rangle$ decay as $1/r$ at $h_z = 0$ [Fig. 5.3(c)], with exponent $\eta = 1$, consistent with conformal charge $c = 1$ and the $S = 1/2$ HAC universality class [65] (see BOX 1). Inside the plateau, $C^x(r)$ decays exponentially [92] [Fig. 5.3(d)], signaling a gapped phase.

BOX 1: Scaling analysis and phase characterization

We identify the magnetic phases using the magnetization $M(h_z)$, the finite-size scaling of the excitation gap $\delta E_0/L$, and the decay of static spin-spin correlations $C^x(r) = \langle S^x_{L/2} S^x_{L/2+r}\rangle$ with special distance $r$ between the spins. Figure 5.3(a) shows a $1/3$ magnetization plateau for $0.179J_2 \leq h_z \leq 1.1J_2$, while full polarization sets in above $h_z \approx 1.32J_2$. In both the plateau and fully polarized regimes, $\delta E_0/L$ extrapolates to a nonzero value as $L \to \infty$ (e.g., $h_z = 0.5, 1.5$), indicating a gapped phase. In contrast, for $0 < h_z < 0.12J_2$ and $1.12J_2 < h_z < 1.32J_2$, the gap closes in the thermodynamic limit (e.g., $h_z = 0.0, 1.2$), signaling a gapless spectrum. Correlations are consistent with these findings: in the gapped plateau and fully polarized phases, $C^x(r)$ decays exponentially with $r$ [92] (e.g., $h_z = 0.5$ in Fig. 5.3(d)), whereas in the gapless regime it follows a power law, $C^x(r) \sim 1/r^\eta$ with $\eta \approx 1$ (e.g., $h_z = 0$ in Fig. 5.3(c)), consistent with a $c = 1$ conformal field theory and the spin-$\frac{1}{2}$ HAC universality class [65]. The oscillations in $C^x(r)$ arise from the trimer pattern of couplings $J_1$ (weak) and $J_2$ (strong) and are most pronounced in the gapless phase (Fig. 5.3(c)).

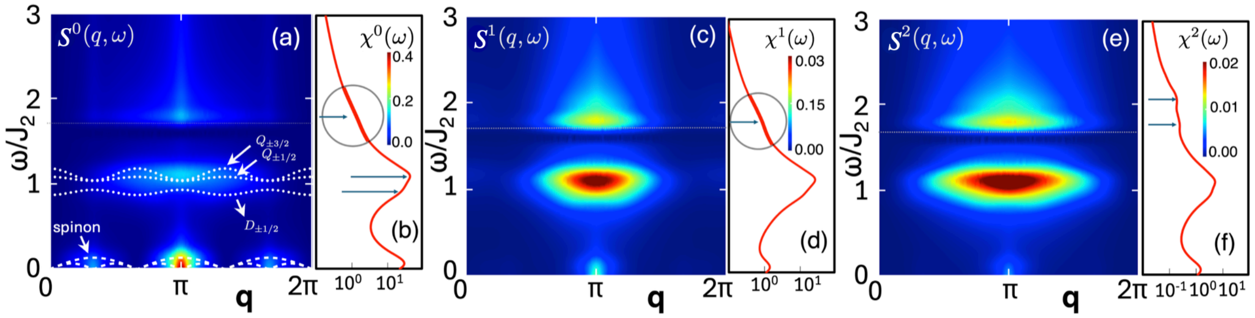

Figure 5.4: **Zero-field RIXS spectra:** (a,c,e) DMRG results for $S_l(\mathbf{q}, \omega)$ with $l = 0, 1, 2$ on 120 sites. (b,d,f) Corresponding $\mathbf{q}$-integrated ED spectra on 15 sites. In (a), the long-dashed curve marks the spinon continuum boundaries; dotted lines show single-trimer excitation dispersions. Data above $\omega = 1.8J_2$ is scaled by 10 in all panels.

### 5.3.2 RIXS Spectrum

**Zero-field RIXS:**

Figure 5.4 summarizes the dynamical structure factor $S^l(\mathbf{q}, \omega)$ at zero magnetic field for UCL expansion's orders $l = 0, 1$, and 2. For $l = 0$ [Fig. 5.4(a)], $S^0(\mathbf{q}, \omega)$ exhibits three clearly separated features. (i) A lowest-energy, gapless mode extends up to $\omega/J_2 \sim 0.135$, with spectral weight centered at momenta $\mathbf{q} = \frac{(2n+1)\pi}{3}$ $(n = 0, 1, 2)$. (ii) A mid-energy feature occurs near $\mathbf{q} = \pi$ and $\omega = 1.11J_2$, and resolves into two nearby peaks in the $\mathbf{q}$-integrated spectra [Fig. 5.4(b), arrows]. (iii) A weak high-energy shoulder appears around $\omega \sim 1.8J_2$ [small bump marked by an encircled arrow in Fig. 5.4(b)]. To clarify the origin of these structures, we analyze $S^0(\mathbf{q}, \omega)$ using exact diagonalization (ED). To resolve these features, we examine the spectra of single and coupled $J_1 - J_2$ trimer unit cells and derive a low-energy effective Hamiltonian. The exact diagonalization (ED) spectrum of an isolated trimer [Fig. 5.5(a)] reveals eight eigenstates grouped into: a doubly-degenerate $S = 1/2$ ground state $|S\rangle_\sigma$ at $E_S = -0.7655J_2$, a $|D\rangle_\sigma$ doublet at $E_D = 0.1305J_2$, and a fourfold $S = 3/2$ quadruplet $|Q\rangle_\sigma$ at $E_Q = 0.3175J_2$. Two *decoupled* trimers yield 64 states organized into product sectors: $|SS\rangle$, $|SD\rangle$, $|SQ\rangle$, $|DD\rangle$, $|DQ\rangle$, $|QQ\rangle$, where the first (second) label refers to the state on the first (second) trimer (spin labels suppressed for brevity). These yield a fourfold ground state at $2E_S$, and excited states at $E_{SD} = 0.896J_2$, $E_{SQ} = 1.083J_2$, $E_{DD} =$

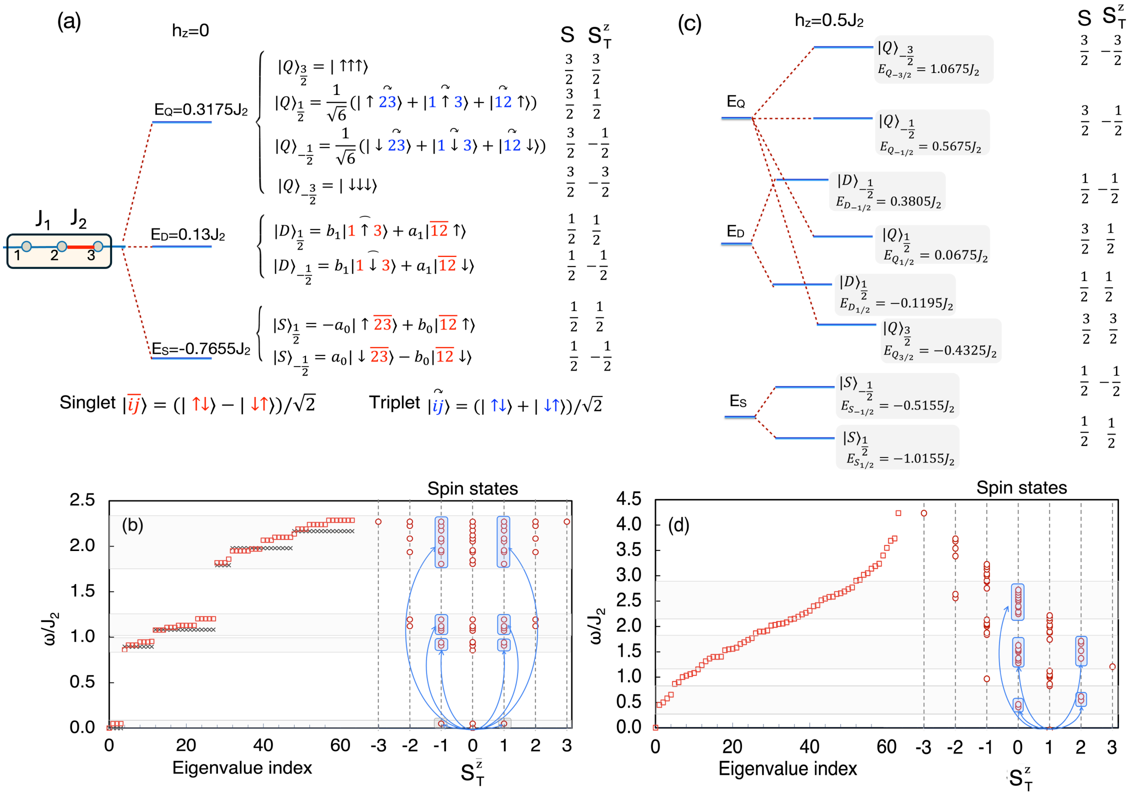

Figure 5.5: **Trimer spectra:** (a, c) Single-trimer eigenspectrum and spin configurations at $h_z = 0$ and $0.5J_2$, with site labels defined in the trimer schematic (a). Coefficients of the eigenstates are $a_0 = 0.91531$, $b_0 = 0.151984$, $a_1 = 0.4407$ and $b_1 = 0.703949$. (b) Two-trimer spectra for $h_z = 0$. The crosses show decoupled levels, squares show coupled levels, and corresponding $S_T^z$ for the coupled levels are shown in the right. (d) provides the two coupled trimers spectra and the $S_T^z$ values for $h_z = 0.5J_2$. In (b) and (d), the blue arrows mark allowed $\Delta S^z = \pm 1$ transitions from the respective ground states.

$1.792J_2$, $E_{DQ} = 1.979J_2$, and $E_{QQ} = 2.166J_2$ relative to the ground state (crosses in Fig. 5.5(b)). Including inter-trimer coupling broadens the spectrum (red squares enclosed by gray bands). The coupled ground state ($|g\rangle_{2\mathrm{Tr}}$) becomes non-degenerate with $S_T^z = 0$ and is dominated by $|SS\rangle$ components. The blue arrows on the right of Fig. 5.5(b) mark allowed $\Delta S^z = \pm 1$ transitions that contribute to $S^0(\mathbf{q}, \omega)$. We first examine single-spin-flip excitations ($\Delta S^z = \pm 1$) of the coupled ground state $|g\rangle_{2\mathrm{Tr}}$, located in the lowest gray band of Fig. 5.5(b) (lowest blue arrows). At $l = 0$ the RIXS operator reduces to $O_{i,0} = S_i^x$, which flips a single local spin. We ask whether such a single-spin flip fractionalizes in the trimerized system. A real-space renormalization-group derivation of the effective low-energy model [110, 109] (details in Appendix B.1.1) yields

$$H_{\text{eff}} = J_{\text{eff}} \sum_{i}^{L/3} \widetilde{\mathbf{S}}_i \cdot \widetilde{\mathbf{S}}_{i+1} + J'_{\text{eff}} \sum_{i}^{L/3} \widetilde{\mathbf{S}}_i \cdot \widetilde{\mathbf{S}}_{i+2}, \tag{5.3}$$

where each trimer is mapped to an effective spin-$1/2$ $\widetilde{\mathbf{S}}$, with $J_{\text{eff}} = 0.16J_1$ and $J'_{\text{eff}} \sim 10^{-4}J_1$. Because $J'_{\text{eff}} \ll J_{\text{eff}}$, the excitations form a spinon continuum with lower and upper boundaries $\omega = \frac{J_{\text{eff}}}{2}|\sin(3\mathbf{q})|$ and $\omega = \pi J_{\text{eff}}|\sin(3\mathbf{q}/2)|$, respectively. The factor of three in the arguments reflects zone folding, since one trimer maps to one effective site. The continuum boundaries (long-dashed curves in Fig. 5.4(a)) agree with the DMRG data, establishing that the lowest feature consists of deconfined spinons at $l = 0$.

The remaining spin-flip-allowed ($\Delta S^z = \pm 1$) transitions (blue arrows in Fig. 5.5(b)) reveal two types of high-energy excitations. We demonstrate that the first dominates at $l = 0$, while the second appears prominently only at $l > 0$. The first involves single-trimer excitations: $|SS\rangle$ components of $|g\rangle_{2\text{Tr}}$ connect to $|SD\rangle$ or $|SQ\rangle$ sectors via local spin flips ($O_{i,0} = S_i^x$), yielding $|D\rangle_{\pm 1/2}$ at $0.896J_2$ and $|Q\rangle_{\pm 1/2, \pm 3/2}$ at $1.083J_2$, matching the mid-energy peaks in Fig. 5.4(a). To quantify their dispersion, we evaluate these single-trimer excitations on a staggered product ansatz $\prod_i^{L/3} |S\rangle_{(-1)^i 1/2}$ (Appendix B.2.1). The resulting dispersions (fine-dashed lines in Fig. 5.4(a)) align with the centroids of the gray bands in Fig. 5.5(b). The second kind involves excitations from $|SD\rangle$ and $|SQ\rangle$ components to two-trimer sectors $|DD\rangle$, $|DQ\rangle$, or $|QQ\rangle$, also via local spin flips. For example, $|D\rangle_{-1/2}|D\rangle_{-1/2}$ at $1.791J_2$ underlies the high-energy bump near $\omega \sim 1.8J_2$ in Fig. 5.4(a). It lies at the bottom of the highest gray band in Fig. 5.5(b), while $|Q\rangle_{3/2}|Q\rangle_{-1/2}$ and $|Q\rangle_{-1/2}|Q\rangle_{-1/2}$ define its upper edge $2.08J_2$. However, due to the dominance of $|SS\rangle$ in the ground state, these composite excitations appear with very weak intensity at $l = 0$ [Fig. 5.4(a)].

These latter excitations—from $|g\rangle_{2\text{Tr}}$ to $|DD\rangle$, $|DQ\rangle$, or $|QQ\rangle$—are significantly enhanced at higher RIXS orders. At first order ($l = 1$), the RIXS operator reduces to

$$O_{l=1} = \frac{1}{4}\sum_i \left(J_{i,i-1}S^x_{i-1} + J_{i,i+1}S^x_{i+1}\right) e^{i\mathbf{q}\cdot\mathbf{r}_i} \\ + i\sum_i \left[J_{i,i-1}S^z_i S^y_{i-1}\left(1 - e^{-i\mathbf{q}\cdot\mathbf{a}}\right) + J_{i,i+1}S^z_i S^y_{i+1}\left(1 - e^{i\mathbf{q}\cdot\mathbf{a}}\right)\right] e^{i\mathbf{q}\cdot\mathbf{r}_i}. \tag{5.4}$$

These contributions can act within a single trimer or simultaneously on neighboring trimers. The latter is a *non-local* process that enables intra- and inter-trimer excitations. In the two-trimer problem, $O_{i,1}$ can scatter the $|SS\rangle$ components of $|g\rangle_{2\mathrm{Tr}}$ (See BOX 2) with $S^z_T = 0$ directly into $|DD\rangle$, $|DQ\rangle$, and $|QQ\rangle$ states with $\Delta S^z = \pm 1$. As a result, spectral weight is transferred from the spinon continua to higher-energy composite modes, as seen in Fig. 5.4(c,d).

This redistribution amplifies at second order ($l = 2$) [Fig. 5.4(e,f)]. The second-order operator simplifies to:

$$O_{l=2} = \sum_{j,k} J_{i,j}J_{i,k}S^x_i\left(\mathbf{S}_i\cdot\mathbf{S}_j\right)\left(\mathbf{S}_i\cdot\mathbf{S}_k\right) = \frac{5}{4}\sum_{j,k} J_{i,j}J_{i,k}S^x_i(\mathbf{S}_j\cdot\mathbf{S}_k) - i\sum_{j,k} J_{i,j}J_{i,k}S^x_i\mathbf{S}_i\cdot(\mathbf{S}_j\times\mathbf{S}_k). \tag{5.5}$$

The second term (scalar chirality) vanishes in non-chiral systems. The dominant nontrivial inter-trimer contribution arises from $\frac{5}{4}\sum_{j\neq k} J_{i,j}J_{i,k}S^x_i(\mathbf{S}_j\cdot\mathbf{S}_k)$, where $j$ and $k$ are nearest neighbors of site $i$ and $j \neq k$ . Consistently, Fig. 5.4(f) displays clear multiplet features at $E_{DQ}$ and $E_{QQ}$, associated with $|DQ\rangle$ and $|QQ\rangle$ states (arrows). hese results show that higher-order RIXS processes involve non-local spin operators, enabling additional pathways to composite excitations and enhancing their spectral weight. Since such terms are suppressed by $1/\Gamma^{2l}$ in the UCL expansion, their selective enhancement may be extracted by combining RIXS with inelastic neutron scattering (INS), to filter out the $l = 0$ single-spin-flip channel [139, 172].

### 5.3.3 Quasiparticle excitations

We now clarify the microscopic origin of high-energy modes (see Appendix B.2). We compute the dispersion of isolated single-trimer excitations over a staggered product ground state ansatz $\prod_i^{L/3}|S\rangle_{(-1)^i 1/2}$. This captures the dominant structure of the exact ground state as verified via ED.

BOX 2: Analysis of two-trimer excitations in zero magnetic field at various orders of RIXS

To understand the features observed in the RIXS spectra and their dependence on the scattering order, we analyze the two-trimer singlet-like ground state at zero field: $|g\rangle_{2\mathrm{Tr}} = \frac{1}{\sqrt{2}}\left(|S\rangle_{-1/2} \otimes |S\rangle_{1/2} - |S\rangle_{1/2} \otimes |S\rangle_{-1/2}\right)$, where $|S\rangle_{\pm 1/2}$ are single trimer ground states (see Fig. 5.4(a) ).

The resulting dispersive bands, arising from local $|S\rangle \rightarrow |D\rangle$ and $|S\rangle \rightarrow |Q\rangle$ excitations, lie within the mid-energy regime and track the features seen in the full $S^0(q, \omega)$ [Fig. 5.4(a)], confirming their identification as single-trimer composite quasiparticles. To validate this further, we compute $S^0(q, \omega)$ using a truncated basis comprising only such product states and the relevant excited sectors, but incorporate the exact numerical ground state. The resulting spectra closely match the energy and momentum structure of the full ED and DMRG response (Appendix B.2.2, Fig. B.2). This demonstrates that the mid-energy features originate from well-defined dispersing quasiparticles connected to ($J_1 - J_2$)-trimer unit-cell excitations. We find that these quasiparticle features persist for $J_1/J_2 \in [0.05, 0.5]$; below, dimer excitations dominate, and above, they merge into a continuum.

**RIXS spectra at magnetization plateau:**

We now turn to the behavior of the RIXS spectra at the one-third magnetization plateau, focusing first on the single- and two-trimer excitations. Figures 5.5(c) and (d) display the corresponding single- and two-trimer energy levels at the midpoint of the plateau ($h_z = 0.5J_2$). In the single-trimer case [Fig. 5.5(c)], the levels $|S\rangle_\sigma$, $|D\rangle_\sigma$, and $|Q\rangle_\sigma$ split in the presence of the magnetic field. Spin-aligned states shift to lower energy, while anti-aligned states shift upward, completely lifting the degeneracies. Once two trimers are coupled [Fig. 5.5(d)], these discrete levels broaden into a quasi-continuum. At the plateau, the ground state of the two-trimer system carries total spin $S^z_T = 1$ ($M = 1/6$), and exact diagonalization (ED) shows that it is well approximated by the direct product ground state $|\tilde{g}\rangle_{\mathrm{plat}} = |S_1\rangle_\uparrow \otimes |S_2\rangle_\uparrow$. Excitations with $\Delta S^z = \pm 1$ fall within narrow energy windows, highlighted by the horizontal bands and blue arrows in Fig. 5.5(d).

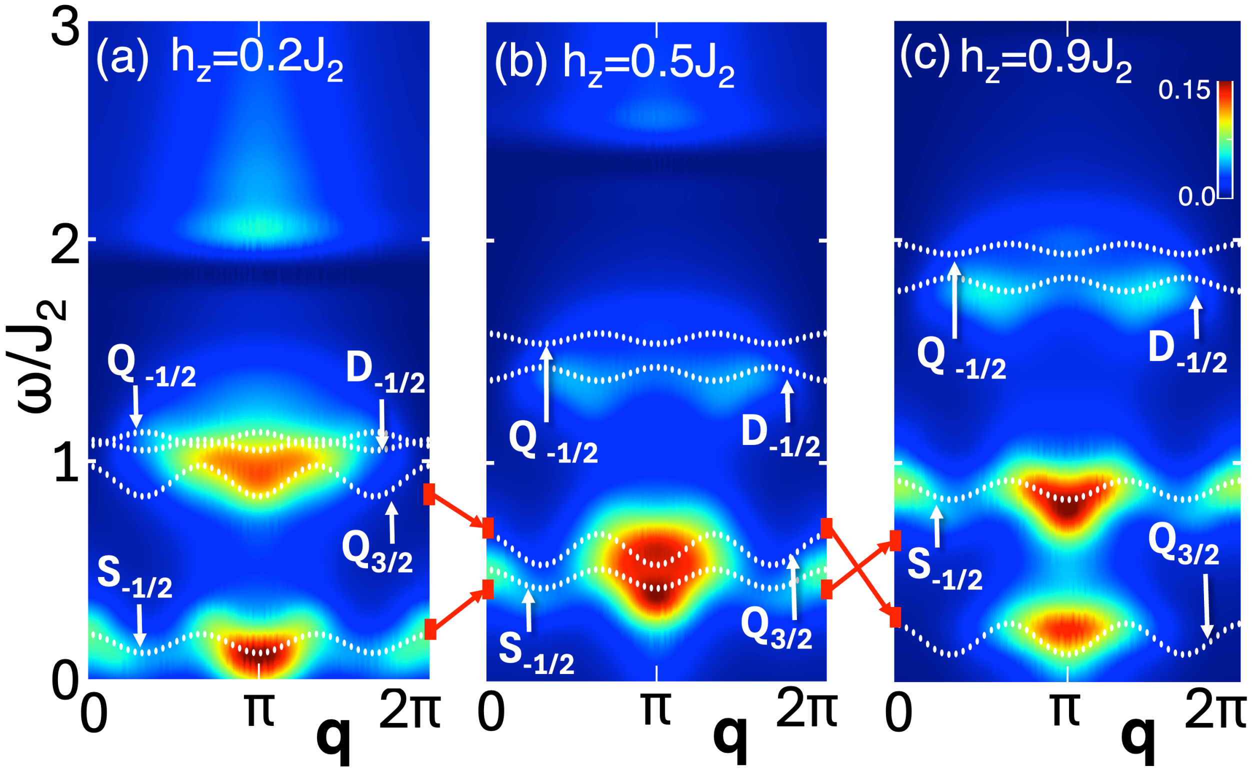

Figure 5.6: **RIXS at finite field:** $S^0(\mathbf{q},\omega)$ for indicated $h_z$ values. Long-dashed lines across the three panels show analytically predicted feature locations and their $h_z$-dependent evolution; Inset in (b) shows the dispersions of low-energy modes discussed in the text. Color scale is identical across all panels.

The full RIXS intensity $S^0(\mathbf{q},\omega)$, calculated at $h_z = 0.2J_2$, $0.5J_2$, and $0.9J_2$, is shown in Figs. 5.6(a-c). At the plateau midpoint ($h_z = 0.5J_2$) [Fig. 5.6(b)], two dominant features appear at $\omega \approx 0.5J_2$ and $1.5J_2$, consistent with the gray bands in Fig. 5.5(d). ED studies of up to four trimers confirm that the plateau ground state remains well approximated by the direct product $|\tilde{g}\rangle_{\text{plat}} = \prod_{i=1}^{L/3} |S_i\rangle_\uparrow$. The low-energy band near $0.58J_2$ originates from single-trimer excitations $|S\rangle_{1/2} \to |S\rangle_{-1/2}$ and $|S\rangle_{1/2} \to |Q\rangle_{3/2}$, both corresponding to $\Delta S^z = \pm 1$. The mid-energy band near $1.5J_2$ arises from transitions $|S\rangle_{1/2} \to |D\rangle_{-1/2}$ $(1.37J_2)$ and $|S\rangle_{1/2} \to |Q\rangle_{-1/2}$ $(1.54J_2)$. At higher energies, around $2.5J_2$ [Fig. 5.5(d)], multi-trimer processes such as $|S\rangle_{1/2}|D\rangle_{1/2} \to |D\rangle_{-1/2}|D\rangle_{1/2}$ contribute to a broad continuum, but these are strongly suppressed due to the nearly product-state nature of $|\tilde{g}\rangle_{\text{plat}}$. For the same reason, higher angular momentum ($l > 0$) contributions do not significantly modify the $l = 0$ RIXS response. The dispersions of the single-trimer quasiparticles, tracked by dashed lines in Fig. 5.6(b) (inset), confirm this interpretation.

A simplified analytical description of $S^0(\mathbf{q}, \omega)$ can be obtained by approximating the single-trimer plateau state $|S_i\rangle_\uparrow$ as $|\uparrow, \overline{bc}\rangle$, with the 'a'-site spin polarized and the 'b-c' pair forming a singlet (see appendix B.2.3). Within this approximation, the response takes the form

$$S^0(\mathbf{q}, \omega) = \frac{1}{3}\delta(\omega - h_z) + \frac{2}{3}\sin^2(qa/2)\Big[\delta(\omega - J_2 + h_z/2) + \delta(\omega - J_2 - h_z)\Big],$$

which reproduces the three key low-energy features and captures their linear dependence on the applied field $h_z$. The small rectangles in Figs. 5.6(a-c) mark these analytical predictions, which qualitatively follow the numerical DMRG results. Importantly, as the field is increased to $h_z = 0.9J_2$ [Fig. 5.6(c)], the $|Q\rangle_{3/2}$ excitation becomes the lowest-energy mode, signaling the proximity to the plateau endpoint.

Beyond the critical field $h_z = 1.12J_2$, the magnetization plateau collapses and the spectrum becomes gapless, with $|Q\rangle_{3/2}$ excitations dominating the low-energy sector (appendix B.3). Just above the plateau, the magnetization increases smoothly but remains below full polarization, reflecting the gradual population of trimer $|Q\rangle_{3/2}$ states via $\Delta S = 1$ single-trimer processes that break singlet bonds, $|1_\uparrow, \overline{2, 3}\rangle \rightarrow |1_\uparrow 2_\uparrow 3_\uparrow\rangle$. These excitations can be viewed as emergent magnons—composite bosonic quasiparticles arising from singlet-to-triplet bond transitions—which delocalize through inter-trimer couplings. The resulting low-energy theory corresponds to a gapless $S = 1$ Luttinger liquid.

Interestingly, such composite magnons may condense at finite temperature into a Bose-Einstein condensate (BEC), stabilized by dimensional crossover effects in real materials such as $Cu_3(P_2O_6OH)_2$. This scenario is reminiscent of magnon BEC observed in dimer systems like $TlCuCl_3$ [142] and in the quasi-1D compound $KGaCu(PO_4)_2$ [30].

## 5.4 Conclusion

We have established the experimental relevance of our theoretical predictions for fractionalized quasiparticles—namely spinons, doublons, and quartons—in the spin-$\frac{1}{2}$ trimer chain compound $\mathrm{Cu_3(P_2O_6OH)_2}$. Taking $J_1 = 9.48\,\mathrm{meV}$ as the natural energy scale, we find that spinons dominate the low-energy sector, extending up to $\sim 1.5\,\mathrm{meV}$, while doublons disperse up to $\sim 10\,\mathrm{meV}$. Quartons appear as gapped excitations near $\sim 20\,\mathrm{meV}$, but above the one-third magnetization plateau they soften into gapless modes that disperse up to $\sim 2\,\mathrm{meV}$. These energy windows are well within the resolution of modern soft X-ray RIXS and inelastic neutron scattering [89, 90], which makes our predictions directly accessible to experiment.

A key outcome of our analysis is the identification of field-induced, gapless $S = 1$ quasiparticles that emerge above the plateau. These excitations form a dispersive continuum, consistent with a Luttinger liquid description of interacting spin-1 bosons in one dimension [59]. This establishes $\mathrm{Cu_3(P_2O_6OH)_2}$ as a rare platform where fractionalized Luttinger liquid behavior coexists with emergent Bose-Einstein condensation (BEC) physics, the latter being stabilized by temperature-driven dimensional crossover effects Such coexistence is of particular interest because it provides a bridge between one-dimensional quantum criticality and three-dimensional long-range order.

It is instructive to contrast this behavior with that of trimer chains in the opposite exchange regime ($J_1 > J_2$). In such systems, exemplified by $\mathrm{Na_2Cu_3Ge_4O_{12}}$, the RIXS spectra are significantly broader and the critical fields required to destabilize the plateau are substantially higher, reaching values as large as $\sim 200\,\mathrm{T}$ [33, 102]. By comparison, $\mathrm{Cu_3(P_2O_6OH)_2}$ requires only $\sim 85\,\mathrm{T}$ to close the plateau gap [112, 80, 100], reflecting how the relative hierarchy of exchange couplings crucially governs the accessibility of exotic excitations in these materials.

Taken together, our results highlight the pivotal role of geometric trimerization in shaping the quasiparticle spectrum and field response of low-dimensional magnets. Moreover, they demonstrate how momentum- and energy-resolved probes such as RIXS provide unique, nonlocal access to fractionalized spinons, doublons, and quartons, as well as to emergent condensate phases. This establishes trimerized spin chains as versatile platforms for exploring the interplay between fractionalization, Luttinger liquid physics, and field-tunable magnon condensation in quantum magnets.

# Chapter 6

# Conclusions and Perspectives

Strongly correlated electron systems represent a frontier in condensed matter physics, where the interplay of electron-electron interactions gives rise to a wealth of emergent quantum phenomena such as magnetism, Mott insulating behavior, and high-temperature superconductivity [40]. This thesis investigates the fundamental mechanisms underlying these phenomena, focusing on the collective excitations and quasiparticle dynamics that define the low-energy physics of correlated materials. The overarching goal of this work has been to develop a microscopic understanding of how strong correlations manifest in both one- and two-dimensional quantum magnets, and to demonstrate how modern spectroscopic techniques, particularly resonant inelastic X-ray scattering (RIXS), can probe their underlying quantum dynamics.

The research highlights the role of quantum criticality and dimensionality in shaping the excitation spectrum of correlated materials. In low-dimensional systems, quantum fluctuations are enhanced, leading to phenomena such as spin fractionalization and the emergence of exotic quasiparticles such as spinons, doublons, triplons, and magnons [137, 142, 30]. The thesis explores how geometric modulation, such as trimerization in spin chains, gives rise to a hierarchy of fractionalized and composite excitations, tunable by external fields. These findings underscore the importance of exchange hierarchy and symmetry in governing the accessibility and character of quasiparticles, and demonstrate how field-induced transitions can drive systems between distinct quantum phases, including magnetization plateaus and Luttinger liquid regimes [59, 68, 126]. In this context, the central objective of this thesis has been to bridge theoretical modeling and experimental observables, establishing a unified framework for interpreting the complex excitation spectra of correlated cuprates.

The thesis provides new insights into the hierarchy of magnetic excitations in two-dimensional antiferromagnets, revealing the nature of higher-order multi-magnon excitations [125] bserved in Cu $L_3$ edge RIXS experiment [139]. These excitations, including dispersive three-magnon excitation, could play a potential role in the spin-fluctuation-mediated pairing mechanism of high-temperature superconductivity [143, 40].

Overall, the thesis advances a coherent narrative that connects the microscopic origins of strong correlations to the macroscopic observables accessible in modern experiments. By integrating theoretical modeling, numerical simulation, and spectroscopic analysis, it demonstrates how RIXS and related techniques can unravel the complex dynamics of spin and charge excitations in low-dimensional quantum materials. The findings not only deepen our understanding of the fundamental physics of strongly correlated systems but also pave the way for future explorations of exotic quantum phases, fractionalization, and the mechanisms underlying high-temperature superconductivity.

In summary, this work establishes a unified framework for probing and interpreting the emergent phenomena in strongly correlated electron systems. It highlights the power of RIXS as a central tool for investigating collective excitations, the utility of advanced computational methods for modeling complex quantum dynamics, and the rich interplay between geometry, dimensionality, and external fields in shaping the landscape of quasiparticles and quantum criticality. The insights gained here lay the groundwork for ongoing and future research into the quantum many-body problem, with implications for both fundamental science and the development of novel quantum materials.

# References

[1] *The Theory of Inelastic Neutron Scattering Spectroscopy*, pages 13–65.

[2] Ar. Abanov and Andrey V. Chubukov. A relation between the resonance neutron peak and arpes data in cuprates. *Phys. Rev. Lett.*, 83:1652–1655, Aug 1999.

[3] P. Abbamonte, A. Rusydi, S. Smadici, G. D. Gu, G. A. Sawatzky, and D. L. Feng. Spatially modulated 'mottness' in la2-xbaxcuo4. *Nature Physics*, 1(3):155–158, 2005.

[4] Peter Abbamonte and Jörg Fink. Collective charge excitations studied by electron energy-loss spectroscopy, 2024.

[5] Bekir Aktaş. *A Survey of Nanomagnetism*, pages 1–21. Springer Berlin Heidelberg, Berlin, Heidelberg, 2002.

[6] L. J. P. Ament and G. Khaliullin. Theory of raman and resonant inelastic x-ray scattering from collective orbital excitations in $YTiO_3$. *Phys. Rev. B*, 81:125118, Mar 2010.

[7] Luuk J. P. Ament, Giacomo Ghiringhelli, Marco Moretti Sala, Lucio Braicovich, and Jeroen van den Brink. Theoretical demonstration of how the dispersion of magnetic excitations in cuprate compounds can be determined using resonant inelastic x-ray scattering. *Phys. Rev. Lett.*, 103:117003, Sep 2009.

[8] Luuk J. P. Ament, Giniyat Khaliullin, and Jeroen van den Brink. Theory of resonant inelastic x-ray scattering in iridium oxide compounds: Probing spin-orbit-entangled ground states and excitations. *Phys. Rev. B*, 84:020403, Jul 2011.

[9] Luuk J. P. Ament, Michel van Veenendaal, Thomas P. Devereaux, John P. Hill, and Jeroen van den Brink. Resonant inelastic x-ray scattering studies of elementary excitations. *Rev. Mod. Phys.*, 83:705–767, Jun 2011.

[10] P. W. Anderson. Antiferromagnetism. theory of superexchange interaction. *Phys. Rev.*, 79:350–356, Jul 1950.

[11] P. W. Anderson. The resonating valence bond state in $La_2CuO_4$ and superconductivity. *Science*, 235(4793):1196–1198, 1987.

[12] J. D. Axe and M. K. Crawford. Structural instabilities in lanthanum cuprate superconductors. *Journal of Low Temperature Physics*, 95(1):271–284, April 1994.

[13] G. Balakrishnan and R. Vijayaraghavan. On the electron superconductors $\mathrm{nd}_{2-x}\mathrm{ce}_x\mathrm{cuo}_{4-y}$. *Bulletin of Materials Science*, 14(2):287–290, April 1991.

[14] A. S. BARKER and R. LOUDON. Response functions in the theory of raman scattering by vibrational and polariton modes in dielectric crystals. *Rev. Mod. Phys.*, 44:18–47, Jan 1972.

[15] Alfred Q. R. Baron. Introduction to high-resolution inelastic x-ray scattering, 2020.

[16] Susmita Basak, Tanmoy Das, Hsin Lin, M. Z. Hasan, R. S. Markiewicz, and A. Bansil. Coexisting pseudogap, charge-transfer-gap, and mott-gap energy scales in the resonant inelastic x-ray scattering spectra of electron-doped cuprate superconductors. *Phys. Rev. B*, 85:075104, Feb 2012.

[17] J. G. Bednorz and K. A. Müller. Possible hightc superconductivity in the ba−la−cu−o system. *Zeitschrift für Physik B Condensed Matter*, 64(2):189–193, 1986.

[18] Anup Kumar Bera, S. M. Yusuf, Sudip Kumar Saha, Manoranjan Kumar, David Voneshen, Yurii Skourski, and Sergei A. Zvyagin. Emergent many-body composite excitations of interacting spin-1/2 trimers. *Nature Communications*, 13(1):6888, 2022.

[19] Anup Kumar Bera, SM Yusuf, Sudip Kumar Saha, Manoranjan Kumar, David Voneshen, Yurii Skourski, and Sergei A Zvyagin. Emergent many-body composite excitations of interacting spin-1/2 trimers. *Nature Communications*, 13(1):6888, 2022.

[20] H. Bethe. Zur theorie der metalle. *Zeitschrift für Physik*, 71(3):205–226, Mar 1931.

[21] Davide Betto, Roberto Fumagalli, Leonardo Martinelli, Matteo Rossi, Riccardo Piombo, Kazuyoshi Yoshimi, Daniele Di Castro, Emiliano Di Gennaro, Alessia Sambri, Doug Bonn, George A. Sawatzky, Lucio Braicovich, Nicholas B. Brookes, José Lorenzana, and Giacomo Ghiringhelli. Multiple-magnon excitations shape the spin spectrum of cuprate parent compounds. *Phys. Rev. B*, 103:L140409, Apr 2021.

[22] V. Bisogni, L. Simonelli, L. J. P. Ament, F. Forte, M. Moretti Sala, M. Minola, S. Huotari, J. van den Brink, G. Ghiringhelli, N. B. Brookes, and L. Braicovich. Bimagnon studies in cuprates with resonant inelastic x-ray scattering at the o $k$ edge. i. assessment on la$_2$cuo$_4$ and comparison with the excitation at cu $L_3$ and cu $k$ edges. *Phys. Rev. B*, 85:214527, Jun 2012.

[23] L. Braicovich, L. J. P. Ament, V. Bisogni, F. Forte, C. Aruta, G. Balestrino, N. B. Brookes, G. M. De Luca, P. G. Medaglia, F. Miletto Granozio, M. Radovic, M. Salluzzo, J. van den Brink, and G. Ghiringhelli. Dispersion of magnetic excitations in the cuprate La$_2$CuO$_4$ and CaCuO$_2$ compounds measured using resonant x-ray scattering. *Phys. Rev. Lett.*, 102:167401, Apr 2009.

[24] L. Braicovich, M. Moretti Sala, L. J. P. Ament, V. Bisogni, M. Minola, G. Balestrino, D. Di Castro, G. M. De Luca, M. Salluzzo, G. Ghiringhelli, and J. van den Brink. Momentum and polarization dependence of single-magnon spectral weight for Cu $L_3$-edge resonant inelastic x-ray scattering from layered cuprates. *Phys. Rev. B*, 81:174533, May 2010.

[25] L. Braicovich, A. Tagliaferri, E. Annese, G. Ghiringhelli, C. Dallera, F. Fracassi, A. Palenzona, and N. B. Brookes. Spectroscopy of strongly correlated systems: Resonant x-ray scattering without energy resolution in the scattered beam. *Phys. Rev. B*, 75:073104, Feb 2007.

[26] L. Braicovich, J. van den Brink, V. Bisogni, M. Moretti Sala, L. J. P. Ament, N. B. Brookes, G. M. De Luca, M. Salluzzo, T. Schmitt, V. N. Strocov, and G. Ghiringhelli. Magnetic excitations and phase separation in the underdoped la$_{2-x}$sr$_{x}$cuo$_{4}$ superconductor measured by resonant inelastic x-ray scattering. *Phys. Rev. Lett.*, 104:077002, Feb 2010.

[27] D. C. Cabra, A. Honecker, and P. Pujol. Magnetization plateaux in $n$-leg spin ladders. *Phys. Rev. B*, 58:6241–6257, Sep 1998.

[28] Jing Chen, E. Miles Stoudenmire, Yashar Komijani, and Piers Coleman. Matrix product study of spin fractionalization in the one-dimensional kondo insulator. *Phys. Rev. Res.*, 6:023227, Jun 2024.

[29] Jing Chen, E. Miles Stoudenmire, Yashar Komijani, and Piers Coleman. Matrix product study of spin fractionalization in the one-dimensional kondo insulator. *Phys. Rev. Res.*, 6:023227, Jun 2024.

[30] R Chen, H J Hu, Z Qu, T Li, C B Liu, C L Wang, S J Sun, C Dong, and Y Qiu. Field-induced bose–einstein condensation in zigzag spin chain kgacu(po4)2. *Journal of Physics: Condensed Matter*, 36(16):165801, jan 2024.

[31] Zhuoyu Chen, Yao Wang, Slavko N. Rebec, Tao Jia, Makoto Hashimoto, Donghui Lu, Brian Moritz, Robert G. Moore, Thomas P. Devereaux, and Zhi-Xun Shen. Anomalously strong near-neighbor attraction in doped 1d cuprate chains. *Science*, 373(6560):1235–1239, 2021.

[32] Jun-Qing Cheng, Jun Li, Zijian Xiong, Han-Qing Wu, Anders W Sandvik, and Dao-Xin Yao. Fractional and composite excitations of antiferromagnetic quantum spin trimer chains. *npj Quantum Materials*, 7(1):3, 2022.

[33] Jun-Qing Cheng, Zhi-Yao Ning, Han-Qing Wu, and Dao-Xin Yao. Quantum phase transition and composite excitations of antiferromagnetic spin trimer chains in a magnetic field. *npj Quantum Materials*, 9(1):96, 2024.

[34] R. Chitra and M. J. Rozenberg. Impurity effects in the quantum kagome system $\mathrm{ZnCu_3(OH)_6Cl_2}$. *Phys. Rev. B*, 77:052407, Feb 2008.

[35] R. Coldea, S. M. Hayden, G. Aeppli, T. G. Perring, C. D. Frost, T. E. Mason, S.-W. Cheong, and Z. Fisk. Spin waves and electronic interactions in $\mathrm{la_2cuo_4}$. *Phys. Rev. Lett.*, 86:5377–5380, Jun 2001.

[36] R. Comin, A. Frano, M. M. Yee, Y. Yoshida, H. Eisaki, E. Schierle, E. Weschke, R. Sutarto, F. He, A. Soumyanarayanan, Yang He, M. Le Tacon, I. S. Elfimov, Jennifer E. Hoffman, G. A. Sawatzky, B. Keimer, and A. Damascelli. Charge order driven by fermi-arc instability in $\mathrm{Bi_2Sr_{2-x}La_xCuO_{6+\delta}}$. *Science*, 343(6169):390–392, 2014.

[37] T. Cuk, D. H. Lu, X. J. Zhou, Z.-X. Shen, T. P. Devereaux, and N. Nagaosa. A review of electron–phonon coupling seen in the high-tc superconductors by angle-resolved photoemission studies (arpes). *physica status solidi (b)*, 242(1):11–29, 2005.

[38] Eduardo H. da Silva Neto, Riccardo Comin, Feizhou He, Ronny Sutarto, Yeping Jiang, Richard L. Greene, George A. Sawatzky, and Andrea Damascelli. Charge ordering in the electron-doped superconductor $\mathrm{Nd_{2-x}Ce_xCuO_4}$. *Science*, 347(6219):282–285, 2015.

[39] E. Dagotto, J. Riera, and D. Scalapino. Superconductivity in ladders and coupled planes. *Phys. Rev. B*, 45:5744–5747, Mar 1992.

[40] Elbio Dagotto. Correlated electrons in high-temperature superconductors. *Rev. Mod. Phys.*, 66:763–840, Jul 1994.

[41] B. Dalla Piazza, M. Mourigal, N. B. Christensen, G. J. Nilsen, P. Tregenna-Piggott, T. G. Perring, M. Enderle, D. F. McMorrow, D. A. Ivanov, and H. M. Rønnow. Fractional excitations in the square-lattice quantum antiferromagnet. *Nature Physics*, 11(1):62–68, Jan 2015.

[42] Andrea Damascelli, Zahid Hussain, and Zhi-Xun Shen. Angle-resolved photoemission studies of the cuprate superconductors. *Reviews of Modern Physics*, 75(2):473–541, 2003.

[43] Frank M. F. de Groot, Maurits W. Haverkort, Hebatalla Elnaggar, Amélie Juhin, Ke-Jin Zhou, and Pieter Glatzel. Resonant inelastic x-ray scattering. *Nature Reviews Methods Primers*, 4(1):45, 2024.

[44] J.van den Brink. The theory of indirect resonant inelastic x-ray scattering on magnons. *Europhysics Letters*, 80(4):47003, oct 2007.

[45] Thomas P. Devereaux and Rudi Hackl. Inelastic light scattering from correlated electrons. *Rev. Mod. Phys.*, 79:175–233, Jan 2007.

[46] A. Donkov and A. V. Chubukov. Momentum-dependent light scattering in a two-dimensional heisenberg antiferromagnet: Analysis of x-ray scattering data. *Phys. Rev. B*, 75:024417, Jan 2007.

[47] R. L. Doretto and Matthias Vojta. Quantum magnets with weakly confined spinons: Multiple length scales and quantum impurities. *Phys. Rev. B*, 80:024411, Jul 2009.

[48] D. S. Ellis, Jungho Kim, J. P. Hill, S. Wakimoto, R. J. Birgeneau, Y. Shvyd'ko, D. Casa, T. Gog, K. Ishii, K. Ikeuchi, A. Paramekanti, and Young-June Kim. Magnetic nature of the 500 mev peak in $\mathrm{La_{2-x}Sr_xCuO_4}$ observed with resonant inelastic x-ray scattering at the Cu $k$-edge. *Phys. Rev. B*, 81:085124, Feb 2010.

[49] V. J. Emery. Theory of high-$\mathrm{t_c}$ superconductivity in oxides. *Phys. Rev. Lett.*, 58:2794–2797, Jun 1987.

[50] V. J. Emery and G. Reiter. Mechanism for high-temperature superconductivity. *Phys. Rev. B*, 38:4547–4556, Sep 1988.

[51] V. J. Emery and G. Reiter. Quasiparticles in the copper-oxygen planes of high-$T_c$ superconductors: An exact solution for a ferromagnetic background. *Phys. Rev. B*, 38:11938–11941, Dec 1988.

[52] L. Facheris, S. D. Nabi, A. Glezer Moshe, U. Nagel, T. Rõ om, K. Yu. Povarov, J. R. Stewart, Z. Yan, and A. Zheludev. Confinement of fractional excitations in a triangular lattice antiferromagnet. *Phys. Rev. Lett.*, 130:256702, Jun 2023.

[53] L.D. Faddeev and L.A. Takhtajan. What is the spin of a spin wave? *Physics Letters A*, 85(6):375–377, 1981.

[54] Matthew Fishman, Steven R. White, and E. Miles Stoudenmire. The ITensor Software Library for Tensor Network Calculations. *SciPost Phys. Codebases*, page 4, 2022.

[55] Filomena Forte, Luuk J. P. Ament, and Jeroen van den Brink. Magnetic excitations in $\mathrm{la_2Cuo_4}$ probed by indirect resonant inelastic x-ray scattering. *Phys. Rev. B*, 77:134428, Apr 2008.

[56] R. Fumagalli, L. Braicovich, M. Minola, Y. Y. Peng, K. Kummer, D. Betto, M. Rossi, E. Lefrançois, C. Morawe, M. Salluzzo, H. Suzuki, F. Yakhou, M. Le Tacon, B. Keimer, N. B. Brookes, M. Moretti Sala, and G. Ghiringhelli. Polarization-resolved cu $L_3$-edge resonant inelastic x-ray scattering of orbital and spin excitations in $\mathrm{ndba_2cu_3o_{7-\delta}}$. *Phys. Rev. B*, 99:134517, Apr 2019.

[57] Faris Gel'mukhanov, Michael Odelius, Sergey P. Polyutov, Alexander Föhlisch, and Victor Kimberg. Dynamics of resonant x-ray and auger scattering. *Rev. Mod. Phys.*, 93:035001, Jul 2021.

[58] G. Ghiringhelli, M. Le Tacon, M. Minola, S. Blanco-Canosa, C. Mazzoli, N. B. Brookes, G. M. De Luca, A. Frano, D. G. Hawthorn, F. He, T. Loew, M. Moretti Sala, D. C. Peets, M. Salluzzo, E. Schierle, R. Sutarto, G. A. Sawatzky, E. Weschke, B. Keimer, and

L. Braicovich. Long-range incommensurate charge fluctuations in $(\mathrm{Y}, \mathrm{Nd})\mathrm{Ba}_2\mathrm{Cu}_3\mathrm{O}_{6+\mathrm{x}}$. *Science*, 337(6096):821–825, 2012.

[59] T. Giamarchi. *Quantum Physics in One Dimension*. Oxford University Press, 2004.

[60] Thierry Giamarchi. *Quantum Physics in One Dimension*. Oxford University Press, 12 2003.

[61] John B. Goodenough. Theory of the role of covalence in the perovskite-type manganites $[\mathrm{La}, m(\mathrm{II})]\mathrm{Mno}_3$. *Phys. Rev.*, 100:564–573, Oct 1955.

[62] Frank M. F. de Groot, Maurits W. Haverkort, Hebatalla Elnaggar, Amélie Juhin, Ke-Jin Zhou, and Pieter Glatzel. Resonant inelastic X-ray scattering. *Nature Reviews Methods Primers*, 4(1):45, 2024.

[63] Anita Guarino, Carmine Autieri, Pasquale Marra, Antonio Leo, Gaia Grimaldi, Adolfo Avella, and Angela Nigro. Superconductivity induced by structural reorganization in the electron-doped cuprate $\mathrm{Nd}_{2-\mathrm{x}}\mathrm{Ce}_{\mathrm{x}}\mathrm{CuO}_4$. *Phys. Rev. B*, 105:014512, Jan 2022.

[64] M. Guarise, B. Dalla Piazza, M. Moretti Sala, G. Ghiringhelli, L. Braicovich, H. Berger, J. N. Hancock, D. van der Marel, T. Schmitt, V. N. Strocov, L. J. P. Ament, J. van den Brink, P.-H. Lin, P. Xu, H. M. Rønnow, and M. Grioni. Measurement of magnetic excitations in the two-dimensional antiferromagnetic $\mathrm{sr}_2\mathrm{cuo}_2\mathrm{cl}_2$ insulator using resonant x-ray scattering: Evidence for extended interactions. *Phys. Rev. Lett.*, 105:157006, Oct 2010.

[65] K. Hallberg, X. Q. G. Wang, P. Horsch, and A. Moreo. Critical behavior of the $S = 3/2$ antiferromagnetic heisenberg chain. *Phys. Rev. Lett.*, 76:4955–4958, Jun 1996.

[66] J. N. Hancock, G. Chabot-Couture, Y. Li, G. A. Petrakovskiĭ, K. Ishii, I. Jarrige, J. Mizuki, T. P. Devereaux, and M. Greven. Resonant inelastic x-ray scattering in electronically quasi-zero-dimensional $\mathrm{cub}_2\mathrm{o}_4$. *Phys. Rev. B*, 80:092509, Sep 2009.

[67] Yoshihisa Harada, Kozo Okada, Ritsuko Eguchi, Akio Kotani, Hidenori Takagi, Tomoyuki Takeuchi, and Shik Shin. Unique identification of zhang-rice singlet excitation in $sr_2cuo_2cl_2$ mediated by the o $1s$ core hole: Symmetry-selective resonant soft x-ray raman scattering study. *Phys. Rev. B*, 66:165104, Oct 2002.

[68] Masashi Hase, Masanori Kohno, Hideaki Kitazawa, Naohito Tsujii, Osamu Suzuki, Kiyoshi Ozawa, Giyuu Kido, Motoharu Imai, and Xiao Hu. 1/ 3 magnetization plateau observed in the spin-1/ 2 trimer chain compound $Cu_3(P_2O_6OH)_2$. *Physical Review B-Condensed Matter and Materials Physics*, 73(10):104419, 2006.

[69] Masashi Hase, Masaaki Matsuda, Kazuhisa Kakurai, Kiyoshi Ozawa, Hideaki Kitazawa, Naohito Tsujii, Andreas Dönni, Masanori Kohno, and Xiao Hu. Direct observation of the energy gap generating the $1/3$ magnetization plateau in the spin-$1/2$ trimer chain compound $cu_3(P_2O_6OD)_2$ by inelastic neutron scattering measurements. *Phys. Rev. B*, 76:064431, Aug 2007.

[70] M. W. Haverkort. Theory of resonant inelastic x-ray scattering by collective magnetic excitations. *Phys. Rev. Lett.*, 105:167404, Oct 2010.

[71] S. M. Hayden, H. A. Mook, Pengcheng Dai, T. G. Perring, and F. Doğan. The structure of the high-energy spin excitations in a high-transition-temperature superconductor. *Nature*, 429(6991):531–534, 2004.

[72] Meiyu He, Trinanjan Datta, and Dao-Xin Yao. $k$-edge and $L_3$-edge rixs study of columnar and staggered quantum dimer phases of the square lattice heisenberg model. *Phys. Rev. B*, 101:024426, Jan 2020.

[73] J. P. Hill, G. Blumberg, Young-June Kim, D. S. Ellis, S. Wakimoto, R. J. Birgeneau, Seiki Komiya, Yoichi Ando, B. Liang, R. L. Greene, D. Casa, and T. Gog. Observation of a 500

mev collective mode in $La_{2-x}Sr_xCuO_4$ and $Nd_2CuO_4$ using resonant inelastic x-ray scattering. *Phys. Rev. Lett.*, 100:097001, Mar 2008.

[74] H. Hosono, K. Tanabe, E. Takayama-Muromachi, H. Kageyama, S. Yamanaka, H. Kumakura, and S. Fujitsu. Exploration of new superconductors and functional materials, and fabrication of superconducting tapes and wires of iron pnictides. *Science and Technology of Advanced Materials*, 16(3), 2015.

[75] Rui-Zhen Huang, Da-Chuan Lu, Yi-Zhuang You, Zi Yang Meng, and Tao Xiang. Emergent symmetry and conserved current at a one-dimensional incarnation of deconfined quantum critical point. *Phys. Rev. B*, 100:125137, Sep 2019.

[76] Rui-Zhen Huang, Da-Chuan Lu, Yi-Zhuang You, Zi Yang Meng, and Tao Xiang. Emergent symmetry and conserved current at a one-dimensional incarnation of deconfined quantum critical point. *Phys. Rev. B*, 100:125137, Sep 2019.

[77] J Hubbard. Electron correlations in narrow energy bands. *Proc. Roy. Soc. (London), Ser. A*, Vol: 276, 11 1963.

[78] Harald Ibach and Douglas L Mills. *Electron energy loss spectroscopy and surface vibrations*. Academic press, 2013.

[79] E. D. Isaacs, P. M. Platzman, P. Metcalf, and J. M. Honig. Inelastic x-ray scattering study of the metal-antiferromagnetic insulator transition in $v_2o_3$. *Phys. Rev. Lett.*, 76:4211–4214, May 1996.

[80] Marcelo Jaime, Ramzy Daou, Scott A. Crooker, Franziska Weickert, Atsuko Uchida, Adrian E. Feiguin, Cristian D. Batista, Hanna A. Dabkowska, and Bruce D. Gaulin. Magnetostriction and magnetic texture to 100.75 Tesla in frustrated SrCu2(BO3)2. *Proceedings of the National Academy of Sciences*, 109(31):12404–12407, 2012.

[81] O. Janson, J. Richter, and H. Rosner. Modified kagome physics in the natural spin-$1/2$ kagome lattice systems: Kapellasite $Cu_3Zn(OH)_6Cl_2$ and haydeeite $Cu_3Mg(OH)_6Cl_2$. *Phys. Rev. Lett.*, 101:106403, Sep 2008.

[82] Chunjing Jia, Krzysztof Wohlfeld, Yao Wang, Brian Moritz, and Thomas P. Devereaux. Using rixs to uncover elementary charge and spin excitations. *Phys. Rev. X*, 6:021020, May 2016.

[83] Chunjing Jia, Krzysztof Wohlfeld, Yao Wang, Brian Moritz, and Thomas P. Devereaux. Using RIXS to Uncover Elementary Charge and Spin Excitations. *Physical Review X*, 6(2):021020, 2016.

[84] Shenghan Jiang and Olexei Motrunich. Ising ferromagnet to valence bond solid transition in a one-dimensional spin chain: Analogies to deconfined quantum critical points. *Phys. Rev. B*, 99:075103, Feb 2019.

[85] Junjiro Kanamori. Superexchange interaction and symmetry properties of electron orbitals. *Journal of Physics and Chemistry of Solids*, 10(2):87–98, 1959.

[86] M. A. Kastner, R. J. Birgeneau, G. Shirane, and Y. Endoh. Magnetic, transport, and optical properties of monolayer copper oxides. *Rev. Mod. Phys.*, 70:897–928, Jul 1998.

[87] B. Keimer, S. A. Kivelson, M. R. Norman, S. Uchida, and J. Zaanen. From quantum matter to high-temperature superconductivity in copper oxides. *Nature*, 518(7538):179–186, 2015.

[88] C. Kim, A. Y. Matsuura, Z.-X. Shen, N. Motoyama, H. Eisaki, S. Uchida, T. Tohyama, and S. Maekawa. Observation of spin-charge separation in one-dimensional $srcuo_2$. *Phys. Rev. Lett.*, 77:4054–4057, Nov 1996.

[89] Jungho Kim, D. Casa, Ayman Said, Rich Krakora, B. J. Kim, Elina Kasman, Xianrong Huang, and T. Gog. Quartz-based flat-crystal resonant inelastic x-ray scattering spectrometer with sub-10 mev energy resolution. *Scientific Reports*, 8(1):1958, Jan 2018.

[90] Jungho Kim, Xiangrong Huang, Thomas Toellner, and Ayman Said. Advances in hard X-ray RIXS toward meV resolution in the study of 5d transition metal materials. *Frontiers in Electronic Materials*, 4:1487856, 2024.

[91] K. v. Klitzing, G. Dorda, and M. Pepper. New method for high-accuracy determination of the fine-structure constant based on quantized hall resistance. *Phys. Rev. Lett.*, 45:494–497, Aug 1980.

[92] Tohru Koma. Spectral gap and decay of correlations in U(1)-symmetric lattice systems in dimensions D<2. *Journal of Mathematical Physics*, 48(2):023303, 02 2007.

[93] Deepu Kumar and Pradeep Kumar. Raman Spectroscopy, Advances and Applications. *Springer Series in Optical Sciences*, pages 17–51, 2024.

[94] Umesh Kumar and Shi-Zeng Lin. Inducing and controlling superconductivity in the hubbard honeycomb model using an electromagnetic drive. *Phys. Rev. B*, 103:064508, Feb 2021.

[95] Umesh Kumar, Abhishek Nag, Jiemin Li, H. C. Robarts, A. C. Walters, Mirian García-Fernández, R. Saint-Martin, A. Revcolevschi, Justine Schlappa, Thorsten Schmitt, Steven Johnston, and Ke-Jin Zhou. Unraveling higher-order contributions to spin excitations probed using resonant inelastic x-ray scattering. *Phys. Rev. B*, 106:L060406, Aug 2022.

[96] Umesh Kumar, Alberto Nocera, Gregory Price, Kenneth Stiwinter, Steven Johnston, and Trinanjan Datta. Spectroscopic signatures of next-nearest-neighbor hopping in the charge and spin dynamics of doped one-dimensional antiferromagnets. *Phys. Rev. B*, 102:075134, Aug 2020.

[97] B. Lake, D. A. Tennant, J.-S. Caux, T. Barthel, U. Schollwöck, S. E. Nagler, and C. D. Frost. Multispinon continua at zero and finite temperature in a near-ideal heisenberg chain. *Phys. Rev. Lett.*, 111:137205, Sep 2013.

[98] Cornelius Lanczos. An iteration method for the solution of the eigenvalue problem of linear differential and integral operators. *Journal of Research of the National Bureau of Standards*, 45(4):255–282, October 1950.

[99] Arthur Lavarélo and Guillaume Roux. Spinon excitation spectra of the J1-J2 chain from analytical calculations in the dimer basis and exact diagonalization. *The European Physical Journal B*, 87(10):229, 2014.

[100] J. M. Law, H. Luetkens, G. Pascua, Th. Hansen, R. Glaum, Z.-S. Wang, J. Wosnitza, and R. K. Kremer. Neutron diffraction, muon-spin rotation, and high magnetic field investigation of the multiferroic antiferromagnetic quantum spin-chain system cucro$_4$. *Phys. Rev. B*, 107:184442, May 2023.

[101] Patrick A. Lee, Naoto Nagaosa, and Xiao-Gang Wen. Doping a mott insulator: Physics of high-temperature superconductivity. *Rev. Mod. Phys.*, 78:17–85, Jan 2006.

[102] Junli Li, Jun-Qing Cheng, Trinanjan Datta, and Dao-Xin Yao. Resonant inelastic x-ray scattering spectra of spinon, doublon, and quarton excitations of a spin-$\frac{1}{2}$ antiferromagnetic heisenberg trimer chain. *Phys. Rev. B*, 111:024404, Jan 2025.

[103] Shaozhi Li, Alberto Nocera, Umesh Kumar, and Steven Johnston. Particle-hole asymmetry in the dynamical spin and charge responses of corner-shared 1d cuprates. *Communications Physics*, 4(1):217, Sep 2021.

[104] H. Lu, M. Rossi, A. Nag, M. Osada, D. F. Li, K. Lee, B. Y. Wang, M. Garcia-Fernandez, S. Agrestini, Z. X. Shen, E. M. Been, B. Moritz, T. P. Devereaux, J. Zaanen, H. Y. Hwang, Ke-Jin Zhou, and W. S. Lee. Magnetic excitations in infinite-layer nickelates. *Science*, 373(6551):213–216, 2021.

[105] Cheng Luo, Trinanjan Datta, and Dao-Xin Yao. Spectrum splitting of bimagnon excitations in a spatially frustrated heisenberg antiferromagnet revealed by resonant inelastic x-ray scattering. *Phys. Rev. B*, 89:165103, Apr 2014.

[106] Jin Luo, G. T. Trammell, and J. P. Hannon. Scattering operator for elastic and inelastic resonant x-ray scattering. *Phys. Rev. Lett.*, 71:287–290, Jul 1993.

[107] A. H. MacDonald, S. M. Girvin, and D. Yoshioka. $\frac{t}{U}$ expansion for the hubbard model. *Phys. Rev. B*, 37:9753–9756, Jun 1988.

[108] Pasquale Marra, Krzysztof Wohlfeld, and Jeroen van den Brink. Unraveling orbital correlations with magnetic resonant inelastic x-ray scattering. *Phys. Rev. Lett.*, 109:117401, Sep 2012.

[109] Miguel A Martín-Delgado. Real-space renormalization group methods applied to quantum lattice hamiltonians. In *Strongly Correlated Magnetic and Superconducting Systems: Proceedings of the El Escorial Summer School Held in Madrid, Spain, 15–19 July 1996*, pages 184–231. Springer, 2007.

[110] Miguel A. Martín-Delgado and Germán Sierra. Real space renormalization group methods and quantum groups. *Phys. Rev. Lett.*, 76:1146–1149, Feb 1996.

[111] Leonardo Martinelli, Davide Betto, Kurt Kummer, Riccardo Arpaia, Lucio Braicovich, Daniele Di Castro, Nicholas B. Brookes, Marco Moretti Sala, and Giacomo Ghiringhelli. Fractional spin excitations in the infinite-layer cuprate $CaCuO_2$. *Phys. Rev. X*, 12:021041, May 2022.

[112] Y. H. Matsuda, N. Abe, S. Takeyama, H. Kageyama, P. Corboz, A. Honecker, S. R. Manmana, G. R. Foltin, K. P. Schmidt, and F. Mila. Magnetization of $srcu_2(bo_3)_2$ in ultrahigh magnetic fields up to 118 t. *Phys. Rev. Lett.*, 111:137204, Sep 2013.

[113] N. D. Mermin and H. Wagner. Absence of ferromagnetism or antiferromagnetism in one- or two-dimensional isotropic heisenberg models. *Phys. Rev. Lett.*, 17:1133–1136, Nov 1966.

[114] M. Mitrano, S. Johnston, Young-June Kim, and M. P. M. Dean. Exploring quantum materials with resonant inelastic x-ray scattering. *Phys. Rev. X*, 14:040501, Dec 2024.

[115] M. Mitrano, S. Johnston, Young-June Kim, and M. P. M. Dean. Exploring quantum materials with resonant inelastic x-ray scattering. *Phys. Rev. X*, 14:040501, Dec 2024.

[116] A. Mitrovic and M. Bocko. Josephson junctions with ferromagnetic barriers for digital superconducting electronics: A review. *Phys. Rev. Appl.*, 23:067001, Jun 2025.

[117] M Moretti Sala, V Bisogni, C Aruta, G Balestrino, H Berger, N B Brookes, G M de Luca, D Di Castro, M Grioni, M Guarise, P G Medaglia, F Miletto Granozio, M Minola, P Perna, M Radovic, M Salluzzo, T Schmitt, K J Zhou, L Braicovich, and G Ghiringhelli. Energy and symmetry of dd excitations in undoped layered cuprates measured by cu l3 resonant inelastic x-ray scattering. *New Journal of Physics*, 13(4):043026, apr 2011.

[118] Martin Mourigal, Mechthild Enderle, Axel Klöpperpieper, Jean-Sébastien Caux, Anne Stunault, and Henrik M. Rønnow. Fractional spinon excitations in the quantum heisenberg antiferromagnetic chain. *Nature Physics*, 9(7):435–441, Jul 2013.

[119] Christopher Mudry, Akira Furusaki, Takahiro Morimoto, and Toshiya Hikihara. Quantum phase transitions beyond landau-ginzburg theory in one-dimensional space revisited. *Phys. Rev. B*, 99:205153, May 2019.

[120] A. Nocera, U. Kumar, N. Kaushal, G. Alvarez, E. Dagotto, and S. Johnston. Computing resonant inelastic x-ray scattering spectra using the density matrix renormalization group method. *Scientific Reports*, 8(1):11080, Jul 2018.

[121] M. R. Norman, H. Ding, M. Randeria, J. C. Campuzano, T. Yokoya, T. Takeuchi, T. Takahashi, T. Mochiku, K. Kadowaki, P. Guptasarma, and D. G. Hinks. Destruction of the fermi surface in underdoped high-tc superconductors. *Nature*, 392(6672):157–160, March 1998.

[122] S. Notbohm, P. Ribeiro, B. Lake, D. A. Tennant, K. P. Schmidt, G. S. Uhrig, C. Hess, R. Klingeler, G. Behr, B. Büchner, M. Reehuis, R. I. Bewley, C. D. Frost, P. Manuel, and R. S. Eccleston. One- and two-triplon spectra of a cuprate ladder. *Phys. Rev. Lett.*, 98:027403, Jan 2007.

[123] Masaki Oshikawa, Masanori Yamanaka, and Ian Affleck. Magnetization plateaus in spin chains: “haldane gap” for half-integer spins. *Phys. Rev. Lett.*, 78:1984–1987, Mar 1997.

[124] Subhajyoti Pal. ED_t-J: Exact diagonalization for the $t$-$j$ model. `https://github.com/sjp95/ED_t-J`, 2025. Accessed: 2025-08-14.

[125] Subhajyoti Pal, Umesh Kumar, Prabhakar, and Anamitra Mukherjee. Theoretical analysis of multimagnon excitations in resonant inelastic x-ray scattering spectra of two-dimensional antiferromagnets. *Phys. Rev. B*, 108:214405, Dec 2023.

[126] Subhajyoti Pal, Pradeep Thakur, Ashis Kumar Nandy, and Anamitra Mukherjee. Emergent quasiparticles & field-tuned rixs spectra in a trimerized spin-1/2 chain, 2025.

[127] E. Pavarini, I. Dasgupta, T. Saha-Dasgupta, O. Jepsen, and O. K. Andersen. Band-structure trend in hole-doped cuprates and correlation with $t_{c\max}$. *Phys. Rev. Lett.*, 87:047003, Jul 2001.

[128] Y. Y. Peng, G. Dellea, M. Minola, M. Conni, A. Amorese, D. Di Castro, G. M. De Luca, K. Kummer, M. Salluzzo, X. Sun, X. J. Zhou, G. Balestrino, M. Le Tacon, B. Keimer, L. Braicovich, N. B. Brookes, and G. Ghiringhelli. Influence of apical oxygen on the extent of in-plane exchange interaction in cuprate superconductors. *Nature Physics*, 13(12):1201–1206, 2017.

[129] Y. Y. Peng, G. Dellea, M. Minola, M. Conni, A. Amorese, D. Di Castro, G. M. De Luca, K. Kummer, M. Salluzzo, X. Sun, X. J. Zhou, G. Balestrino, M. Le Tacon, B. Keimer, L. Braicovich, N. B. Brookes, and G. Ghiringhelli. Influence of apical oxygen on the extent of in-plane exchange interaction in cuprate superconductors. *Nature Physics*, 13(12):1201–1206, Dec 2017.

[130] Y. Y. Peng, M. Salluzzo, X. Sun, A. Ponti, D. Betto, A. M. Ferretti, F. Fumagalli, K. Kummer, M. Le Tacon, X. J. Zhou, N. B. Brookes, L. Braicovich, and G. Ghiringhelli. Direct observation of charge order in underdoped and optimally doped $\mathrm{bi}_2(\mathrm{sr},\mathrm{la})_2\mathrm{cuo}_{6+\delta}$ by resonant inelastic x-ray scattering. *Phys. Rev. B*, 94:184511, Nov 2016.

[131] D. G. Pettifor and D. L. Weaire, editors. *The Recursion Method and Its Applications*, volume 58 of *Springer Series in Solid-State Sciences*. Springer, Berlin/Heidelberg, 1985.

[132] D. Pines. *Theory Of Quantum Liquids*. CRC Press, 1989.

[133] David Pines. *Elementary Excitations in Solids*. CRC Press, 1999.

[134] Michael Powalski, Kai P. Schmidt, and Götz S. Uhrig. Mutually attracting spin waves in the square-lattice quantum antiferromagnet. *SciPost Phys.*, 4:001, 2018.

[135] Prabhakar and Anamitra Mukherjee. *Journal of Physics A: Mathematical and Theoretical*, 56(38):385204, aug 2023.

[136] Prabhakar and Anamitra Mukherjee. *Phys. Rev. B*, 108:165103, Oct 2023.

[137] Prabhakar, Subhajyoti Pal, Umesh Kumar, Manoranjan Kumar, and Anamitra Mukherjee. Fractionalized excitations and resonant inelastic x-ray spectra in frustrated spin-1/2 trimer chains. *Phys. Rev. B*, 111:205106, May 2025.

[138] P. G. Radaelli, D. G. Hinks, A. W. Mitchell, B. A. Hunter, J. L. Wagner, B. Dabrowski, K. G. Vandervoort, H. K. Viswanathan, and J. D. Jorgensen. Structural and superconducting properties of $la_{2-x}sr_xcuo_4$ as a function of sr content. *Phys. Rev. B*, 49:4163–4175, Feb 1994.

[139] H. C. Robarts, M. García-Fernández, J. Li, A. Nag, A. C. Walters, N. E. Headings, S. M. Hayden, and Ke-Jin Zhou. Dynamical spin susceptibility in $la_2cuo_4$ studied by resonant inelastic x-ray scattering. *Phys. Rev. B*, 103:224427, Jun 2021.

[140] Brenden Roberts, Shenghan Jiang, and Olexei I. Motrunich. Deconfined quantum critical point in one dimension. *Phys. Rev. B*, 99:165143, Apr 2019.

[141] H. Rosner, H. Eschrig, R. Hayn, S.-L. Drechsler, and J. Málek. Electronic structure and magnetic properties of the linear chain cuprates $sr_2cuo_3$and $ca_2cuo_3$. *Phys. Rev. B*, 56:3402–3412, Aug 1997.

[142] Ch. Rüegg, N. Cavadini, A. Furrer, H.-U. Güdel, K. Krämer, H. Mutka, A. Wildes, K. Habicht, and P. Vorderwisch. Bose–Einstein condensation of the triplet states in the magnetic insulator TlCuCl3. *Nature*, 423(6935):62–65, 2003.

[143] D.J. Scalapino. The case for $dx2-y2$ pairing in the cuprate superconductors. *Physics Reports*, 250(6):329–365, 1995.

[144] A. Schilling, M. Cantoni, J. D. Guo, and H. R. Ott. Superconductivity above 130 k in the hg–ba–ca–cu–o system. *Nature*, 363(6424):56–58, 1993.

[145] J. Schlappa, U. Kumar, K. J. Zhou, S. Singh, M. Mourigal, V. N. Strocov, A. Revcolevschi, L. Patthey, H. M. Rønnow, S. Johnston, and T. Schmitt. Probing multi-spinon excitations outside of the two-spinon continuum in the antiferromagnetic spin chain cuprate sr2cuo3. *Nature Communications*, 9(1):5394, Dec 2018.

[146] J. Schlappa, T. Schmitt, F. Vernay, V. N. Strocov, V. Ilakovac, B. Thielemann, H. M. Rønnow, S. Vanishri, A. Piazzalunga, X. Wang, L. Braicovich, G. Ghiringhelli, C. Marin,

J. Mesot, B. Delley, and L. Patthey. Collective magnetic excitations in the spin ladder $Sr_{14}Cu_{24}O_{41}$ measured using high-resolution resonant inelastic x-ray scattering. *Phys. Rev. Lett.*, 103:047401, Jul 2009.

[147] J. Schlappa, K. Wohlfeld, K. J. Zhou, M. Mourigal, M. W. Haverkort, V. N. Strocov, L. Hozoi, C. Monney, S. Nishimoto, S. Singh, A. Revcolevschi, J.-S. Caux, L. Patthey, H. M. Rønnow, J. van den Brink, and T. Schmitt. Spin–orbital separation in the quasi-one-dimensional mott insulator sr2cuo3. *Nature*, 485(7396):82–85, 2012.

[148] Kai P. Schmidt and Götz S. Uhrig. Excitations in one-dimensional $s = \frac{1}{2}$ quantum antiferromagnets. *Phys. Rev. Lett.*, 90:227204, Jun 2003.

[149] Gary Schmiedinghoff, Leanna Müller, Umesh Kumar, Götz S. Uhrig, and Benedikt Fauseweh. Three-body bound states in antiferromagnetic spin ladders. *Communications Physics*, 5(1):218, Sep 2022.

[150] W. Schuelke. *Electron Dynamics by Inelastic X-Ray Scattering*. Oxford University Press, 2007.

[151] T. Senthil, Ashvin Vishwanath, Leon Balents, Subir Sachdev, and Matthew P. A. Fisher. Deconfined Quantum Critical Points. *Science*, 303(5663):1490–1494, 2004.

[152] Hui Shao, Yan Qi Qin, Sylvain Capponi, Stefano Chesi, Zi Yang Meng, and Anders W. Sandvik. Nearly deconfined spinon excitations in the square-lattice spin-$1/2$ heisenberg antiferromagnet. *Phys. Rev. X*, 7:041072, Dec 2017.

[153] G. L. Squires. *Introduction to the Theory of Thermal Neutron Scattering*. Cambridge University Press, 3 edition, 2012.

[154] Takanori Sugimoto and Takami Tohyama. Quasi-fractionalization of edge spin in chirality-assisted cluster-based Haldane state on triangular spin tube. *Communications Physics*, 6(1):291, 2023.

[155] Takanori Sugimoto and Takami Tohyama. Quasi-fractionalization of edge spin in chirality-assisted cluster-based haldane state on triangular spin tube. *Communications Physics*, 6(1):291, 2023.

[156] W. Tabis, Y. Li, M. Le Tacon, L. Braicovich, A. Kreyssig, M. Minola, G. Dellea, E. Weschke, M. J. Veit, M. Ramazanoglu, A. I. Goldman, T. Schmitt, G. Ghiringhelli, N. Barišić, M. K. Chan, C. J. Dorow, G. Yu, X. Zhao, B. Keimer, and M. Greven. Charge order and its connection with fermi-liquid charge transport in a pristine high-tc cuprate. *Nature Communications*, 5(1):5875, 2014.

[157] So Takei and Yaroslav Tserkovnyak. Detecting fractionalization in critical spin liquids using color centers. *Phys. Rev. Res.*, 6:013043, Jan 2024.

[158] Tom Timusk and Bryan Statt. The pseudogap in high-temperature superconductors: an experimental survey. *Reports on Progress in Physics*, 62(1):61, jan 1999.

[159] Tom Timusk and Bryan Statt. The pseudogap in high-temperature superconductors: an experimental survey. *Reports on Progress in Physics*, 62(1):61, jan 1999.

[160] J. M. Tranquada, B. J. Sternlieb, J. D. Axe, Y. Nakamura, and S. Uchida. Evidence for stripe correlations of spins and holes in copper oxide superconductors. *Nature*, 375(6532):561–563, 1995.

[161] K. Tsutsui, T. Tohyama, and S. Maekawa. Momentum dependence of resonant inelastic x-ray scattering spectrum in insulating cuprates. *Phys. Rev. Lett.*, 83:3705–3708, Nov 1999.

[162] D. Vaknin, S. K. Sinha, D. E. Moncton, D. C. Johnston, J. M. Newsam, C. R. Safinya, and H. E. King. Antiferromagnetism in $\mathrm{la_2cuo_{4-y}}$. *Phys. Rev. Lett.*, 58:2802–2805, Jun 1987.

[163] J. van den Brink and M. van Veenendaal. Correlation functions measured by indirect resonant inelastic x-ray scattering. *Europhysics Letters*, 73(1):121, dec 2005.

[164] Michel van Veenendaal. Polarization dependence of $l$- and $m$-edge resonant inelastic x-ray scattering in transition-metal compounds. *Phys. Rev. Lett.*, 96:117404, Mar 2006.

[165] C. M. Varma, P. B. Littlewood, S. Schmitt-Rink, E. Abrahams, and A. E. Ruckenstein. Phenomenology of the normal state of cu-o high-temperature superconductors. *Phys. Rev. Lett.*, 63:1996–1999, Oct 1989.

[166] F. H. Vernay, M. J. P. Gingras, and T. P. Devereaux. Momentum-dependent light scattering in insulating cuprates. *Phys. Rev. B*, 75:020403, Jan 2007.

[167] G. Vidal. Classical simulation of infinite-size quantum lattice systems in one spatial dimension. *Phys. Rev. Lett.*, 98:070201, Feb 2007.

[168] Guifré Vidal. Efficient classical simulation of slightly entangled quantum computations. *Phys. Rev. Lett.*, 91:147902, Oct 2003.

[169] Guifré Vidal. Efficient simulation of one-dimensional quantum many-body systems. *Phys. Rev. Lett.*, 93:040502, Jul 2004.

[170] Sean Vig, Anshul Kogar, Matteo Mitrano, Ali A. Husain, Vivek Mishra, Melinda S. Rak, Luc Venema, Peter D. Johnson, Genda D. Gu, Eduardo Fradkin, Michael R. Norman, and Peter Abbamonte. Measurement of the dynamic charge response of materials using low-energy, momentum-resolved electron energy-loss spectroscopy (M-EELS). *SciPost Phys.*, 3:026, 2017.

[171] B. Vignolle, S. M. Hayden, D. F. McMorrow, H. M. Rønnow, B. Lake, C. D. Frost, and T. G. Perring. Two energy scales in the spin excitations of the high-temperature superconductor la2−xsrxcuo4. *Nature Physics*, 3(3):163–167, 2007.

[172] S. Wakimoto, K. Ishii, H. Kimura, M. Fujita, G. Dellea, K. Kummer, L. Braicovich, G. Ghiringhelli, L. M. Debeer-Schmitt, and G. E. Granroth. High-energy magnetic excitations in

overdoped la$_{2-x}$sr$_x$cuo$_4$ studied by neutron and resonant inelastic x-ray scattering. *Phys. Rev. B*, 91:184513, May 2015.

[173] Xiangang Wan, Thomas A. Maier, and Sergej Y. Savrasov. Calculated magnetic exchange interactions in high-temperature superconductors. *Phys. Rev. B*, 79:155114, Apr 2009.

[174] Yuan Wan and N. P. Armitage. Resolving continua of fractional excitations by spinon echo in thz 2d coherent spectroscopy. *Phys. Rev. Lett.*, 122:257401, Jun 2019.

[175] Steven R. White. Density matrix formulation for quantum renormalization groups. *Phys. Rev. Lett.*, 69:2863–2866, Nov 1992.

[176] Steven R. White. Density-matrix algorithms for quantum renormalization groups. *Phys. Rev. B*, 48:10345–10356, Oct 1993.

[177] M. Windt, M. Grüninger, T. Nunner, C. Knetter, K. P. Schmidt, G. S. Uhrig, T. Kopp, A. Freimuth, U. Ammerahl, B. Büchner, and A. Revcolevschi. Observation of two-magnon bound states in the two-leg ladders of $(ca, la)_{14}$cu$_{24}O_{41}$. *Phys. Rev. Lett.*, 87:127002, Aug 2001.

[178] M. K. Wu, J. R. Ashburn, C. J. Torng, P. H. Hor, R. L. Meng, L. Gao, Z. J. Huang, Y. Q. Wang, and C. W. Chu. Superconductivity at 93 k in a new mixed-phase y-ba-cu-o compound system at ambient pressure. *Phys. Rev. Lett.*, 58:908–910, Mar 1987.

[179] Tao Wu, Hadrien Mayaffre, Steffen Krämer, Mladen Horvatić, Claude Berthier, W. N. Hardy, Ruixing Liang, D. A. Bonn, and Marc-Henri Julien. Magnetic-field-induced charge-stripe order in the high-temperature superconductor yba2cu3oy. *Nature*, 477(7363):191–194, 2011.

[180] Tao Wu, Hadrien Mayaffre, Steffen Krämer, Mladen Horvatić, Claude Berthier, Philip L. Kuhns, Arneil P. Reyes, Ruixing Liang, W. N. Hardy, D. A. Bonn, and Marc-Henri Julien.

Emergence of charge order from the vortex state of a high-temperature superconductor. *Nature Communications*, 4(1):2113, 2013.

[181] K. Yamada, C. H. Lee, K. Kurahashi, J. Wada, S. Wakimoto, S. Ueki, H. Kimura, Y. Endoh, S. Hosoya, G. Shirane, R. J. Birgeneau, M. Greven, M. A. Kastner, and Y. J. Kim. Doping dependence of the spatially modulated dynamical spin correlations and the superconducting-transition temperature in $\mathrm{la}_{2-x}\mathrm{sr}_x\mathrm{cuo}_4$. *Phys. Rev. B*, 57:6165–6172, Mar 1998.

[182] Ayako Yamamoto, Nao Takeshita, Chieko Terakura, and Yoshinori Tokura. High pressure effects revisited for the cuprate superconductor family with highest critical temperature. *Nature Communications*, 6(1):8990, Dec 2015.

[183] Shun-Li Yu, Wei Wang, Zhao-Yang Dong, Zi-Jian Yao, and Jian-Xin Li. Deconfinement of spinons in frustrated spin systems: Spectral perspective. *Phys. Rev. B*, 98:134410, Oct 2018.

[184] J. Zaanen, G. A. Sawatzky, and J. W. Allen. Band gaps and electronic structure of transition-metal compounds. *Phys. Rev. Lett.*, 55:418–421, Jul 1985.

[185] Jan Zaanen and Andrzej M. Oleś. Canonical perturbation theory and the two-band model for high-$T_c$ superconductors. *Phys. Rev. B*, 37:9423–9438, Jun 1988.

[186] Carolyn Zhang and Michael Levin. Exactly solvable model for a deconfined quantum critical point in 1d. *Phys. Rev. Lett.*, 130:026801, Jan 2023.

[187] F. C. Zhang and T. M. Rice. Effective hamiltonian for the superconducting cu oxides. *Phys. Rev. B*, 37:3759–3761, Mar 1988.

[188] F. C. Zhang and T. M. Rice. Validity of the t-j model. *Phys. Rev. B*, 41:7243–7246, Apr 1990.

# Appendix A

## A.1 Derivation of the UCL approximation for RIXS at the Cu $L$-edge

The Ultra-Covalent Limit (UCL) approximation for Resonant Inelastic X-ray Scattering (RIXS) at the Cu $L$-edge is valid when the energy differences between the intermediate state's eigenstates are much smaller than the inverse core-hole lifetime, $\Gamma$. We begin with the spectral decomposition of the RIXS given in Eq.3.2:

$$\frac{1}{\omega_{in} - \mathcal{H} + i\Gamma} = \sum_{|N\rangle} |N\rangle\langle N| \frac{1}{\omega_{in} - \mathcal{E}_N + i\Gamma}, \tag{A.1}$$

where $\{|N\rangle\}$ are eigenstates of $\mathcal{H}$ with energy $\{\mathcal{E}_N\}$.

We focus on the RIXS process at the resonant Cu $L$-edge, corresponding to transitions between the initial configuration $2p^0 3d^{*1}$ and the intermediate configuration $2p^1 3d^{*0}$, where all operators are expressed in the hole representation. In this case, the intermediate states $|N\rangle$ that contribute to the scattering amplitude must exclude configurations where the $d$-orbital on the core-hole site $\mathbf{j}$ is occupied by a hole. This restriction is enforced by introducing a projection operator $\tilde{P}_{\mathbf{j}}$, so that the intermediate-state propagator can be rewritten as

$$\sum_{|N\rangle} |N\rangle\langle N| \frac{1}{\omega_{in} - \mathcal{E}_N + i\Gamma} \longrightarrow \sum_{|N\rangle} \tilde{P}_{\mathbf{j}} |N\rangle\langle N| \tilde{P}_{\mathbf{j}} \frac{1}{\omega_{in} - \mathcal{E}_N + i\Gamma}. \tag{A.2}$$

To proceed, we split the total Hamiltonian into two commuting parts:

$$\bar{H} = H + U_c \sum_{\mathbf{i},\alpha,\sigma,\sigma'} n^d_{\mathbf{i}\sigma}\, n^p_{\mathbf{i}\alpha\sigma'}, \tag{A.3}$$

$$\bar{H}_c = H_c - U_c \sum_{\mathbf{i},\alpha,\sigma,\sigma'} n^d_{\mathbf{i}\sigma}\, n^p_{\mathbf{i}\alpha\sigma'}. \tag{A.4}$$

Here, $\bar{H}$ acts purely within the valence sector, while $\bar{H}_c$ governs the core-hole degrees of freedom. The commutativity of $\bar{H}$ and $\bar{H}_c$ follows from the fact that, due to the projection $\tilde{P}_{\mathbf{j}}$, the intermediate states always contain a hole in either the $2p$ shell or the $3d$ shell, but never both on the same site.

The eigenstates of the total Hamiltonian can then be written as product states

$$|N\rangle = |n\rangle \otimes |n_c\rangle, \tag{A.5}$$

$$\mathcal{E}_N = \varepsilon_n + \varepsilon_{n_c}, \tag{A.6}$$

where $|n\rangle$ is an eigenstate of $\bar{H}$ with energy $\varepsilon_n$ and $|n_c\rangle$ is an eigenstate of $\bar{H}_c$ with energy $\varepsilon_{n_c}$.

Substituting this into the intermediate-state propagator gives

$$\frac{1}{\omega_{in} - \mathcal{H} + i\Gamma} = \sum_{|n\rangle,\,|n_c\rangle} \tilde{P}_{\mathbf{j}}\,|n\rangle\langle n|\,n_c\rangle\langle n_c|\,\tilde{P}_{\mathbf{j}} \frac{1}{\omega_{in} - \varepsilon_n - \varepsilon_{n_c} + i\Gamma}. \tag{A.7}$$

For a single hole in the $p$-shell, $\bar{H}_c$ has only two eigenstates:

$$|L_2\rangle, \quad |L_3\rangle, \tag{A.8}$$

corresponding to the $j = 1/2$ and $j = 3/2$ angular momentum states, split by the spin–orbit interaction $\lambda$. Their energies are $\varepsilon_{L_2}$ and $\varepsilon_{L_3}$, respectively. (Here, $j$ denotes total angular momentum, while $\mathbf{j}$ labels the lattice site.)

The propagator, therefore, separates into two distinct contributions:

$$\begin{aligned}\frac{1}{\omega_{in} - \mathcal{H} + i\Gamma} =& \sum_{|n\rangle} \tilde{P}_{\mathbf{j}}\,|n\rangle\langle n|L_2\rangle\langle L_2|\,\tilde{P}_{\mathbf{j}} \frac{1}{\omega_{in} - \varepsilon_n - \varepsilon_{L_2} + i\Gamma} \\ &+ \sum_{|n\rangle} \tilde{P}_{\mathbf{j}}\,|n\rangle\langle n|L_3\rangle\langle L_3|\,\tilde{P}_{\mathbf{j}} \frac{1}{\omega_{in} - \varepsilon_n - \varepsilon_{L_3} + i\Gamma}.\end{aligned} \tag{A.9}$$

**Resonance approximation:**

We consider the case where the incident x-ray photons are tuned to the $L_3$ resonance, such that $\omega_i \simeq \varepsilon_{L_3}$. In the cuprates, the spin–orbit coupling $\lambda$ is much larger than both the core-hole lifetime broadening $\Gamma$ and the relevant valence excitation energies $\varepsilon_n$ ($\lambda \gg \Gamma$ and $\varepsilon_n \ll \lambda$). Under these conditions, the $L_2$ contribution to the intermediate-state propagator is strongly suppressed and can be neglected[82]. The resolvent operator therefore reduces to

$$\frac{1}{\omega_{in} - \mathcal{H} + i\Gamma} = \sum_{|n\rangle} \tilde{P}_{\mathbf{j}} |n\rangle\langle n|L_3\rangle\langle L_3|\tilde{P}_{\mathbf{j}} \frac{1}{-\varepsilon_n + i\Gamma}. \tag{A.10}$$

**UCL expansion:**

To proceed, we employ the ultra-short core-hole lifetime (UCL) expansion [7, 125, 55, 163, 44], which is appropriate for Cu $L$-edge RIXS in the regime $4t/\Gamma \ll 1$. Expanding the resolvent in powers of $\bar{H}/\Gamma$ yields

$$\frac{1}{\omega_{in} - \mathcal{H} + i\Gamma} = \tilde{P}_{\mathbf{j}} |L_3\rangle\langle L_3| \sum_{l=0}^{\infty} \frac{\bar{H}^l}{(i\Gamma)^{l+1}} \tilde{P}_{\mathbf{j}}. \tag{A.11}$$

This form allows the local RIXS scattering operator to be expressed as

$$O_{\mathbf{j},\mathbf{e}} = \frac{1}{i\Gamma} D^{\dagger}_{\mathbf{j},\mathbf{e}^f} \tilde{P}_{\mathbf{j}} |L_3\rangle\langle L_3| \sum_{l=0}^{\infty} \frac{\bar{H}^l}{(i\Gamma)^l} \tilde{P}_{\mathbf{j}} D_{\mathbf{j},\mathbf{e}^i}, \tag{A.12}$$

where $D_{\mathbf{j},\mathbf{e}^i}$ and $D_{\mathbf{j},\mathbf{e}^f}$ are the dipole operators associated with the incident and scattered photon polarizations.

**Second-order UCL approximation:**

Truncating the expansion to the first two terms ($l = 0$ and $l = 1$) leads to the second-order UCL approximation. In this case, the RIXS operator separates into two contributions:

$$O_{\mathbf{j},\mathbf{e}} = O^{(1)}_{\mathbf{j},\mathbf{e}} + O^{(2)}_{\mathbf{j},\mathbf{e}}, \tag{A.13}$$

$$O^{(1)}_{\mathbf{j},\mathbf{e}} = \frac{1}{i\Gamma} D^{\dagger}_{\mathbf{j},\mathbf{e}^f} \tilde{P}_{\mathbf{j}} |L_3\rangle\langle L_3| \tilde{P}_{\mathbf{j}} D_{\mathbf{j},\mathbf{e}^i}, \tag{A.14}$$

$$O^{(2)}_{\mathbf{j},\mathbf{e}} = \frac{1}{(i\Gamma)^2} D^{\dagger}_{\mathbf{j},\mathbf{e}^f} \tilde{P}_{\mathbf{j}} |L_3\rangle\langle L_3| \bar{H} \tilde{P}_{\mathbf{j}} D_{\mathbf{j},\mathbf{e}^i}. \tag{A.15}$$

The applicability and limitations of this approximation are discussed in detail in the main text.

### A.1.1 Change of Projection Operators

It is often convenient to introduce an alternative projection operator, denoted as $P_{\mathbf{j}}$, which projects onto the subspace with no double occupancy in the $d$-orbital at site **j**. This is precisely the site where the core hole is created. With this definition, one finds the useful identity:

$$\tilde{P}_{\mathbf{j}} D_{\mathbf{j},\mathbf{e}^i} = D_{\mathbf{j},\mathbf{e}^i} P_{\mathbf{j}}, \tag{A.16}$$

Where $D_{\mathbf{j},\mathbf{e}^i}$ is the dipole operator. A similar relation holds for the Hermitian conjugate operator $D^\dagger_{\mathbf{j},\mathbf{e}^f}$.

### A.1.2 The $l = 1$ Term

We now consider the term

$$P_{\mathbf{j}} D^\dagger_{\mathbf{j},\mathbf{e}^f} |L_3\rangle\langle L_3|\, \bar{H}\, D_{\mathbf{j},\mathbf{e}^i} P_{\mathbf{j}} |i\rangle. \tag{A.17}$$

To proceed, note that

$$P_{\mathbf{j}} D^\dagger_{\mathbf{j},\mathbf{e}^f} |L_3\rangle\langle L_3|\, \bar{H}_{\mathbf{mj}}\, D_{\mathbf{j},\mathbf{e}^i} P_{\mathbf{j}} |i\rangle = 0, \tag{A.18}$$

where

$$\begin{aligned} \bar{H}_{\mathbf{mj}} = &-t \sum_{m(j),\sigma} \left(d^\dagger_{\mathbf{m}\sigma} d_{\mathbf{j}\sigma} + \text{h.c.}\right) - t' \sum_{\mathbf{m}'(\mathbf{j}),\sigma} \left(d^\dagger_{\mathbf{m}'\sigma} d_{\mathbf{j}\sigma} + \text{h.c.}\right) \\ &+ U_c \sum_{\alpha\sigma\sigma'} n^d_{\mathbf{j}\sigma} n^p_{\mathbf{j}\alpha\sigma'} + U n^d_{\mathbf{j}\uparrow} n^d_{\mathbf{j}\downarrow}. \end{aligned} \tag{A.19}$$

This vanishing occurs because any Hamiltonian term containing site **j** will give zero when sandwiched between the dipole operators $D$ and the initial state $|i\rangle$. Here, $\mathbf{m}(\mathbf{j})$ and $\mathbf{m}'(\mathbf{j})$ denote the nearest and next-nearest neighbors of site **j**, respectively.

Thus, we can write:

$$\begin{aligned} &P_{\mathbf{j}} D^\dagger_{\mathbf{j},\mathbf{e}^f} |L_3\rangle\langle L_3|\, \bar{H}\, D_{\mathbf{j},\mathbf{e}^i} P_{\mathbf{j}} |i\rangle \\ &= P_{\mathbf{j}} D^\dagger_{\mathbf{j},\mathbf{e}^f} |L_3\rangle\langle L_3| \left(\bar{H} - \bar{H}_{\mathbf{mj}}\right) D_{\mathbf{j},\mathbf{e}^i} P_{\mathbf{j}} |i\rangle. \end{aligned} \tag{A.20}$$

Because $\bar{H} - \bar{H}_{\mathbf{mj}}$ contains no operators acting on the site $\mathbf{j}$, it can be commuted with $D_{\mathbf{j},\mathbf{e}^i}$ and $P_{\mathbf{j}}$, giving:

$$\begin{aligned} & P_{\mathbf{j}} D^{\dagger}_{\mathbf{j},\mathbf{e}^f} |L_3\rangle\langle L_3| \, \bar{H} \, D_{\mathbf{j},\mathbf{e}^i} P_{\mathbf{j}} |i\rangle \\ & = P_{\mathbf{j}} D^{\dagger}_{\mathbf{j},\mathbf{e}^f} |L_3\rangle\langle L_3| D_{\mathbf{j},\mathbf{e}^i} P_{\mathbf{j}} \left( \bar{H} - \bar{H}_{\mathbf{mj}} \right) |i\rangle. \end{aligned} \tag{A.21}$$

Since $\bar{H}|i\rangle = H|i\rangle = E_i|i\rangle = 0$ (with the energy zero set accordingly), we are left with:

$$P_{\mathbf{j}} D^{\dagger}_{\mathbf{j},\mathbf{e}^f} |L_3\rangle\langle L_3| D_{\mathbf{j},\mathbf{e}^i} P_{\mathbf{j}} \, \bar{H}_{\mathbf{mj}} |i\rangle. \tag{A.22}$$

However, due to the projection $P_{\mathbf{j}}$, both $U$ and $U_c$ terms do not contribute, and terms like $P_{\mathbf{j}} D^{\dagger}_{\mathbf{j},\mathbf{e}^f} |L_3\rangle\langle L_3| D_{\mathbf{j},\mathbf{e}^i} P_{\mathbf{j}} d^{\dagger}_{\mathbf{l}\sigma} d_{\mathbf{j}\sigma} |i\rangle$ vanish for any $\mathbf{l} = \mathbf{m}$ or $\mathbf{m}'$. We then obtain:

$$\begin{aligned} & P_{\mathbf{j}} D^{\dagger}_{\mathbf{j},\mathbf{e}^f} |L_3\rangle\langle L_3| \, \bar{H} \, D_{\mathbf{j},\mathbf{e}^i} P_{\mathbf{j}} |i\rangle \\ & = -P_{\mathbf{j}} D^{\dagger}_{\mathbf{j},\mathbf{e}^f} |L_3\rangle\langle L_3| D_{\mathbf{j},\mathbf{e}^i} \\ & \quad \times \left[ -t \sum_{\mathbf{m}(\mathbf{j}),\sigma} d^{\dagger}_{\mathbf{j}\sigma} d_{\mathbf{m}\sigma} - t' \sum_{\mathbf{m}'(\mathbf{j}),\sigma} d^{\dagger}_{\mathbf{j}\sigma} d_{\mathbf{m}\sigma} \right] P_{\mathbf{j}} |i\rangle. \end{aligned} \tag{A.23}$$

The asymmetry here, i.e., the absence of Hermitian conjugate terms $\propto d^{\dagger}_{\mathbf{m}\sigma} d_{\mathbf{j}\sigma}$, reflects that in RIXS we are sensitive only to sites hosting $3d$ holes.

### A.1.3 Local RIXS Matrix Elements

Defining the local matrix elements of RIXS for the scattering geomatry given in the Section A.1.4 below as

$$P_{\mathbf{j}} D^{\dagger}_{\mathbf{j},\mathbf{e}^f} |L_3\rangle\langle L_3| D_{\mathbf{j},\mathbf{e}^i} P_{\mathbf{j}} \equiv \mathcal{M}_{\mathbf{e}} P_{\mathbf{j}} n_{\mathbf{j}} P_{\mathbf{j}} + \tilde{\mathcal{M}}_{\mathbf{e}} P_{\mathbf{j}} S^z_{\mathbf{j}} P_{\mathbf{j}}, \tag{A.24}$$

the local RIXS form factors from Ref. [108] are:

$$\begin{aligned} \mathcal{M}_{\pi\text{–}\sigma} &= -i \frac{2}{3} \left( \mathbf{e}^i_y \mathbf{e}^f_x - \mathbf{e}^i_x \mathbf{e}^f_y \right), \\ \mathcal{M}_{\pi\text{–}\pi} &= -\frac{2}{3} \left( \mathbf{e}^i_x \mathbf{e}^f_x + \mathbf{e}^i_y \mathbf{e}^f_y \right). \end{aligned} \tag{A.25}$$

A short derivation of atomic form factor is given in the section A.1.4 below. With $P_{\mathbf{j}} n_{\mathbf{j}} P_{\mathbf{j}} = \tilde{n}_{\mathbf{j}}$ and $P_{\mathbf{j}} S^z_{\mathbf{j}} P_{\mathbf{j}} = S^z_{\mathbf{j}}$, where $\tilde{n}_{\mathbf{j}} = \sum_\sigma \tilde{d}^\dagger_{\mathbf{j}\sigma}\tilde{d}_{\mathbf{j}\sigma}$ and $\tilde{d}^\dagger_{\mathbf{j}\sigma} = d^\dagger_{\mathbf{j}\sigma}(1 - n_{\mathbf{j},-\sigma})$, the RIXS operators in the UCL approximation are:

$$\begin{aligned} O^{(0)}_{\mathbf{j},\mathbf{e}} &= \frac{1}{\Gamma}\mathcal{M}_{\mathbf{e}}\tilde{n}_{\mathbf{j}} + \frac{1}{\Gamma}\tilde{\mathcal{M}}_{\mathbf{e}} S^z_{\mathbf{j}}, \\ O^{(1)}_{\mathbf{j},\mathbf{e}} &= \frac{t}{i\Gamma^2}\mathcal{M}_{\mathbf{e}}\sum_{\mathbf{m}(\mathbf{j})}\tilde{d}^\dagger_{\mathbf{j}\sigma}d_{\mathbf{m}\sigma} + \frac{t}{i\Gamma^2}\tilde{\mathcal{M}}_{\mathbf{e}} S^z_{\mathbf{j}}\sum_{\mathbf{m}(\mathbf{j})} d^\dagger_{\mathbf{j}\sigma}d_{\mathbf{m}\sigma} \\ &\quad + \frac{t'}{i\Gamma^2}\mathcal{M}_{\mathbf{e}}\sum_{\mathbf{m}'(\mathbf{j})}\tilde{d}^\dagger_{\mathbf{j}\sigma}d_{\mathbf{m}\sigma} + \frac{t'}{i\Gamma^2}\tilde{\mathcal{M}}_{\mathbf{e}} S^z_{\mathbf{j}}\sum_{\mathbf{m}'(\mathbf{j})} d^\dagger_{\mathbf{j}\sigma}d_{\mathbf{m}\sigma}. \end{aligned} \tag{A.26}$$

Substituting into Eq. (3.5) and Fourier transforming yields (NSC channel):

$$I^{\text{UCL}}_{\pi\text{–}\sigma}(\mathbf{q},\omega) = |\mathcal{M}_{\pi\text{–}\sigma}|^2\left\{\frac{1}{\Gamma^2}S^0(\mathbf{q},\omega) + \frac{1}{\Gamma^4}S^1(\mathbf{q},\omega)\right\}, \tag{A.27}$$

$$S^0(\mathbf{q},\omega) = \sum_f \left|\langle f|S^z_{\mathbf{q}}|i\rangle\right|^2 \delta(\omega + E_i - E_f), \tag{A.28}$$

$$\begin{aligned} S^1(\mathbf{q},\omega) = \frac{z^2t^2}{N^2}\sum_f &\left|\left\langle f\left|\sum_{\mathbf{k},\mathbf{k}'}\varepsilon_{-\mathbf{k}'+\mathbf{k}+\mathbf{q}}S^z_{\mathbf{k}'}\tilde{d}^\dagger_{\mathbf{k},\sigma}d_{-\mathbf{k}'+\mathbf{k}+\mathbf{q},\sigma}\right| i\right\rangle\right|^2 \\ &\times \delta(\omega + E_i - E_f), \end{aligned} \tag{A.29}$$

where $S^z_{\mathbf{q}} = \frac{1}{2\sqrt{N}}\sum_{\mathbf{k}}(d^\dagger_{\mathbf{k}\uparrow}d_{\mathbf{q}+\mathbf{k},\uparrow} - d^\dagger_{\mathbf{k}\downarrow}d_{\mathbf{q}+\mathbf{k},\downarrow})$, $z = 4$ for a 2D square lattice, and $\varepsilon_{\mathbf{k}} = \gamma_{\mathbf{k}} + (t'/t)\eta_{\mathbf{k}}$ with $\gamma_{\mathbf{k}} = (\cos k_x + \cos k_y)/2$ and $\eta_{\mathbf{k}} = \cos k_x \cos k_y$. The function $\varepsilon_{\mathbf{k}}$ has $A_{1g}$ symmetry.

Similarly, for the $\pi-\pi$ channel (SC channel):

$$I^{\text{UCL}}_{\pi\text{–}\pi}(\mathbf{q},\omega) = |\mathcal{M}_{\pi\text{–}\pi}|^2\left\{\frac{1}{\Gamma^2}\tilde{N}^0(\mathbf{q},\omega) + \frac{1}{\Gamma^4}\tilde{N}^1(\mathbf{q},\omega)\right\}, \tag{A.30}$$

$$\tilde{N}^0(\mathbf{q},\omega) = \sum_f |\langle f|\tilde{n}_{\mathbf{q}}|i\rangle|^2 \delta(\omega + E_i - E_f), \tag{A.31}$$

$$\begin{aligned} \tilde{N}^1(\mathbf{q},\omega) = \frac{z^2t^2}{N}\sum_f &\left|\left\langle f\left|\sum_{\mathbf{k}}\varepsilon_{\mathbf{q}+\mathbf{k}}\tilde{d}^\dagger_{\mathbf{k},\sigma}d_{\mathbf{q}+\mathbf{k},\sigma}\right| i\right\rangle\right|^2 \\ &\times \delta(\omega + E_i - E_f), \end{aligned} \tag{A.32}$$

where $\tilde{n}_{\mathbf{i}} = \sum_\sigma \tilde{d}^\dagger_{\mathbf{i}\sigma}\tilde{d}_{\mathbf{i}\sigma}$ is the constrained density operator, and $\tilde{d}^\dagger_{\mathbf{i}\sigma} = d^\dagger_{\mathbf{i}\sigma}(1-n_{\mathbf{i}\bar{\sigma}})$, $\tilde{d}_{\mathbf{i}\sigma} = (1-n_{\mathbf{i}\bar{\sigma}})d_{\mathbf{i}\sigma}$.

Because the first-order UCL terms are real while the second-order terms are imaginary, there is no interference between them. Consequently, the total RIXS cross section is simply the sum of the first- and second-order contributions. Importantly, within this truncation of the UCL expansion, the RIXS spectrum does not depend on the core-hole potential $U_c$; dependence on $U_c$ only appears in higher-order corrections [82].

### A.1.4 Polarization-Dependent RIXS Form Factor at the Cu $L_3$ Edge

The RIXS intensity can be written as

$$I_\epsilon(\mathbf{q},\omega) = |\mathcal{M}_\epsilon|^2 \sum_f \frac{1}{\sqrt{L}} \sum_j e^{i\mathbf{q}\cdot j} \left| \langle f | \tilde{D}_{\text{in},j}\, \tilde{\mathcal{O}}\, \tilde{D}_{\text{out},j} | g \rangle \right|^2 \delta(E_f - E_g - \omega), \tag{A.33}$$

where the polarization dependence enters through the *atomic form factor* $\mathcal{M}_\epsilon$. Let us redefine the Eq. A.24

$$\mathcal{W}_\epsilon = P_j D^\dagger_{j,\mathbf{e}^f} |L_3\rangle\langle L_3| D_{j,\mathbf{e}^i} P_j. \tag{A.34}$$

The operators $D_{j,\mathbf{e}^{i(f)}}$ describe dipole-allowed transitions between the $2p$ and $3d$ shells [70, 108]:

$$D_{j,\mathbf{e}} = \sum_{m_p, m_d, \sigma} \langle 3d, m_d | \mathbf{e}\cdot\mathbf{r} | 2p, m_p \rangle \, d^\dagger_{j,m_d,\sigma} p_{j,m_p,\sigma}. \tag{A.35}$$

At the Cu $L_3$-edge, the intermediate core state corresponds to the $2p_{3/2}$ configuration, whose total angular momentum $j = 3/2$ results from spin–orbit coupling in the $2p$ shell.

### A.1.5 Tensor Structure of the Atomic Form Factor

The local scattering amplitude can be expressed in Cartesian tensor form as

$$\mathcal{W}_\epsilon = \sum_{i,j} e^f_i \mathcal{M}_{ij} e^i_j, \tag{A.36}$$

where $\mathcal{M}_{ij}$ is the atomic form factor tensor and $\mathbf{e}^i$ ($\mathbf{e}^f$) incoming (outgoing) photon polarizations.

$$\mathcal{M}_{ij} = \sum_{m_j} \langle 3d \,|\, r_i \,|\, 2p_{3/2}, m_j \rangle \langle 2p_{3/2}, m_j \,|\, r_j \,|\, 3d \rangle. \tag{A.37}$$

For the Cu $L_3$-edge, this tensor can be decomposed as [70]

$$\mathcal{M}_{ij} = \mathcal{M}\, \delta_{ij} + \tilde{\mathcal{M}}\, i\epsilon_{ijk} S_k, \tag{A.38}$$

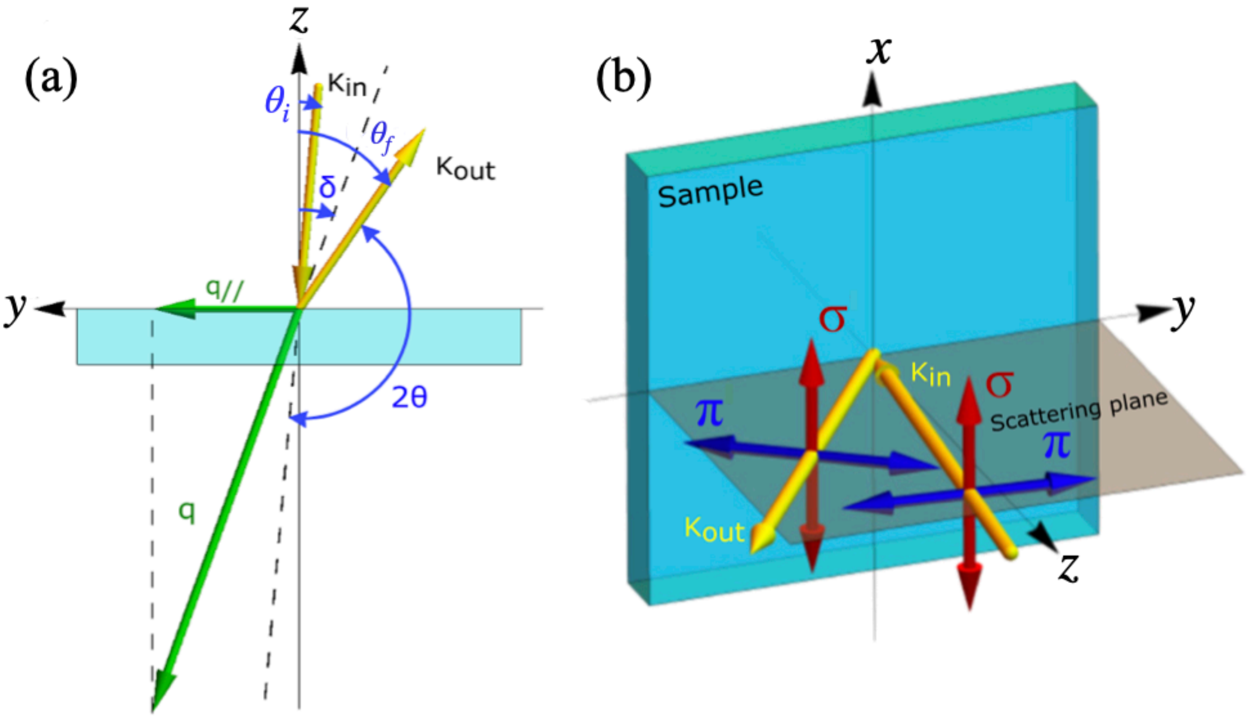

Figure A.1: (a) Schematic illustration of the scattering geometry, showing the incident ($\mathbf{k}_{\text{in}}$) and scattered ($\mathbf{k}_{\text{out}}$) wave vectors, the scattering angle, and the sample orientation. (b) Experimental setup emphasizing the polarization configuration, which allows analysis of the polarization dependence of the scattered intensity [56].

where $\mathcal{M}$ corresponds to the *non-spin-flip (charge)* channel and $\tilde{\mathcal{M}}$ to the *spin-flip (magnetic)* channel. The antisymmetric term involving $\epsilon_{ijk}$ arises due to the strong spin–orbit coupling in the $2p$ core state and is responsible for the polarization dependence of magnetic RIXS.

In the scattering-plane basis, we define the orthogonal unit vectors [see Fig. A.1]

$$\begin{aligned} \hat{x} &: \text{in the scattering plane ,} \\ \hat{y} &: \text{perpendicular to the scattering plane,} \\ \hat{z} &: \text{sample surface normal.} \end{aligned} \tag{A.39}$$

Then, the polarization vectors for the incoming and outgoing x-rays are

$$\begin{aligned} \mathbf{e}^i_\pi &= (\sin\theta_i, 0, \cos\theta_i), & \mathbf{e}^f_\pi &= (-\sin\theta_f, 0, \cos\theta_f), \\ \mathbf{e}^i_\sigma &= (0, 1, 0), & \mathbf{e}^f_\sigma &= (0, 1, 0). \end{aligned} \tag{A.40}$$

Here, $\theta_i$ and $\theta_f$ denote the incident and exit angles of the incoming and outgoing photons, respectively, measured with respect to the sample surface (or, equivalently, the surface normal $\hat{z}$). The total scattering angle is given by $2\theta = \theta_i + \theta_f$. The vectors $\mathbf{e}_\pi^{i,f}$ correspond to $\pi$-polarized light lying in the scattering plane, while $\mathbf{e}_\sigma^{i,f}$ represent $\sigma$-polarized light perpendicular to it.

For the $\pi$–$\sigma$ channel Setting $\mathbf{e}^i = \mathbf{e}_\pi^i$, $\mathbf{e}^f = \mathbf{e}_\sigma^f$, the dot product term of the Eq. A.38 vanishes and only the cross product contributes. Therefor for the above scattering geometry The atomic form factor takes the form

$$\mathcal{M}_{\pi\text{–}\sigma} = i\frac{2}{3}\,(\mathbf{e}_\sigma^f \times \mathbf{e}_\pi^i)_z = -i\frac{2}{3}\left(\mathbf{e}_y^i \mathbf{e}_x^f - \mathbf{e}_x^i \mathbf{e}_y^f\right), \tag{A.41}$$

The prefactor $\frac{2}{3}$ comes from the Clebsch–Gordan coefficient.

Similarly for the $\pi$–$\pi$ channel Setting $\mathbf{e}^i = \mathbf{e}_\pi^i$, $\mathbf{e}^f = \mathbf{e}_\pi^f$, the dot product term of the Eq. A.38 vanishes and only the cross product contributes. Therefor for the above scattering geometry The atomic form factor takes the form

$$\mathcal{M}_{\pi\text{–}\pi} = -\frac{2}{3}\,(\mathbf{e}_\pi^f \cdot \mathbf{e}_\pi^i)_z = -\frac{2}{3}\left(\mathbf{e}_x^i \mathbf{e}_x^f + \mathbf{e}_y^i \mathbf{e}_y^f\right), \tag{A.42}$$

The prefactor $\frac{2}{3}$ comes from the Clebsch–Gordan coefficient.

## A.2 UCL approximation for the Heisenberg model

In the case of undoped, half-filled $d$-level systems such as the cuprates, the low-energy magnetic excitations can be effectively described by a Heisenberg spin Hamiltonian of the form $\sum_{i,j} J_{i,j}\mathbf{S}_i \cdot \mathbf{S}_j$. Within the fast-collision approximation [106, 163, 44], the RIXS excitation process is assumed to be quasi-local, which allows for a systematic expansion of the scattering amplitude in powers of $1/\Gamma$, where $\Gamma$ is the inverse core-hole lifetime as discussed above in Section 3.1.1.

For NSC channel, the RIXS intensity takes the form

$$\begin{aligned} I_\epsilon(\mathbf{q},\omega) \propto & \left[ \frac{1}{\Gamma^2} \sum_f \left| \left\langle f \left| \frac{1}{\sqrt{L}} \sum_i e^{i\mathbf{q}\cdot\mathbf{R}_i} S_i^x \right| g \right\rangle \right|^2 \right. \\ & + \frac{1}{\Gamma^4} \sum_f \left| \left\langle f \left| \frac{1}{\sqrt{L}} \sum_{i,j} e^{i\mathbf{q}\cdot\mathbf{R}_i} J_{i,j} S_i^x (\hat{S}_i \cdot \hat{S}_j) \right| g \right\rangle \right|^2 \\ & \left. + \frac{1}{\Gamma^6} \sum_f \left| \left\langle f \left| \frac{1}{\sqrt{L}} \sum_{i,j,k} e^{i\mathbf{q}\cdot\mathbf{R}_i} J_{i,j} J_{i,k} S_i^x (\hat{S}_i \cdot \hat{S}_j)(\hat{S}_i \cdot \hat{S}_k) \right| g \right\rangle \right|^2 + \cdots \right] \\ & \times \delta\left( E_d^f - E_d^g - \omega \right) \equiv \sum_l S^l(\mathbf{q},\omega) \end{aligned} \tag{A.43}$$

For NSC channel

$$\begin{aligned} I_\epsilon(\mathbf{q},\omega) \propto & \left[ \frac{1}{\Gamma^2} \sum_f \left| \left\langle f \left| \frac{1}{\sqrt{L}} \sum_{i,\sigma} e^{i\mathbf{q}\cdot\mathbf{R}_i} \hat{n}_{i\sigma} \right| g \right\rangle \right|^2 \right. \\ & + \frac{1}{\Gamma^4} \sum_f \left| \left\langle f \left| \frac{1}{\sqrt{L}} \sum_{i,j} e^{i\mathbf{q}\cdot\mathbf{R}_i} J_{i,j} (\hat{S}_i \cdot \hat{S}_j) \right| g \right\rangle \right|^2 \\ & \left. + \frac{1}{\Gamma^6} \sum_f \left| \left\langle f \left| \frac{1}{\sqrt{L}} \sum_{i,j,k} e^{i\mathbf{q}\cdot\mathbf{R}_i} J_{i,j} J_{i,k} (\hat{S}_i \cdot \hat{S}_j)(\hat{S}_i \cdot \hat{S}_k) \right| g \right\rangle \right|^2 + \cdots \right] \\ & \times \delta\left( E_d^f - E_d^g - \omega \right) \equiv \sum_l S^l(\mathbf{q},\omega) \end{aligned} \tag{A.44}$$

In the present case, the spin-flip operator $S_i^x$ appears in the NSC channel because the scattering geometry is defined with the normal to the scattering plane along the $z$-axis, making spin flips correspond to rotations in the transverse ($x$) direction. In this treatment, we focus exclusively on the many-body contribution to the RIXS cross-section. Although atomic form factors also play a significant role in determining experimental spectra, our aim here is to isolate and understand the structure of many-body excitations revealed by RIXS.

# Appendix B

## B.1 Effective Hamiltonian and ED-analysis

### B.1.1 Effective Hamiltonian for lowest energy feature spectra:

In Fig. 5.5(a) of Chapter 5, we observe that the lowest-energy doublets of a single trimer ($|S\rangle_{-1/2}$ and $|S\rangle_{1/2}$) are formed as linear combinations of a singlet state and an unpaired spin. As a result, each trimer effectively behaves as a spin-$1/2$ object. These doublets are separated from the higher-energy states by a finite gap, which ensures that the low-energy dynamics of the trimer chain can be faithfully captured by an effective Hamiltonian acting only within this reduced Hilbert space.

The trimer chain is invariant under translations with a unit cell containing three spins, and it also respects SU(2) rotational symmetry. Consequently, any effective Hamiltonian must preserve both translation symmetry and SU(2) invariance.

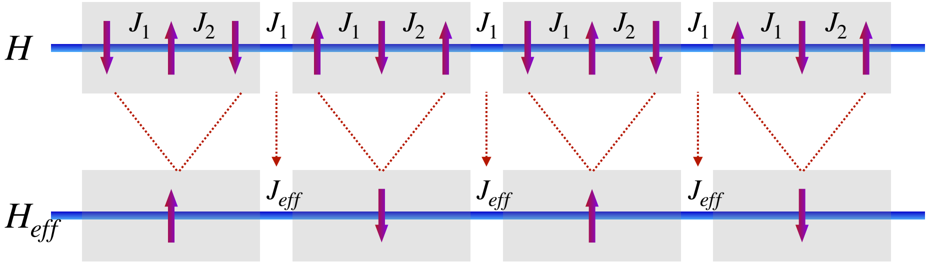

Figure B.1: Decomposition of the trimer chain into intra-trimer Hamiltonian $H_t$ (three-site interactions) and inter-trimer Hamiltonian $H_{tt}$ (coupling between neighboring trimers).

To proceed, we separate the trimer Hamiltonian into two contributions (Fig. B.1): the intra-trimer Hamiltonian $H_t$, which governs interactions within each three-spin block, and the inter-trimer Hamiltonian $H_{tt}$, which describes couplings between neighboring blocks:

$$\hat{H}_t = \sum_{i=1}^{N} \left( J_1 \mathbf{S}_i^1 \cdot \mathbf{S}_i^2 + J_2 \mathbf{S}_i^2 \cdot \mathbf{S}_i^3 \right), \tag{B.1}$$

$$\hat{H}_{tt} = \sum_{i=1}^{N} J_1 \mathbf{S}_i^3 \cdot \mathbf{S}_{i+1}^1. \tag{B.2}$$

Here, $N = L/3$ is the number of trimers, and the inter-trimer term couples the third spin of the $i$th trimer with the first spin of the $(i+1)$th trimer.

Each trimer possesses two degenerate ground states [Fig. 5.5(a)], which can be expressed as:

$$|S\rangle_{-1/2} = a_0|\downarrow \overline{23}\rangle - b_0|\overline{12}\downarrow\rangle, \tag{B.3}$$

$$|S\rangle_{1/2} = -a_0|\uparrow \overline{23}\rangle + b_0|\overline{12}\uparrow\rangle, \tag{B.4}$$

where $|\uparrow\rangle$ and $|\downarrow\rangle$ denote eigenstates of $S^z$, and $a_0$, $b_0$ are coefficients defined in Fig. 5.5(a).

The projection operator $\mathbf{P}_j$ maps the $j$th trimer onto its ground-state doublet:

$$\mathbf{P}_j = |S\rangle^j_{-1/2}\langle\Downarrow|^j + |S\rangle^j_{1/2}\langle\Uparrow|^j, \tag{B.5}$$

where $|\Downarrow\rangle$ and $|\Uparrow\rangle$ are basis states in the effective spin-$1/2$ Hilbert space.

To derive the effective Hamiltonian, we employ the real-space renormalization group approach using the identity [110, 109]:

$$\mathcal{P}\frac{1}{z-H}\mathcal{P} = \left(z\mathcal{P} - \mathcal{P}H\mathcal{P} - \mathcal{P}H\mathcal{Q}\frac{1}{z-\mathcal{Q}H\mathcal{Q}}\mathcal{Q}H\mathcal{P}\right)^{-1}. \tag{B.6}$$

We define the projection operator $\mathcal{P} = \prod_i P_i$, which projects each trimer onto its ground-state doublet $|S\rangle_{\pm 1/2}$, and $\mathcal{Q} = I - \mathcal{P}$, which projects onto the complementary subspace. The total Hamiltonian is given by $H = H_t + H_{tt}$, where $H_t$ describes interactions within a trimer and $H_{tt}$ accounts for couplings between trimers. To analyze the system, we evaluate the resolvent at $z = \omega + i\eta$, with $\omega = 2E_S$ and $\eta \to 0$, for a chain of length $L$. The projected Hamiltonian terms contribute in distinct ways: $\mathcal{P}H_t\mathcal{P}$ yields a nearest-neighbor (NN) Ising-like interaction $\tilde{S}_i^z \tilde{S}_{i+1}^z$, while $\mathcal{P}H_{tt}\mathcal{P}$ generates NN transverse exchange terms $\tilde{S}_i^{x(y)} \tilde{S}_{i+1}^{x(y)}$. Additionally, the higher-order term $\mathcal{P}H\mathcal{Q}\frac{1}{z-\mathcal{Q}H\mathcal{Q}}\mathcal{Q}H\mathcal{P}$ introduces both NN and next-nearest-neighbor (NNN) interactions. Combining all these contributions, the effective Hamiltonian takes the form of a Heisenberg model,

$$\hat{H}_{\text{eff}} = J_{\text{eff}} \sum_{i=1}^{L/3} \widetilde{\mathbf{S}}_i \cdot \widetilde{\mathbf{S}}_{i+1} + J'_{\text{eff}} \sum_{i=1}^{L/3} \widetilde{\mathbf{S}}_i \cdot \widetilde{\mathbf{S}}_{i+2}, \tag{B.7}$$

where $\widetilde{\mathbf{S}}$ is the effective spin-$1/2$ operator associated with each trimer.

This effective Hamiltonian corresponds to a Heisenberg antiferromagnetic chain (HAC) with nearest-neighbor (NN) and next-nearest-neighbor (NNN) couplings. The dominant effective coupling is $J_{\text{eff}} = a_0 b_0 (a_0 + b_0)^2 J_1 \approx 0.16 J_1$ while the effective NNN coupling is $J'_{\text{eff}} = [a_0 b_0 (a_0 + b_0)^2 \left(b_1(a_0+b_0) - a_1 b_0\right) \left(a_0(2a_1+b_1) + b_0(a_1+b_1)\right)]/\Delta E$ with $\Delta E = E_0 - E_1$, where $E_0$ is the ground-state energy of an isolated trimer and $E_1$ is the doublon excitation energy. Numerically, $J'_{\text{eff}} \sim 10^{-4} J_1$, implying that $H_{\text{eff}}$ is, to excellent accuracy, a NN HAC [99]. This effective model successfully captures the gapless low-energy excitations of the trimer chain, which are known as spinons. The corresponding low-energy spectrum forms a two-spinon continuum with the predicted lower boundary given by $\omega_l = \pi J_{eff} |\sin(3\mathbf{q})|/2$ and the upper boundary by $\omega_u = \pi J_{eff} |\sin(3\mathbf{q}/2)|$. which are plotted as white dashed lines in the first Brillouin zone in Fig. 5.4(a) of the chapter 5 and labeled as "spinons."

## B.2 Quasiparticle analysis

### B.2.1 Dispersion relations at zero and finite field

The low-energy spectrum of the trimer spin chain is composed of distinct elementary excitations, which can be classified ascomposite quasi particle govorn by single trimer excitations. To gain further insight into the nature of these excitations, We compute approximate dispersion relations of single-trimer excitations, $|D\rangle_\sigma$ and $|Q\rangle_\sigma$, at both zero and finite fields [126]. Their dispersions, obtained within a variational single–particle approach. The resulting spectra, corresponding to the zeroth-order RIXS process, are presented in Fig. 5.4(a) of the chapter 5. The dispersion relations corresponding to the propagation of one trimer excitations within the trimer spin chain with momentum $\mathbf{q}$.

### Model and Ground State Construction

We consider a trimer spin chain in which each unit cell (trimer) is described by its local Hamiltonian. The complete Hamiltonian of the system is given by the sum of intra-trimer contributions $H_m$ and inter-trimer couplings $H_{m,m+1}$, assuming periodic boundary conditions:

$$H = \sum_{m=1}^{L/3} H_m + \sum_{m=1}^{L/3} H_{m,m+1}. \tag{B.8}$$

We assume a simple variational ansatz for the zero-field ground state, constructed as a staggered direct product of single-trimer ground states $\{|S\rangle_\sigma, |S\rangle_{-\sigma}\}$. This is justified since the ground state is dominated by states in the singlet sector. For an even number of trimers, the variational ground state is

$$|\psi_\text{G}\rangle = |S_1\rangle_\sigma |S_2\rangle_{-\sigma} \cdots |S_{L/3}\rangle_{-\sigma} \tag{B.9}$$

which is consistent with $S_T^z = 0$. This ansatz captures the essential symmetry of the trimer chain and provides a natural reference for constructing excitations.

The corresponding ground state energy is obtained as

$$\langle H\rangle_\text{G} = \langle\psi_\text{G}| H |\psi_\text{G}\rangle = \frac{L}{3}E_S + \frac{1}{4}a_0 b_0 (a_0 + b_0)^2 \frac{L}{3} J_1, \tag{B.10}$$

where $a_0$ and $b_0$ are amplitudes of the trimer ground state wavefunction in the chosen basis.

### Excited States: $|D\rangle_\sigma$ and $|Q\rangle_\sigma$

To construct single-trimer excitations, we promote one trimer from $|S\rangle_\sigma$ to either $|D\rangle_{-\sigma}$ or $|Q\rangle_{\sigma\pm1}$, corresponding to $\Delta S^z = \pm1$ at a single site in $|\psi_\text{G}\rangle$. For example, the state corresponding to a single $|D\rangle_{1/2}$ excitation at site $r$ is

$$\left|\psi_{D_{1/2}}\right\rangle_r = |S_1\rangle_\sigma \cdots |D_r\rangle_{1/2} \cdots |S_{L/3}\rangle_{-\sigma}, \tag{B.11}$$

respecting spin selection rules. We then construct momentum-resolved excitations via

$$\left|\psi^{\mathbf{q}}_{D_{1/2}}\right\rangle = \frac{1}{\sqrt{L/3}} \sum_{r=1}^{L/3} e^{-i\mathbf{q}\cdot\mathbf{r}} \left|\psi_{D_{1/2}}\right\rangle_r . \tag{B.12}$$

This construction allows to acquire nontrivial dispersion relations arising from inter-trimer couplings.

### Energy Expectation Values

The dispersion relation follows as the difference between excited- and ground-state energies:

$$\epsilon_q^{D_{1/2}} = \langle \psi^{\mathbf{q}}_{D_{1/2}} | H | \psi^{\mathbf{q}}_{D_{1/2}} \rangle - \langle \psi_{\mathrm{G}} | \, H \, | \psi_{\mathrm{G}} \rangle \tag{B.13}$$

### Dispersion of $|D\rangle_\sigma$ Excitations

For the $|D\rangle_\sigma$ excitation, the dispersion in the reduced Brillouin zone is found to be

$$\begin{aligned}\epsilon_{D_{\pm 1/2}}(q) = E_D - E_S &- \frac{1}{4} a_0 b_0 (a_0 + b_0)^2 J_1 \\ &- \frac{1}{8} a_1 (a_0 + b_0) \left[ a_0 (a_1 + b_1) - b_0 b_1 \right] J_1 \\ &+ \frac{1}{4} \left[ a_0 a_1 - b_1 (a_0 + b_0) \right] \left[ a_0 (a_1 + b_1) + b_0 (2a_1 + b_1) \right] J_1 \cos(q). \end{aligned} \tag{B.14}$$

To unfold this dispersion into the full Brillouin zone, one substitutes $q \to 3q$ [126], yielding

$$\begin{aligned}\epsilon_{D_{\pm 1/2}}(q) = E_D - E_S &- \frac{1}{4} a_0 b_0 (a_0 + b_0)^2 J_1 \\ &- \frac{1}{8} a_1 (a_0 + b_0) \left\{ a_0 (a_1 + b_1) - b_0 b_1 \right\} J_1 \\ &+ \frac{1}{4} \left\{ a_0 a_1 - b_1 (a_0 + b_0) \right\} \left\{ a_0 (a_1 + b_1) + b_0 (2a_1 + b_1) \right\} J_1 \cos(3q). \end{aligned} \tag{B.15}$$

The first two terms in this expression correspond to the intrinsic energy gap of the localized doublon excitation. The cosine-dependent terms encode the dynamics induced by inter-trimer couplings. By symmetry, excitations with $\Delta S^z = +1$ and $\Delta S^z = -1$ are degenerate and share the same dispersion in the reduced Brillouin zone.

Dispersions for the other single-trimer excitations are computed similarly. Dispersions at finite field, within the plateau, are calculated analogously using the variational ground state $|\tilde{g}\rangle_{\text{plat}} = \prod_{i=1}^{L/3} |S_i\rangle_{1/2}$, which accurately approximates the plateau state as discussed in the main text. These field-dependent dispersions are shown in Fig. 4 of the main paper.

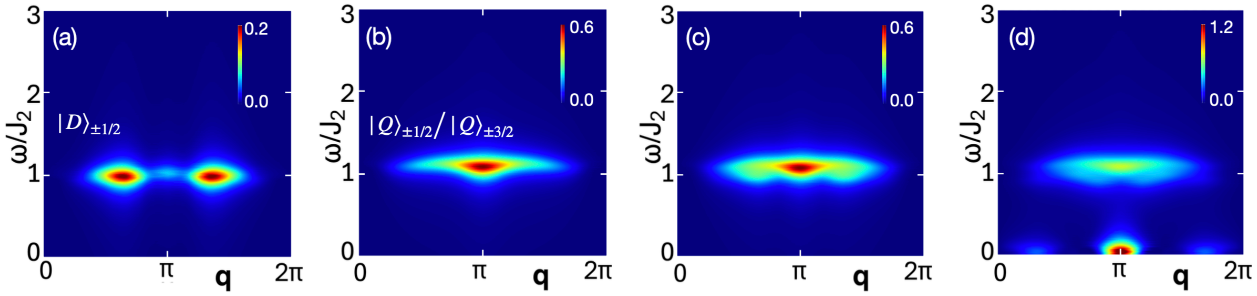

Figure B.2: $\chi^0(\mathbf{q},\omega)$ at zero field obtained by ED in the truncated Hilbert space. Panel (a) for $|S\rangle_\sigma \to |D\rangle_{\sigma\pm1}$, Panel (b) for $|S\rangle_\sigma \to |Q\rangle_{\sigma\pm1}$ excitation. Panel (c) shows the consolidated plot. Panel (d) is the exactly calculated $\chi^0(\mathbf{q},\omega)$ on four trimer.

### B.2.2 $l = 0$ RIXS contribution in truncated Hilbert Space

To go beyond the product ansatz, we compute ED-based $l = 0$ RIXS using the exact ground state at zero field, while restricting excited states to one single-trimer excitations only. We construct a truncated Hilbert space where each trimer hosts at most one internal excitation, $|S\rangle_\sigma \to |D\rangle_{\sigma\pm1}$ or $|S\rangle_\sigma \to |Q\rangle_{\sigma\pm1}$ and use only these excitations in computing $\chi^0(\mathbf{q},\omega)$. Results with $|D\rangle_\sigma$ and $|Q\rangle_\sigma$ excitations appear in Supplemental Fig. B.2(a,b), and match the energy locations in Fig. 2(a) of the main paper. Panel (c) shows their sum, compared with the full ED result in (d). The agreement, near $\omega \sim 1.1J_2$, confirms their origin in single-trimer quasiparticles. As Fig. 2(a) uses DMRG on larger systems, the comparison is qualitative.

### B.2.3 Analytical understanding of the $q$-dependence in $l = 0$ RIXS spectra at magnetization plateau

To gain a simplified understanding of the momentum dependence in the low-energy $l = 0$ RIXS spectra, we approximate the plateau ground state by replacing $|S\rangle_{1/2}$ with the dominant component $|\uparrow,\bar{2}3\rangle$[126]. This approximation is justified because the coefficient $a_0$ is much larger than $b_0$ in the exact form $|S\rangle_{1/2} = a_0|\uparrow\bar{2}3\rangle + b_0|\bar{1}2\uparrow\rangle$ (see Fig. 5.5(a) of the chapter 5, where numerical values are provided in the caption). Within this approximation, the single-trimer ground state in a magnetic field $h_z = 0.5J_2$ has energy

$$E_{\tilde{g}} = -\frac{h_z}{2} = -0.25J_2.$$

The allowed excitations with $\Delta S^z = \pm 1$ can then be expressed as

$$\{|f\rangle = |\downarrow \overline{23}\rangle, \quad |\uparrow\uparrow\uparrow\rangle, \quad |\uparrow\downarrow\downarrow\rangle\}.$$

These final states correspond to distinct physical processes: a spin flip on the polarized site, a fully spin-polarized trimer, and a broken singlet on sites $\{2, 3\}$, respectively. Their excitation energies, measured relative to $E_{\tilde{g}}$, are given by $h_z$, $J_2 - h_z/2$, and $J_2 + h_z$.

With these ingredients, the analytical expression for the $l = 0$ RIXS spectrum reduces to

$$S^0(\mathbf{q}, \omega) = \frac{1}{3}\,\delta(\omega - h_z) + \frac{2}{3}\,\sin^2\!\left(\tfrac{qa}{2}\right)\Big\{\delta(\omega - J_2 + h_z/2) + \delta(\omega - J_2 - h_z)\Big\}.$$

This simple form provides direct physical insight into the spectral features. The first term corresponds to a sharp, non-dispersive mode at $\omega = h_z$, while the latter terms give rise to two dispersive branches that scale with $\sin^2(qa/2)$. In particular, at $q = \pi$ these dispersive branches appear near $\omega = 0.75J_2$ and $\omega = 1.5J_2$, in agreement with the numerical spectra shown in Fig. 5.6(b). Thus, the crude approximation captures the essential structure of the lowest three bands in the RIXS response. We emphasize, however, that higher-energy continua and multi-trimer processes are absent from this treatment, as expected for a single-trimer variational description.

Finally, the dependence of these excitation energies on the applied magnetic field $h_z$ provides further intuition for the evolution of the RIXS spectra across the three field values shown in Fig. 5.6. As $h_z$ increases, the non-dispersive mode shifts linearly with field, while the dispersive branches also shift but retain their sinusoidal momentum dependence. This simple picture explains the field-driven evolution of the low-energy features and highlights how the interplay of Zeeman splitting and intra-trimer exchange determines the spectral structure. Although approximate, this analytical framework reproduces the main qualitative trends of the full numerical simulations and provides a transparent physical interpretation of the $q$- and $h_z$-dependence of the $l = 0$ RIXS spectra [59].

Table B.1: Energies of single trimer excitations for different $h_z$[126].

| Final State | $h_z = 0.2J_2$ | $h_z = 0.5J_2$ | $h_z = 0.9J_2$ | State Description |
|---|---|---|---|---|
| $h_z$ | 0.2 | 0.5 | 0.9 | $\lvert\downarrow \bar{23}\rangle \approx \lvert S\rangle_{-1/2}$ |
| $J_2 - h_z/2$ | 0.9 | 0.75 | 0.55 | $\lvert\uparrow\uparrow\uparrow\rangle = \lvert Q\rangle_{3/2}$ |
| $J_2 + h_z$ | 1.2 | 1.5 | 1.9 | $\lvert\uparrow\downarrow\downarrow\rangle \approx \lvert D\rangle_{-1/2}$ |

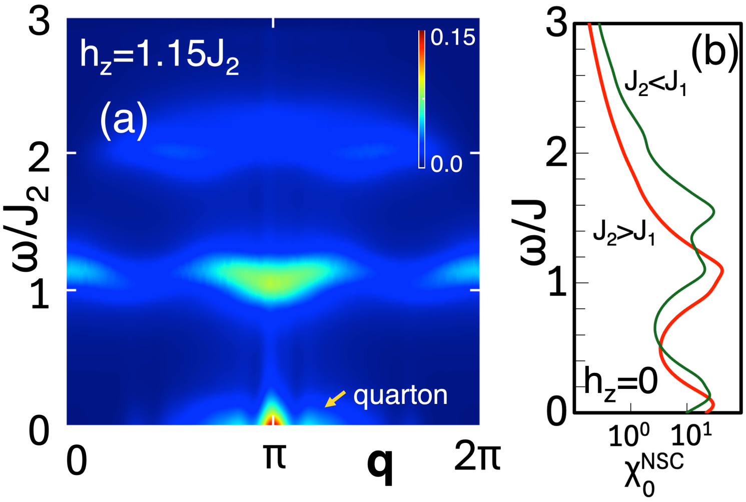

Figure B.3: (a) $S^0(\mathbf{q}, \omega)$ for $h_z = 1.15J_2$, beyond the plateau with a gapless spectra ans quarton $|Q\rangle_{3/2}$ continuum. (b) Zero field $S^0(\omega)$ for trimerized spin-1/2 chain with $J_1 > J_2$ ($J_2/J_1 = 0.27$) and $J_1 < J_2$ ($J_1/J_2 = 0.27$).[126]

## B.3 Comparison of RIXS spectra beyond the plateau and for $J_2 > J_1$

Fig. B.3(a) illustrates the $l = 0$ RIXS response $S^0(\mathbf{q}, \omega)$ at $h_z = 1.15J_2$, a field strength just beyond the one-third magnetization plateau. At this value of $h_z$, the spectrum becomes gapless and is dominated by excitations involving the $|Q\rangle_{3/2}$ state. These excitations form a dispersive continuum, consistent with the interpretation of emergent $S = 1$ quasiparticles discussed in the chapter 5. Their appearance signals the breakdown of the plateau phase and the onset of a gapless regime where trimer triplet states proliferate.

In Fig. B.3(b), we present a direct comparison between the $l = 0$ RIXS contribution for the case studied in the chapter 5 ($J_1 > J_2$) and the opposite exchange hierarchy ($J_2 > J_1$). For weakly coupled trimers ($J_2 > J_1$), the spectrum shows a significantly broader spread of the single-trimer excitation levels. This broader distribution leads to the opening of larger spectral gaps and modifies the overall spectral structure compared to the strongly coupled case. Such distinct features have been reported in earlier studies [32, 137], where the interplay between intra- and inter-trimer couplings was shown to strongly influence the excitation continua.

An important consequence of this difference is the shift in the field values at which magnetization plateaus occur. In the $J_2 > J_1$ regime, the plateau sets in only at substantially higher magnetic fields [33], reflecting the greater stability of the singlet background formed by weakly coupled trimers. This behavior stands in sharp contrast to $Cu_3(P_2O_6OH)_2$, where $J_1 > J_2$ and the plateau emerges at much lower fields.

Together, these results emphasize how the hierarchy of exchange couplings fundamentally alters both the RIXS spectral signatures and the field dependence of magnetization plateaus. By tuning the ratio $J_1/J_2$, trimer chain systems can thus realize distinct regimes of quantum magnetism—ranging from fractionalized spinon-like excitations to emergent trimer quasiparticles—with directly observable consequences in nonlocal spectroscopic probes such as RIXS.